eXPRESS Polymer Letters Vol.2, No.8 (2008) 539
Available online at www.expresspolymlett.com
DOI: 10.3144/expresspolymlett.2008.64

Editorial corner – a personal view
Polymers and 'strange' liquids

*Gy. Bánhegyi**

Polygon Consulting, Arany János u. 28., H-1153 Budapest, Hungary

Interactions of polymers and liquids have been intensively studied since the beginning of polymer science and these investigations contributed significantly to our understanding of polymer structure, conformation and thermodynamics. There are two classes of liquids, however, which may raise new questions and promote new research leading to new understanding in this field, namely *ionic liquids* and *supercritical fluids*, more specifically *supercritical water*. Both classes of 'strange liquid' have been developed, studied and used widely in the so-called 'green chemistry' movement in the last decades of the 20th century.

Ionic liquids are true ionic compounds with bulky, non-symmetric (mostly nitrogen based organic) cations and special (mostly perfluorinated inorganic) anions having a melting point below, or in the neighborhood of room temperature. They have extremely low vapor pressure, can be relatively easily recovered, they are non-flammable and heat resistant. Ionic liquids can be used as reaction media for polymerization, but they can dissolve and/or swell certain polymers and can be used as plasticizers even with medium polarity polymers as e.g. poly(methyl methacrylate). Polymer gels swollen with ionic liquids may be used as solid polymer electrolytes. Ionic liquids can be trapped in crosslinked polymers by *in situ* polymerization or even built into the polymer network. As polymerization media, they can be used in living polymerization or in polymer-analogous reactions.

Supercritical (*sc*) fluids, as special kinds of low viscosity liquids with adjustable solution power have already been with us for decades and the uses of *sc* CO_2 (p_{cr} = 73 bar, T_{cr} = 304 K) as reaction or extraction medium have become well known in the 'polymer community'. As patents show *sc* CO_2 may provide an alternative solution to melt or solution blending in the preparation of nanocomposites as well. Here, however, I would like to draw the readers' attention to *sc* H_2O, supercritical water (p_{cr} = 221 bar, T_{cr} = 647 K), as a special medium for controlled polymer recycling and degradation. The dielectric permittivity and the ion-product of *sc* H_2O can be varied within wide limits by adjusting the pressure and temperature which makes possible the degradation of biomass and polymers within seconds even in the absence of catalysts! This feature is especially important with crosslinked resins, rubbers, which cannot be recycled in the molten state. According to the Chemical Abstracts the patenting and publication activity of Asian countries is especially high in this area.

Dr. György Bánhegyi
Member of Executive Editorial Board

*Corresponding author, e-mail: gybanheg@t-online.hu

eXPRESS Polymer Letters Vol.2, No.8 (2008) 540–545
Available online at www.expresspolymlett.com
DOI: 10.3144/expresspolymlett.2008.65

Preparation and characterization of electrospun fibers of Nylon 11

*M. Dhanalakshmi, J. P. Jog**

Polymer Science and Engineering Division, National Chemical Laboratory, Dr. Homi Bhabha road, Pune-411008, India

Received 17 April 2008; accepted in revised form 19 June 2008

Abstract. Nylon 11 nanofibers mats were successfully prepared by electrospinning process from formic acid solution. The scanning electron microscopy (SEM) images showed that nanofibers with uniform diameter were produced when the polymer concentration was 10% w/v, whereas ribbons were formed at a higher concentration. The crystalline structure of the nanofibers mats was investigated using X-ray diffraction (XRD) and it was found that the nanofibers mats crystallized in γ form. The melt crystallized as well as solution casted films however exhibited α form. The thermal properties of these samples were studied using differential scanning calorimetry (DSC) and it was observed that electrospun fibers showed higher crystallinity than the melt-crystallized samples. However, the crystallinity of electrospun fibers was lower than the solution-crystallized sample.

Keywords: *nanomaterials, biocompatible polymers, electrospinning, Nylon 11*

1. Introduction

Electrospinning process provides a simple route to fabricate polymer fibers with diameters ranging from nanometers to micrometers. The advantage of these fibers is the huge increase in the surface area to volume ratio and recently, electrospinning process has been found to be a cost effective approach for fabrication of polymer fiber mats. Numerous studies have been reported addressing various aspects of electrospinning process [1–5]. The various factors that are known to affect electrospun fibers include solution viscosity, surface tension, electric field intensity and distance. These electrospun fiber mats have wide applications in water filters, textiles, sound absorbers materials, sensors for gas and other chemicals. The use of electrospun nanofibrous mats has also attracted a great deal of attention in biomedical applications. The most important feature of these nanofibrous mats which is exploited in biomedical applications is their ability to mimic extracellular mass (ECM). As a result, these mats are found suitable for biomedical applications as tissue engineering scaffolding, wound dressing, artificial blood vessels, drug delivery carriers, cosmetic and skin masks [6–10]. Recently, several researchers have reported electrospinning of several biocompatible polymers to explore their use in various biomedical applications These include polycaprolactone (PCL), polylactic acid (PLA), poly vinyl alcohol (PVA), chitosan, polyhydroxybuyrate and its copolymers [11–19]. However, there is very little information focusing on electrospinning of Nylon 11.

In this communication, we present preparation and characterization of electrospun fibers of Nylon 11 which is a biocompatible polymer. In this study, we investigate the morphology of Nylon 11 fibers under different weight concentrations. The electrospun fibers were characterized for their morphology and structure using scanning electron microscopy

*Corresponding author, e-mail: jp.jog@ncl.res.in

(SEM), Wide angle X-ray diffraction (WAXD), and differential scanning calorimetry (DSC).

2. Experimental

2.1. Materials

Nylon 11 with a density of 1.026 g/cc, melting point of 189°C and glass transition temperature of about 47°C was purchased from Aldrich Chemicals. Formic acid was procured from Merck. All chemicals were used as received without any further purification.

2.2. Solution preparation

Nylon 11 solutions of 10 and 20 wt% were prepared by dissolving Nylon pellets in formic acid. The solutions were prepared in a constant temperature bath at 70°C for 2 hr. The solutions were cooled to room temperature before electrospinning. The viscosity of solutions was measured using Brookfield viscometer model DV-II+Pro and the viscosity values were found to be 15.5 mPa·s for 10 wt % solution and 29.2 mPa·s for 20 wt% solution.

Films were cast from polymer solution in Petri dish by evaporating the solvent and were used for elucidating the effect of electrospinning process on the structure. For comparison, the melt pressed films were also prepared from Nylon 11 pellets using a laboratory press. Nylon 11 pellets, melt pressed film and solution cast films are coded as P, MP, SC respectively.

2.3. Electrospinning process

The electrospinning apparatus developed in our laboratory was used for this work. The electrospinning setup was horizontal. It consisted of a high voltage supply (0–40 kV) from Gamma Corporation, USA and a syringe pump from Sage instruments (model 351) with flow rate capacity from 0.0015 to 60 ml/min. A glass syringe with 10 ml capacity and a stainless steel needle with 0.8 mm diameter was used. The collector distance was kept at 10 cm from the needle and flow rate was maintained at 0.2 ml/min for experiment. The electrospinning was carried out at 20 kV. The needle was charged to +20 kV and the collector was earthed. Electrospinning process was carried out at room temperature. The electrospun fibers from 10 and 20 wt% solutions are coded as ES10 and ES20.

2.4.Characterization

2.4.1. Scanning electron microscopy (SEM)

The morphology of Nylon 11 electrospun fibers was studied by using Leica-440 scanning electron microscope (SEM). The SEM micrographs of the electrospun fiber were recorded at different magnifications. The sample surfaces were sputtered with gold to avoid overcharging.

2.4.2. X-ray diffraction (XRD)

X-ray diffraction analysis of Nylon 11 melt pressed film, solution casted film and electrospun fiber mats was performed on a Panalytical (XPERT-PRO). The scans were recorded at room temperature with 2θ ranging from 5 to 30°.

2.4.3. Differential scanning calorimetry (DSC)

DSC study of Nylon 11 pellets, melt pressed film, solution casted film and electrospun fibers was performed on Perkin Elmer Differential Scanning Calorimeter (DSC-2) in the temperature ranging from 50–250°C. A controlled heating and cooling rate was maintained at 10°C/min. The test was carried out in nitrogen atmosphere. The melting point of polymer (T_m), crystallization temperature (T_c) and % crystallinity of polymer were determined from the heating and cooling scans.

3. Results and discussion

3.1. Electrospinning process

Electrospinning is a process by which sub-micron polymer fibers are produced using an electro statically driven jet of polymer solution or polymer melt. Metering pump is used to control the flow of polymer solution through syringe. The collector is grounded. When no voltage is applied, the polymer solution through the needle falls like a hemispherical drop due to surface tension. As the intensity electric field is increased, hemispherical surface of fluid starts to elongate to form a conical shape known as Taylor cone [20]. When the threshold value of electrostatic force is reached, it overcomes the surface tension of the polymer solution and a charged jet is ejected from the apex of the cone. The charged jet travels linearly only for a short distance and then undergoes bending instability result-

Figure 1. Electrospinning of Nylon 11

ing in formation of looping trajectory of the jet. The charged jet elongates and the solution dries out and is finally deposited on the collector as fibers. Figure 1 presents the photograph of electrospinning of Nylon 11.

The fibers were collected on the Aluminum collector plate. These electrospun fibers were vacuum dried and then characterized by using SEM, XRD and DSC.

3.2. Scanning electron microscopy

It is well documented that a variety of structures such as beads, fibers and ribbons can be achieved in electrospinning of polymers as reported earlier by Koombhongse *et al*. [21]. The shape and size of these structures are governed by a number of parameters such as polymer solution properties, vapor pressure of the solvent, humidity and also the process parameters such as feed rate, field strength and geometry of the electrode.

Scanning Electron Micrographs electrospun fibers are shown in the Figure 2. As can be seen from the Figure 2a for ES10 sample, nanofibers with round cross section are formed and the fibers are not aligned. For ES20 samples, nanofibers are not with round cross section but nanofibers show ribbon like structures as shown in Figure 2b. It is also observed from the micrographs that ES10 nanofibers have uniform diameter of the order of about 200 nm whereas ES20 sample shows diameter ranging from about 400 nm to few micrometer are formed as shown in Figure 2c and 2d.

In case of polystyrene, similar flat fibers were obtained for 30% w/v solutions in dimethylformamide [21]. The formation of flat ribbons was attributed to the uneven evaporation of the solvent between the skin and the core of the charged jet

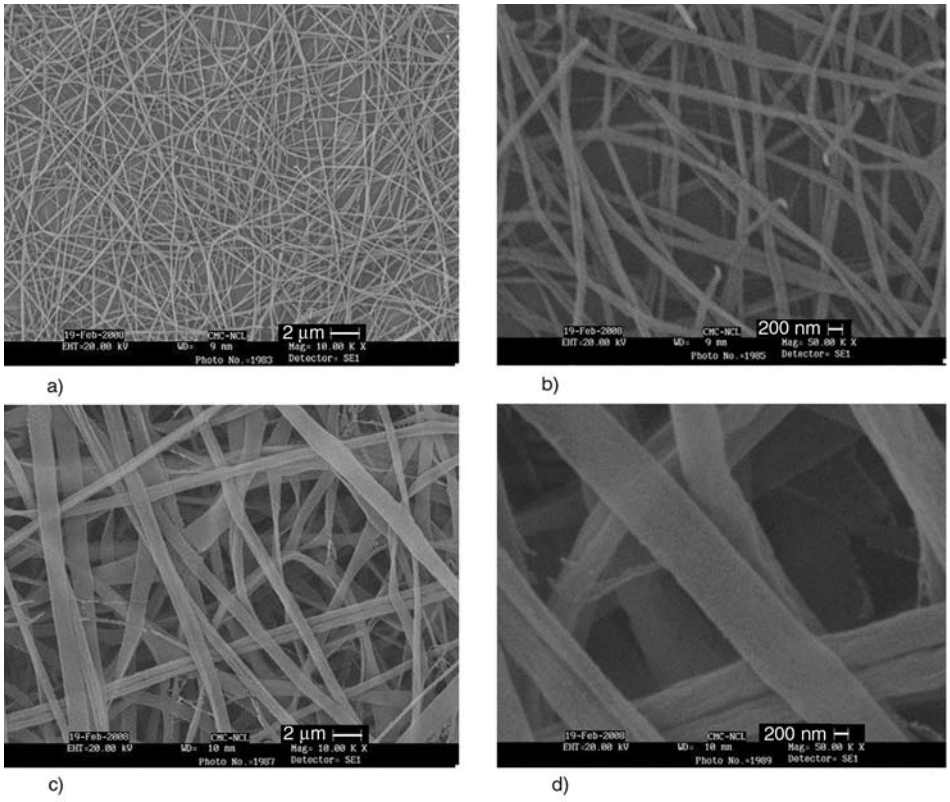

Figure 2. a) Scanning electron micrograph of electrospun fibrous mats of Nylon 11 from 10 wt% solution. b) Magnified scanning electron micrograph of electrospun fibrous mats of Nylon 11 from 10 wt% solution. c) Scanning electron micrograph of electrospun fibrous mats of Nylon 11 from 20 wt% solution. d) Magnified scanning electron micrograph of electrospun fibrous mats of Nylon 11 from 20 wt% solution.

causing the jet to collapse. Flat fibers were also reported in electrospun polyvinyl alcohol fibers from highly viscous solutions [22].

3.3. X-ray diffraction

Nylon 11 is a interesting polymer as it exhibits at least five different crystalline phases such as α, β, γ, δ, δ' and α'. The crystalline structure and polymorphism of Nylon 11 has been studied by several researchers [23–28]. It has been reported that the α form of Nylon 11 exhibits two characteristic reflections at 2θ = 20.2 and 23.01° [23] whereas the γ form of Nylon 11 exhibits a characteristic reflection at 2θ = 21.34° [24].

The structure of melt pressed film, solution cast film and electrospun fibers is studied using XRD to ascertain the crystalline form of Nylon 11. Figure 3a and 3b show the diffraction patterns of MP and SC samples respectively. MP and SC samples exhibit two characteristics reflections around at 2θ = 20.4 and 23.01° corresponding to α crystalline phase of Nylon 11.

The XRD patterns of ES10 and ES20 are depicted in Figure 3a and 3b respectively. In these diffraction patterns of the electrospun fibers, a single peak is observed at about 2θ = 21.63°. This reflection corresponds to the γ form of Nylon 11 [28].

The XRD results indicate that the electrospinning process transforms the α phase of Nylon 11 to γ phase of Nylon 11 whereas the SC sample exhibits α phase of Nylon 11. This leads to the conclusion that the change in crystal form of Nylon 11 results because of the electrospinning process and not because of solution crystallization. In the electrospinning process, the structure of the fiber is formed under the influence of two simultaneous processes namely the evaporation of the solvent

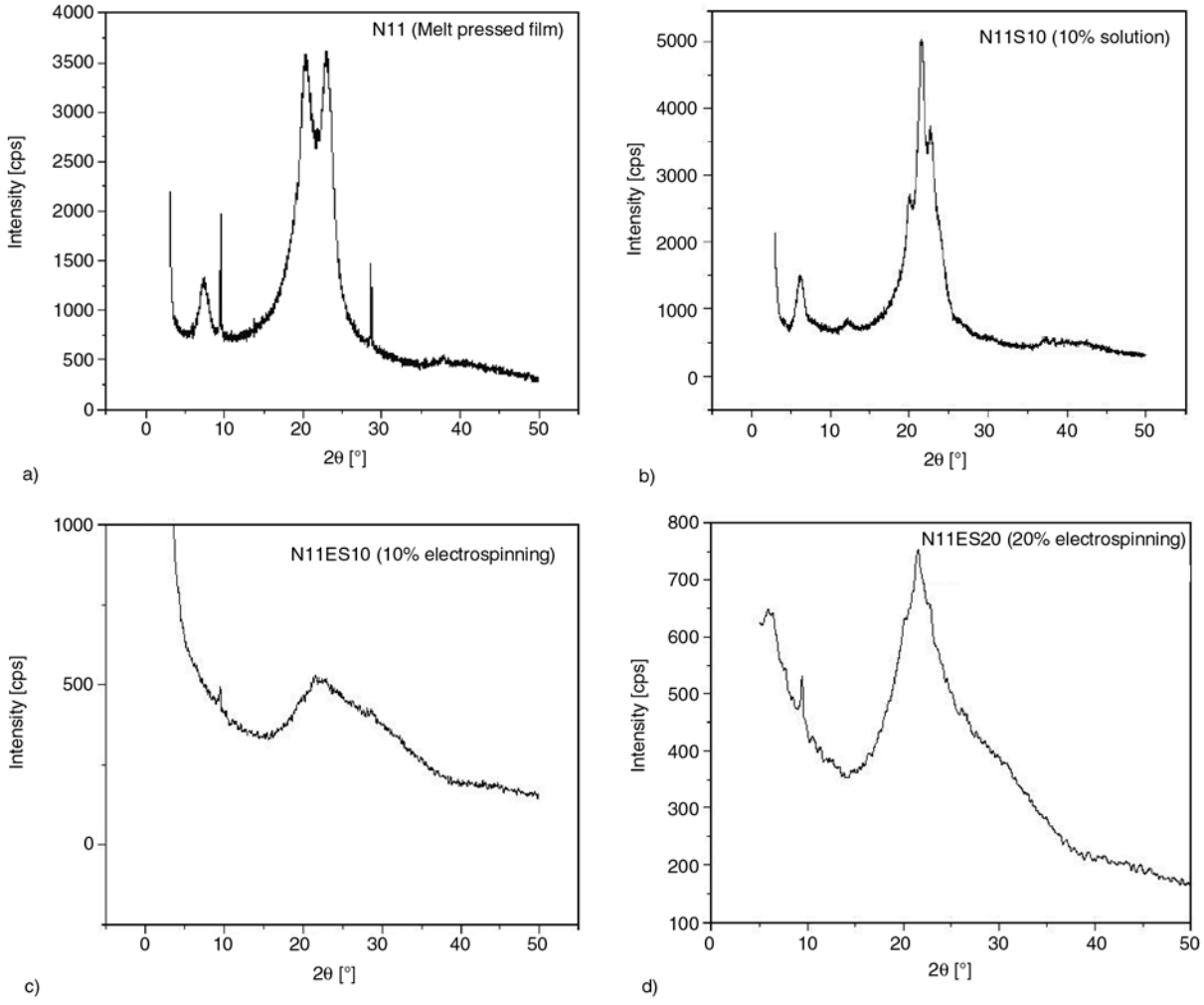

Figure 3. a) XRD scan of melt pressed Nylon 11 film. b) XRD scan of solution casted Nylon 11 film. c) XRD scan of electrospun fibrous mats of Nylon 11 from 10 wt% solution. d) XRD scan of electrospun fibrous mats of Nylon 11 from 20 wt% solution

Table 1. Melting and crystallization parameters of Nylon 11 samples

Sample coding	First heating			Crystalline temperature
	Heat of fusion ΔH_f [J/g]	Crystallinity χ_c [%]	Melting point T_m [°C]	T_c [°C]
P	32.60	15.80	190.90	150.30
MP	40.96	20.00	191.10	160.60
SC10	87.99	41.43	193.68	162.60
ES10	49.32	24.00	188.30	167.90
SC20	84.48	41.20	194.71	161.28
ES20	55.18	26.90	189.40	162.70

and the elongation of the fibers while crystallization from solution takes place under quiescent conditions. Thus, crystallization from solution results in more ordered α form whereas crystallization takes place under mechanical deformation during electrospinning. Similar changes in the crystal form have been noted in Nylon 6, by Stephans *et al.* [29]. They have attributed the formation of γ phase during electrospinning process to the high stress experienced by Nylon 6 during fiber formation.

3.4. Differential scanning calorimetry (DSC)

A thermal analysis of P, MP, SC, ES10 and ES20 is performed on the DSC. The melting and crystallization parameters are presented in Table 1. The crystallinity of samples was calculated by dividing the heat of fusion of polymer samples to heat of fusion of 100% crystalline Nylon 11. The reported value of heat of fusion of 206 J/g for 100% crystalline Nylon 11 was used to calculate the % crystallinity [30]. ES10 and ES20 show higher crystallinity than MP and as received P samples. The crystallization temperature is also higher for electrospun fibers as compared to bulk sample.

It is interesting to note that the solution cast films exhibit highest crystallinity (≈41%) as compared to the ES and melt pressed film. This indicates that the ES mats have lower crystallinity than the corresponding solution cast films. The structure formation during electrospinning is governed by the simultaneous processes of evaporation of the solvent and the elongation of the solidifying fiber. In crystalline polymers, solidification is also connected with formation of crystals. The shorter time for crystallization is expected to result in small crystallites with defects and thus lower degree of crystallinity [31]. It can be envisaged, that the rapid solidification of the polymer solution limits the development of crystallinity while the solidification during film casting takes place slowly resulting in higher degree of crystallinity. Similar results have been reported for poly (lactic acid) (PLLA) [32], Nylon terpolymer [2], Nylon 11 [33] and in PET [34].

4. Conclusions

Nanofibers of Nylon 11 are electrospun at two different solution concentrations. At 10 wt% concentration, uniform nanofibers with diameter of approximately 300 nm are obtained. At higher polymer concentration (20 wt%) formation of ribbons is observed rather than circular fibers. The nanofibers mats so produced exhibit γ crystalline structure as evidenced by the XRD results. The formation of γ crystals is attributed to the possible high rate of elongation experienced by the polymer during electrospinning. The thermal properties of nanofibers show increase in crystallinity as compared to the melt crystallized sample whereas lower crystallinity than that of solution crystallized samples.

References

[1] Bergshoef M. M., Vancso G. J.: Transparent nanocomposites with ultrathin electrospun nylon-4,6 fiber reinforcement. Advanced Materials, **11**, 1362–1365 (1999).

[2] Li Y., Huang Z., Lu Y.: Electro spinning of nylon-6, 66,1010 terpolymer. European Polymer Journal, **42**, 1696–1704 (2006).

[3] Zussman E., Burman M., Yarin A. L., Khalfin R., Cohen Y.: Tensile deformation of electrospun nylon-6,6 nanofibers. Journal of Polymer Science, Part B: Polymer Physics, **44**, 1482–1489 (2006).

[4] Dersch R., Liu T., Schaper A. K., Greiner A., Wendorff J. H.: Electrospun nanofibers: Internal structure and intrinsic orientation. Journal of Polymer Science, Part A: Polymer Chemistry, **41**, 545–553 (2003).

[5] Liu Y., Cui L., Guan F., Gao Y., Hedin N. E., Zhu L., Fong H.: Crystalline morphology and polymorphic phase transitions in electrospun nylon-6 nanofibers. Macromolecules, **40**, 6283–6290 (2007).

[6] Zhang Y., Ouyangn H., Lim C. T., Ramakrishna S., Huang Z-M.: Electrospinning of gelatin/PCL composite fibrous scaffolds. Journal of Biomedical Materials Research, Part B: Applied Biomaterials, **72**, 156–165 (2004).

[7] Venugopal J., Zhang Y. Z., Ramakrishna S.: Electrospun nanofibers: Biomedical applications. Proceedings of the Institution of Mechanical Engineers, Part N: Journal of Nanoengineering and Nanosystems, **218**, 35–45 (2005).

[8] Duan Y-Y., Jia J., Wang S H., Yan W., Jin L., Wang Z-Y.: Preparation of PLGA electrospun nanofibers for tissue engineering applications. Journal of US-China Medical Science, **4**, 41–44 (2007).

[9] Buschle-Diller G., Hawkins A., Copper J.: Electrospun nanofibers from biopolymers and their biomedical applications. in 'Modified Fibers with Medical and Specialty Applications' (eds.: Edwards J. V., Buschle-Diller G., Goheen S. C.) Springer, Berlin 67–80 (2006).

[10] Chen J., Chu B., Hsiao B. S.: Mineralization of hydroxyapatite in electrospun nanofibrous poly (L-latic acid) scaffolds. Journal of Biomedical Materials Research, Part A, **79**, 307–317 (2006).

[11] Ren G., Xu X., Liu Q., Cheng J., Yuan X., Wu L., Wan Y.: Electrospun poly (vinyl alcohol)/glucose oxidase biocomposite membranes for biosensor applications. Reactive and Functional Polymers, **66**, 1559–1564 (2006).

[12] Ristolainen N., Heikkilä P., Harlin A., Seppälä J.: Poly (vinyl alcohol) and polyamide-66 nanocomposites prepared by electrospinning. Macromolecular Materials and Engineering, **291**, 114–122 (2006).

[13] Ohkawa K., Cha D., Kim H., Nishida A., Yamamoto H.: Electrospinning of chitosan. Macromolecules Rapid Communications, **25**, 1600–1606 (2004).

[14] Bhattarai N., Edmondson D., Veiseh O., Matsen F. A., Zhang M.: Electrospun chitosan-based naonofibers and their cellular compatibility. Biomaterials, **26**, 6176–6184 (2005).

[15] Kumber S. G., Nukavarapu S. P., James R., Hogan M. V., Laurencin C. T.: Recent patents of electrospun biomedical nanostructures: An overview. Recent Patents on Biomedical Engineering, **1**, 68–78 (2008).

[16] Supaphol P., Chuangchote S.: On the electrospinning of poly (vinyl alcohol) nanofibers mates: A revisit. Journal of Applied Polymer Science, **108**, 969–978 (2008).

[17] Duan B., Yuan X., Zhu Y., Zhang Y., Li X., Zhang Y., Yao K.: A nanofibrous composite membrane of PLGA-chitosan /PVA prepared by electrospinning. European Polymer Journal, **42**, 2013–2022 (2006).

[18] Cheng M-L., Lin C-C., Su H-L., Chen P-Y., Sun Y-M.: Processing and characterization of electrospun poly(3-hydroxybutyrate-co-3-hydroxyhexanoate) nanofibrous membranes. Polymer, **49**, 546–553 (2008).

[19] Hsu C-M., Shivkumar S.: *N,N*-dimethylformamide additions to the solution for the electrospinning of poly(ε-caprolactone) nanofibers. Macromolecular Materials and Engineering, **289**, 334–340 (2004).

[20] Taylor S. G.: Electrically driven jets. Proceeding of the Royal Society of London: Series A, Mathematical and Physical Sciences, **313**, 453–475 (1969).

[21] Koombhongse S., Liu W., Reneker D. H.: Flat polymer ribbons and other shapes by electrospinning. Journal of Polymer Science, Part B: Polymer Physics, **39**, 2598–2606 (2001).

[22] Koski S., Yim K., Shivkumar S.: Effect of molecular weight on fibrous PVA produced by electrospinning. Materials Letters, **58**, 493–497 (2004).

[23] Zhang Q., Mo Z., Zhang H., Liu S., Cheng S. Z. D.: Crystal transitions of nylon 11 under drawing and annealing. Polymer, **42**, 5543–5547 (2001).

[24] Nair S., Ramesh C., Tashiro K.: Polymorphism in nylon-11: Characterization using HTWAXS and HTFTIR. Macromolecular Symposia, **242**, 216–226 (2006).

[25] Yoshioka Y., Tashiro K.: Structural changes in phase transitions of nylon model compounds. 1. Transition behavior of model compounds of R-NHCo-R' type. Journal of Physical Chemistry: B, **107**, 11835–11842 (2003).

[26] Nair S., Ramesh C., Tashiro K.: Crystalline phases in nylon-11: Studies using HTWAXS and HTFTIR. Macromolecules, **39**, 2841–2848 (2006).

[27] Zhang G., Li Y., Yan D.: Polymorphism in nylon-11/montmorillonite nanocomposites. Journal of Polymer Science, Part B: Polymer Physics, **42**, 253–259 (2004).

[28] Pande S. A., Kelkar D. S., Peshwe D. R.: Investigation of structural, morphological and dynamic mechanical properties of PANI filled nylon 11. Current Applied Physics, **7**, 590–595, (2007).

[29] Stephens J. S., Chase D. B., Rabolt J. F.: Effect of the electrospinning process on polymer crystallization chain conformation in nylon-6 and nylon-12. Macromolecules, **37**, 877–881 (2004).

[30] Fernandez J. O., Swallowe G. M., Lee S. F.: Crystallization of nylon 11 under compressive high strain rates. Journal of Applied Polymer Science, **80**, 2031–2038 (2000).

[31] Wunderlich B.: Macromolecular Physics, Vol 1. Academic Press, New York (1973).

[32] Zong X., Kim K., Fang D., Ran S., Hsiao B. S., Chu B.: Structure and process relationship of electrospun bioabsorbable nanofibers membranes. Polymer, **43**, 4403–4412 (2002).

[33] Behler K., Havel M., Gogotsi Y.: New solvent for polyamides and its application to the electrospinning of polyamides 11 and 12. Polymer, **48**, 6617–6621 (2007).

[34] Kim J-S., Lee D. S.: Thermal properties of electrospun polyesters. Polymer Journal, **32**, 616–618 (2000).

eXPRESS Polymer Letters Vol.2, No.8 (2008) 546–552
Available online at www.expresspolymlett.com
DOI: 10.3144/expresspolymlett.2008.66

Effect of mixing sequence on the curing of amine-hardened epoxy/alumina nanocomposites as assessed by optical refractometry

M. Philipp[1,], P. C. Gervais[1], R. Sanctuary[1], U. Müller[1], J. Baller[1], B. Wetzel[2], J. K. Krüger[1]*

[1]Laboratoire de Physique des Matériaux, Université du Luxembourg, 162A avenue de la faïencerie, L-1511 Luxembourg
[2]Guest Scientist of the Laboratoire de Physique des Matériaux, Université du Luxembourg, 162A avenue de la faïencerie, L-1511 Luxembourg

Received 12 May 2008; accepted in revised form 19 June 2008

Abstract. High performance refractometry has been proven to be a useful tool to elucidate the isothermal curing process of nanocomposites. As a model system an amine-hardening epoxy filled with non-surface-treated alumina nanoparticles was selected. The tremendous resolution of this experimental technique is used to study morphological changes within nanocomposites via the refractive index. It is shown that these morphological changes are not simply due to the curing process but also depend on the sequence of mixing the nanoparticles either first into the resin or first into the hardener. Independent of the resin/hardener composition, the type of the mixing sequence discriminates systematically between two distinct refractive index curves produced by the curing process. The difference between the two refractive index curves increases monotonically with curing time, which underlines the importance of the initial molecular environment of the nanoparticles.

Keywords: *nanocomposites, mixing sequence, optical properties, epoxies*

1. Introduction

The interest in thermoset-based nanocomposites stems first of all from experimental evidences that due to chemical and/or physical interactions between the surfaces of the nanoparticles and the thermoset the physical properties of the composite are often more affected than predicted by a simple mixing rule applied to the properties of the related constituents [1–9]. It is supposed that the existence of specific interactions between the nanoparticles and the constituents of a thermoset will influence the curing process. Therefore the sequence of mixing the nanopowder first into the resin or first into the hardener may influence the physical properties of the final cured nanocomposite. The importance of this mixing sequence for the morphology and consequently for the phenomenological properties of the molecular network is the main interest of this paper.

The thermoset chosen is an amine-hardening epoxy. As suitable nanoparticles we selected alumina powder produced by industry. As nanoparticles we denote here particles with lateral dimensions smaller than 1 μm (see below). Because of the technical importance an almost stoichiometric resin/hardener composition was chosen as model thermoset. In order to deepen the physical understanding of the role of the mixing sequence several under-stoichiometric compositions are investigated.

Because of its tremendous resolution high performance optical refractometry is chosen as a rather

*Corresponding author, e-mail: martine.philipp@uni.lu

unconventional experimental technique to study temporal evolutions of structure-property relations during the isothermal curing process of epoxy-based nanocomposites as a function of the mixing sequence. The experimental data will be discussed on the base of the Lorentz-Lorenz relation.

2. Experimental

2.1. The constituents

In order to investigate the influence of the mixing sequence on the refractive index properties of epoxy-based nanocomposites the following three constituents were chosen:

i. as a hardener (*H*) we selected diethylene triamine (DETA) (epoxy equivalent weight: 20.64 g/eq) from Fluka Chemie GmbH, Buchs, Switzerland. The DETA molecules possess three reactive amine groups. The refractive index was determined to be $n_D^{298\ \mathrm{K}} = 1.4846 \pm 10^{-4}$.

ii. as resin (*R*) diglycidyl ether of bisphenol A (DGEBA) DER 331 (epoxy equivalent weight: 182–192 g/eq) from DOW Europe GmbH, Stade, Germany was chosen. This resin contains a small amount of dimers and trimers in order to hinder the crystallization of the DGEBA monomers, although even monodisperse DGEBA (melting temperature T_m = 315 K) can easily be supercooled. The refractive index was measured to be $n_D^{298\ \mathrm{K}} = 1.5712 \pm 2 \cdot 10^{-4}$.

iii. as nanoparticles (*N*) alumina Aeroxide® Alu C from Evonik industries AG, Hanau, Germany was selected. These alumina nanoparticles were chosen because they are not surface-treated and they yield improved mechanical properties in epoxy nanocomposites [1]. Finally these nanoparticles are available in sufficient quantities. The primary particles have an average diameter of 13 nm and agglomerate in clusters with diameters below 300 nm (as determined by dynamic light scattering). The refractive index of the nanoparticles was estimated from crystal data [10] to 1.76 at 298 K. As for all stiff crystalline materials, away from structural phase transitions, the refractive index of the alumina particles changes little with temperature and pressure. We suppose that the surfaces of the alumina nanoparticles are contaminated at least with water.

2.2. Samples and sample preparation

The choice of the sample compositions was made on the base of the following four arguments:

i. the influence of the mixing sequence on technically relevant compositions. From the stoichiometric point of view the best choice would be a resin/hardener mass ratio of about *R/H* (*100/11*). The present study is based mainly on the slightly over-stoichiometric *R/H* (*100/14*) system, which shows the biggest tensile shear strength during fracture experiments performed on different epoxy mixtures glued on native aluminium [11]. This composition is known to undergo a chemical glass transition at ambient temperature which restricts the chemical conversion of DGEBA's oxirane rings as measured by infrared spectroscopy to about 70%.

ii. After a curing time of more than two hours, the epoxy *R/H* (*100/14*) adheres perfectly on the prism of the refractometer. In order to avoid destruction of the refractometer, the curing behaviour of epoxy *R/H* (*100/14*) can be followed only during this chemical reaction time.

iii. In order to overcome the shortcomings of ii. and to get insight in the influence of the mixing sequence on the final properties of adhesives (in the sense that all possible chemical reactions have taken place) the following under-stoichiometric sample compositions were selected: *R/H* (*100/7*), (*100/3*), (*100/2*) and (*100/1*).

iv. Pre-investigations have shown that at maximum a mass ratio of hardener/nanoparticles *H/N* (*2/1*) is possible. To make the effect of the nanoparticles as visible as possible concerning the mixing sequence for a given *R/H* composition, the amount of nanoparticles for the selected *R/H* compositions was chosen to be always maximal with respect to the amount of hardener (i.e. *H/N* (*2/1*)).

To definitely avoid DGEBA monomer crystals the resin is heated for 15 minutes above the melting temperature T_m = 315 K [12] and then cooled to ambient temperature. The whole preparation takes place under normal room temperature and atmosphere conditions. The realisation of different mix-

ing sequences is achieved by stirring the alumina nanoparticles by hand for five minutes alternatively into the resin (→ (*R/N*)) or into the hardener (→ (*H/N*)) yielding the primary suspension. The lacking hardener respectively resin is mixed subsequently by hand for five minutes into this suspension. Typical sample masses amount to 6 to 8 grams. The time of adding the resin or the hardener to the primary suspension is always taken as the start of the chemical crosslinking. The crosslinking is performed isothermally at 298 K.

2.3. Experimental technique

2.3.1. Theoretical background

In this work high performance optical refractometry is used as a sensitive tool to probe the refractive index of isotropic materials at a wavelength of 589 nm. Based on the mean field theory developed by Clausius-Mosotti and Lorentz-Lorenz [13–16], the Lorentz-Lorenz equation (1) relates for non-interacting molecular systems the refractive index n_D to the mass density ρ:

$$\frac{n_D^2 - 1}{n_D^2 + 2} = r \cdot \rho \tag{1}$$

The specific refractivity r is defined by Equation (2):

$$r = \frac{N_A \alpha}{M_w 3\varepsilon_0} \tag{2}$$

where N_A is the Avogadro number, M_W the molecular mass, ε_0 the vacuum permittivity and α the locally averaged molecular polarisability. At the related frequencies (~$5 \cdot 10^{14}$ Hz) the molecular polarisability is purely electronic in origin. Considering non-interacting small molecules the specific refractivity appears as a constant. In this case the mass density ρ is directly proportional to the refractive index n_D, thus coupling optical properties to the packing of molecules. Equation (2) becomes meaningless for fully cured polymer networks since N_A and M_w are badly defined quantities. Therefore the proportionality discussed above is no more expected for thermosets.

Astonishingly, the Lorentz-Lorenz relation has been experimentally verified to be applicable to many classes of materials under different thermodynamic conditions, including isothermal curing of adhesives [17, 18]. In other words, the specific refractivity remains almost constant even in the case of molecular network formation in polymers. In this case the polarisability α is understood as a locally averaged quantity. 'Local' means in this context small in comparison to the wavelength of light, but large enough to get rid of the tensor properties of the molecular segments of polymers. As a result within the mean field approximation changes of the refractive index reflect variations of the molecular morphology either by changes of density or by small changes of the specific refractivity. From this discussion it is clear that optical refractometry gives no information on the discrete microscopic molecular structure but only on the average morphological properties in so far as they affect the optical polarisability or density. In this sense the refractive index is a highly sensitive tool to detect variations of the average molecular architecture [15, 16].

Beside the mean field approximation a spatial averaging takes place on the prism of the refractometer. For our instrument, the refractive indices are averaged over sample volumes of about ($5 \times 5 \times 0.5 \cdot 10^{-3}$) mm^3. Moreover, because of the high probe frequencies (10^{14}–10^{15} Hz) optical refractometry is not affected by relaxation processes which often hide information about quasi-static properties of the studied material while using experimental techniques with lower probe frequencies.

2.3.2. The refractometer

A modified high performance refractometer (Abbemat) from Anton Paar OptoTec, Seelze, Germany is used to investigate the refractive index of epoxy/alumina nanocomposites. A light source with a wavelength of 589 nm is used (sodium D line). The modification of the refractometer consists in a better temperature stabilisation of its detection system, the electronics and the sample. The resolution of the Abbemat is about 10^{-6}, the absolute accuracy about 10^{-5}. The curing measurements are performed at (298±0.01) K. Data recording is performed under the control of a LabView software developed to control and to record all relevant system parameters in the course of the isothermal measurements.

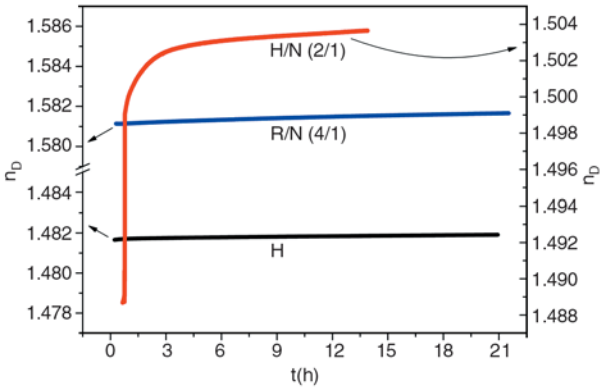

Figure 1. Isothermal temporal evolution at 298 K of the refractive index of the hardener (black curve), the alumina filled hardener *H/N* (*2/1*) (red curve) and the alumina filled resin *R/N* (*4/1*) (blue curve). The filled samples are measured after freshly stirring them.

3. Results and discussion

The basis for the current work is the expectation that there exist different interactions between the alumina nanoparticles and the hardener on one hand, and between the nanoparticles and the resin on the other. These differences are evidenced in Figure 1 by refractive index measurements performed on the primary suspensions *H/N* (*2/1*) and *R/N* (*4/1*). The mass concentrations (*2/1*) and (*4/1*) correspond to the composition related maximum concentration of alumina nanoparticles. During the preparation of the primary suspensions *H/N* (*2/1*) significant thixotropy is observed, which is not noticed in case of the filled resin *R/N* (*4/1*). This thixotropy of the nanoparticle filled hardener is synonymous to an increased viscosity of this sample after temporal relaxation of the material. This increase of the shear viscosity could be accompanied by a densification. According to Figure 1 the refractive index of the nanoparticle filled hardener relaxes during more than 14 hours after the mixing (order of magnitude: 10^{-2}), whereas the refractive index variation of the pure hardener is insignificant. Using Equation (1) this refractive index increase corresponds to a mass densification of about 1% for the nanoparticle filled hardener. The temporal refractive index changes of the filled resin are also completely negligible in comparison to that of the filled hardener. This confirms distinct interaction forces between the resin and the hardener molecules with the nanoparticles' surfaces.

As the hardener and the resin behave differently in presence of the nanoparticles, the question arises whether these different interaction forces play still a significant role while adding the missing reactant necessary to start the curing. Considering the starting conditions (different attraction forces between nanoparticles and the resin respectively the hardener, strong mixing of the missing reactant with the primary suspensions) leads us to the following hypotheses:

i. no differences in the refractive indices during the whole curing process,
ii. differences in the refractive indices at the beginning which are removed from the material in the course of curing or,
iii. differences in the refractive indices at the beginning which are partly maintained after curing.

At first, the curing behaviour of the nanocomposites based on the slightly over-stoichiometric epoxy *R/H* (*100/14*) is studied. A reliable interpretation of refractive index data needs a precise idea of the influence of errors performed during the sample preparation on the repeat accuracy. Therefore the pure over-stoichiometric epoxy *R/H* (*100/14*) and the nanocomposites based on the filled resin *R/N/H* (*100/7/14*) respectively on the filled hardener *H/N/R* (*14/7/100*) (mass ratios) are prepared independently at least three times and investigated as long as they are not too sticky. For the sake of clarity, only two curves are shown in Figure 2 for each type of sample. According to this figure the repeating accuracy (see grey curves) is convincing for

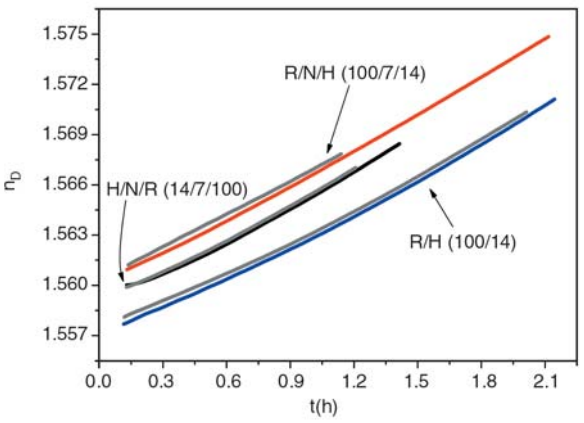

Figure 2. Temporal evolution of the refractive indices for *R/H* (*100/14*), for *R/N/H* (*100/7/14*) and *H/N/R* (*14/7/100*) during the curing at 298 K. For each kind of epoxy two measured curves are shown (the grey curves indicate the repeat accuracy).

each mixing sequence. Taking into account the high resolution of the refractometer the shift in the absolute refractive index values of the three groups of curves is reliable.

Considering the high refractive index of the alumina nanoparticles (n_D = 1.76) and assuming a simple mixing rule between the resin's, the hardener's and the nanoparticles' refractive indices, it seems reasonable that the nanocomposites show higher values than the pure epoxy during curing. Remarkably, during the whole time of the experiments remains a refractive index difference of $\Delta n_D \sim 10^{-3}$ for the two nanocomposites having the same composition. The fact that Δn_D exists at the start confirms the important role of the initial distribution of the three constituents. Within the measured time interval the three types of curves are shifted vertically against each other, but the time evolution is similar. The latter result confirms that the time evolution of the refractive indices stems from the curing of the epoxy. However, the observed time interval of curing is too short to extrapolate to the final state of isothermal curing.

Preliminary transmission electron microscope (TEM) measurements show that the nanoparticles in *H/N/R*-samples are more clustered than in *R/N/H*-samples. It should be stressed that TEM measurements do not distinguish between compact alumina aggregates and agglomerates of alumina particles glued together by a thin epoxy layer. Clouds of alumina particles covered with epoxy would behave optically more similar to a well-dispersed nanocomposite than to compact alumina clusters.

In order to test the influence of the cluster size of nanoparticles on the refractive index we have compared the refractive index of an alumina filled DGEBA DER 331 resin prepared by a mechanical dispersion technique (mean alumina cluster size: below 50 nm) [1] to that of hand-mixed alumina filled resin (mean alumina cluster size: below 300 nm). Astonishingly, both preparation techniques lead to samples showing within the margin of error the same refractive indices. The same agreement is found during the curing of such differently prepared composites by adding the same amount of hardener. Taking into account the high sensitivity of our refractometer this unexpected result seems to be due to a rather small dependence of the refractive index on the size of the alumina clusters, provided the total amount of nanoparticles remains constant. We therefore conclude that the observed changes in the refractive indices (related to the mixing sequence) are due to morphological changes in the polymer rather than to different cluster sizes of the alumina particles.

Without destroying the refractometer we have no access to the refractive indices in the further course of curing of the adhesives presented in Figure 2. In other words, the nanocomposites get really sticky during room temperature curing and even undergo glass transitions. The interesting information about the evolution of the refractive indices for different mixing sequences in the full course of curing up to the depletion of all amine groups can be obtained only for significantly under-stoichiometric compositions.

Four types of nanocomposites with different (under-stoichiometric) *R/H*-compositions, varying between (*100/1*) and (*100/7*) are investigated (see Figure 3). The almost horizontal time evolution of the refractive index after 10 h for the nanocomposites with the *R/H*-composition of (*100/1*) and (*100/2*) shows that the whole chemical crosslinking can be studied for these materials.

Applying a simple linear mixing rule to the refractive indices of the three constituents, the initial refractive indices of the nanocomposites (at t = 0 h) were estimated. Astonishingly, the estimated values are in agreement with the measured data within 1%.

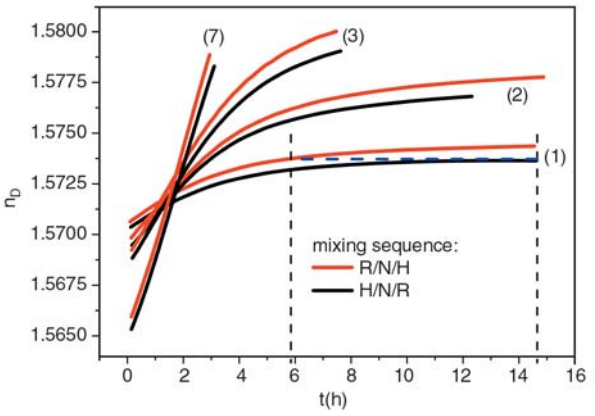

Figure 3. Influence of the mixing sequence (red or black lines) on the time evolution of the refractive index during the curing at 298 K of four kinds of nanocomposites: mass ratios for the constituents of samples (1): *R/N/H* (*100/0.5/1*); (2): *R/N/H* (*100/1/2*); (3): *R/N/H* (*100/1.5/3*) and (7): *R/N/H* (*100/3.5/7*).

The time evolution of the refractive indices shown in Figure 3 is in line with the results given in Figure 2: The refractive indices of the *R/N/H*-samples exceed those of the *H/N/R*-samples, even after long curing times when the chemical reaction has almost stopped due to the depletion of the amine groups. As a result, for a given hardener concentration the spread between corresponding curves increases with time. This contradicts the aforementioned hypotheses i. to iii.

Decreasing the hardener concentration, a decreasing spread is observed for a given curing time as also less nanoparticles are present. From our point of view it is really astonishing that even for the nanocomposites (*100/0.5/1*) and (*1/0.5/100*) a significant Δn_D is preserved in the long time limit. Consequently, as a function of curing time *R/N/H*- and *H/N/R*-samples do not develop the same morphology although they have the same global composition. The differences in the morphology between both kinds of mixing sequences tend to increase with curing time. As already mentioned, these differences stem from the polymer and not from the nanoparticles nor from the cluster sizes, but both take of course influence on the morphology of the polymer.

At least in principle the observed differences in molecular morphology evolution may be attributed to different curing rates. However, it is hard to understand why these hypothetical differences in reaction rate (as deduced from the refractive index) should be the largest in the almost finished curing regime. For the *R/N/H* (*100/0.5/1*) and *H/N/R* (*1/0.5/100*) samples the horizontal shift at the end of both curves would exceed eight hours as indicated by the blue dashed line. If a hindering of the chemical reactions can be excluded, it is likely that the constituting sequence is decisive for the related molecular morphologies in the course of the whole curing process. Accordingly the different morphologies are not temporary in nature but permanent.

The above discussed influence of the mixing sequence on the optical properties of epoxy/alumina nanocomposites has recently been observed also for a two component silicone rubber filled with alumina nanoparticles. The effect of the mixing sequence on the refractive index turns out to be even more pronounced.

4. Conclusions

High performance refractive index experiments have been performed during the isothermal curing of epoxy/alumina nanocomposites in order to investigate the role of the mixing sequence of the constituents. The results clearly show that the constituting sequence of DGEBA, DETA and alumina nanoparticles has an impact on the optical properties of the composites. As the optical polarisability of the nanoparticles is not expected to change during the curing process, the different temporal behaviour of the refractive index for several mixing sequences is indicative for different morphological evolutions in the course of curing.

Acknowledgements

Financial support was kindly obtained from the Ministère de la Culture, de l'Enseignement Supérieur et de la Recherche du Grand-Duché du Luxembourg.

References

[1] Wetzel B., Rosso P., Haupert F., Friedrich K.: Epoxy nanocomposites – fracture and toughening mechanisms. Engineering Fracture Mechanics, **73**, 2375–2398 (2006).

[2] Cao X., Lee L. J., Widya T., Macosko C.: Polyurethane/clay nanocomposites foams: Processing, structure and properties. Polymer, **46**, 775–783 (2005).

[3] Eschbach J., Rouxel D., Vincent B., Mugnier Y., Galez C., Le Dantec R., Bourson P., Krüger J. K., Elmazria O., Alnot P.: Development and characterization of nanocomposite materials. Materials Science and Engineering: C, **27**, 1260–1264 (2007).

[4] Blackman B. R. K., Kinloch A. J., Sohn Lee J., Taylor A. C., Agarwal R., Schueneman G., Sprenger S.: The fracture and fatigue behaviour of nano-modified epoxy polymers. Journal of Materials Science, **42**, 7049– 7051 (2007).

[5] Johnsen B. B., Kinloch A. J., Mohammed R. D., Taylor A. C., Sprenger S.: Toughening mechanisms of nanoparticle-modified epoxy polymers. Polymer, **48**, 530–541 (2007).

[6] Guo Z., Pereira T., Choi O., Wang Y., Hahn H. T.: Surface functionalized alumina nanoparticle filled polymeric nanocomposites with enhanced mechanical properties. Journal of Materials Chemistry, **16**, 2800–2808 (2006).

[7] Denq B-L., Hu Y-S., Chen L-W., Chiu W-Y., Wu T-R.: The curing reaction and physical properties of DGEBA/DETA epoxy resin blended with propyl ester phosphazene. Journal of Applied Polymer Science, **74**, 229–237 (1999).

[8] Altmann N., Halley P. J., Cooper-White J., Lange J.: The effects of silica fillers on the gelation and vitrification of highly filled epoxy-amine thermosets. Die Makromolekulare Chemie, Macromolecular Symposia, **169**, 171–177 (2001).
[9] Sanctuary R., Baller J., Krüger J. K., Schaefer D., Bactavatchalou R., Wetzel B., Possart W., Alnot P.: Complex specific heat capacity of two nanocomposite systems. Thermochimica Acta, **445**, 111–115 (2006).
[10] D'Ans J., Lax E.: Taschenbuch für Chemiker und Physiker, Band I–III. Springer, Berlin (1967).
[11] Possart W.: Adhesion, current research and applications. Wiley, Weinheim (2005).
[12] Flippen-Anderson J. L., Gilardi R.: Diglycidyl ether of bisphenol A (DGEBA). Acta Crystallographica, Section B, **37**, 1433–1435 (1981).
[13] Lorentz H. A.: Über die Beziehung zwischen der Fortpflanzungsgeschwindigkeit des Lichtes und der Körperdichte. Annalen der Physik und Chemie, **9**, 641–665 (1880).
[14] Lorenz L.: Über die Refractionsconstante. Annalen der Physik und Chemie, **11**, 70–103 (1880).
[15] Blythe T., Bloor D.: Electrical properties of polymers. Cambridge University Press, Cambridge (1979).
[16] Böttcher C. J. F.: Theory of electric polarization, vol 1.: Dielectrics in static fields. Elsevier, Amsterdam (1973).
[17] Müller U., Philipp M., Bactavatchalou R., Sanctuary R., Baller J., Zielinski B., Possart W., Alnot P., Krüger J. K.: Chemically induced transition phenomena in polyurethanes as seen by generalized mode Grüneisen parameters. Journal of Physics: Condensed Matter, **20**, 205101 (7pp) (2008).
[18] Krüger J. K., Alnot P., Baller J., Bactavatchalou R., Dorosz S., Henkel M., Kolle M., Krüger S. P., Müller U., Philipp M., Possart W., Sanctuary R., Vergnat C.: About the nature of the structural glass transition: an experimental approach. in 'Ageing and the Glass Transition' (eds.: Henkel M., Pleimling M. and Sanctuary R.) Springer, Berlin, 61–160 (2007).

eXPRESS Polymer Letters Vol.2, No.8 (2008) 553–559
Available online at www.expresspolymlett.com
DOI: 10.3144/expresspolymlett.2008.67

Selective Michael-type addition of a D-glucuronic acid derivative in the synthesis of model substances for uronic acid containing polysaccharides

*K. Bergman, J. Hilborn, T. Bowden**

Department of Materials Chemistry, Division of Polymer Chemistry, Uppsala University, Box 538, SE-751 21 Uppsala, Sweden

Received 8 May 2008; accepted in revised form 28 June 2008

Abstract. A flexible protocol for the preparation of model substances for uronic acid containing polysaccharides is presented. We have synthesized a D-glucuronic acid derivative which is designed so that it easily can be conjugated with different structures and architectures by selective Michael-type addition. By successful coupling of the glucuronic acid derivative to polyethylene glycol with high degree of conversion, products were obtained that were easily characterized and which resembled polysaccharides in terms of solubility and purification methods that could be employed. The model substance can potentially be used to facilitate optimization of low-degree modification reactions of high molecular weight D-glucuronic acid containing polysaccharides.

Keywords: *polymer gels, polysaccharides, Michael-type addition, model substance, NMR*

1. Introduction

Hydrogels are generally considered to be well suited as scaffolds for cell and tissue engineering applications due to their similarity to the natural extra cellular matrix [1–4]. Naturally occurring polysaccharides such as hyaluronic acid (hyaluronan) have received special attention for such purposes due to their biocompatibility and physiochemical properties [5]. Cross-linking of hyaluronic acid is a means to obtain an implantable hydrogel with controlled degradability and mechanical properties [6–8]. However, many cross-linking techniques employed today suffer drawbacks due to large degree modifications, which are necessary to compensate for the large extent of intramolecular reactions that occur when bifunctional cross-linkers are used [9]. In order to maintain the immunoneutrality and unique properties of native hyaluronic acid, it is suggested that the cross-linkable derivative should be modified to a low degree and synthesized under controlled conditions to avoid unwanted and unnecessary side reactions during modification and cross-linking. The degree of modification that can be performed without significantly altering properties of native hyaluronic acid depends on the type of modification and is a matter that deserves greater attention, although it is not a subject of further discussion in this report. Derivatives of uronic acid containing polysaccharides of high molecular weight which are modified to a low degree are difficult to characterize. To address this issue we have developed a synthetic protocol for the preparation of a model substance consisting of a novel D-glucuronic acid derivative that is conjugated with polyethylene glycol (PEG) (Figure 1). D-glucuronic acid is found in the disaccharide

*Corresponding author, e-mail: bowden@mkem.uu.se

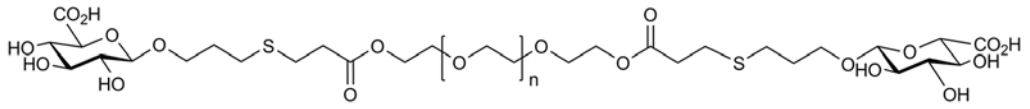

Figure 1. Structure of model substance for uronic acid containing polymers

repeat unit of hyaluronic acid and contains both a carboxylic acid and hydroxyl groups, which are the main targets for performing modifications. The model substance is an ideal candidate for optimizing modification reactions since the process can be followed by nuclear magnetic resonance (NMR), which otherwise is difficult due to the low degree of modification and high molecular weight of hyaluronic acid. Coupling the glucuronic acid derivative with PEG has added the feature to the model substance in the sense that it can be purified by techniques commonly used for polysaccharides, such as gel-filtration and dialysis. The glucuronic acid derivative is designed so that it can be easily combined with different structures and architectures by selective Michael-type addition, making it possible to obtain a substance easy to characterize yet large enough to handle purification wise.

2. Experimental procedures

2.1. Materials and methods

Polyethylene glycol with a molecular weight of 2000 g/mol (PEG2000), purchased from VWR, and polyethylene glycol diacrylate with a molecular weight of 700 Da (PEGDA700), from Aldrich, were used without further purification. Prior use, dichloromethane (VWR) was washed three times with de-ionized water, dried over $MgSO_4$, filtered, refluxed over CaH_2, distilled and stored over argon. Methanol (VWR) was refluxed over CaH_2, distilled and stored over argon. All other chemicals were purchased of reagent grade or of higher purity from Aldrich, ACROS Organics, ABCR or VWR and were used without further purification. Column chromatography was performed on silica gel 60 G (Merck) and monitored by thin layer chromatography (TLC) on fluorescent silica gel coated plates (Merck). ^{1}H NMR and ^{13}C NMR analyses were performed on a JEOL ECP 400 MHz spectrometer with the solvent signal as an internal standard. FT-IR spectra were recorded on a Perkin-Elmer Spectrum One spectrometer. Molecular mass and molecular mass distribution of the final products were obtained by matrix assisted laser desorption ionization time-of-flight mass spectrometry (MALDI-TOF MS) using a Bruker UltraFlex system with a SCOUT-MTP ion source (Bruker Daltonics, Bremen, Germany) operating in reflection mode and with 2,5-dihydroxybenzoic acid (DHB) as matrix. Samples were prepared in de-ionized water by mixing 5 µl of product (1 mg/ml) with 20 µl of DHB (10 mg/ml). Melting point was determined by differential scanning calorimetry (DSC-Q1000, TA Instruments).

2.2. Synthesis of PEG diacrylate

PEG2000 (5 g) was dissolved in 100 ml toluene and dried azeotropically. Toluene was removed by rotary evaporation and the residue dried in vacuum. The dried polymer (1 g, 1 mmol functional groups) was dissolved in 10 ml freshly distilled dichloromethane under nitrogen while cooling in an ice-bath. To the solution was added 0.25 ml acrylic anhydride (2.2 mmol) and 0.3 ml triethylamine (2.2 mmol) and the reaction proceeded while stirring in the dark overnight at room temperature. The volume of the solution was reduced by rotary evaporation and the product (PEGDA2000) was collected by precipitation in cold diethyl ether, filtered and dried in vacuum. Yield: 89%. ^{1}H NMR (DMSO-d_6): δ (ppm) = 3.51 (s, ~234H, PEG main chain), 3.64 (t, 4H, OC*H*$_2$CH$_2$OCOCH=CH$_2$), 4.22 (t, 4H, OCH$_2$C*H*$_2$OCOCH=CH$_2$), 5.96 (dd, 2H, *J* 10.3 Hz and 1.5 Hz, OCH$_2$CH$_2$OCOC*H*=CH$_2$), 6.20 (dd, 2H, *J* 17.2 Hz and 10.3 Hz, OCH$_2$CH$_2$OCOCH=C*H*$_2$) and 6.34 (dd, 4H, *J* 17.2 Hz and 1.46 Hz, OCH$_2$CH$_2$OCOCH=C*H*$_2$). FTIR: ν (cm^{-1}) = 2883 (C–H), 1724 (C=O), 1467 (CH$_2$), 1342, 1279, 1241, 1194, 1106, 960 and 842 (C–O–C).

2.3. Synthesis of methyl (benzoyl 2,3,4-tri-*O*-benzoyl-α-D-glucopyranoside) uronate, 1

To a solution of powdered NaOH (20 mg, 0.5 mmol) in 40 ml freshly distilled methanol was added 4 g D-glucofurano-6,3-lactone (22.7 mmol) followed

by stirring in room temperature for 10 hours. The solution was concentrated by evaporation, the residue dissolved in 50 ml pyridine and cooled to 0°C. Benzoyl chloride (16 ml, 139 mmol) was added to the solution and stirred at room temperature overnight. The reaction mixture was diluted with 40 ml ice-cold de-ionized water and 400 ml dichloromethane, and then washed with saturated aqueous $NaHCO_3$ and water. The organic phase was dried over Na_2SO_4 and concentrated by evaporation. The residue was purified by flash silica chromatography [heptane – ethyl acetate (3:2)] to give **1** as a mixture of the α and β anomers, 9.35 g (66%). ^{1}H NMR ($CDCl_3$): δ (ppm) = 3.59 (s, 3H, CO_2CH_3 β), 3.68 (s, 3H, CO_2CH_3 α), 4.62 (d, 1H, *J* 8.4 Hz, H-5 β), 4.77 (d, 1H, *J* 9.9 Hz, H-5 α), 5.70 (dd, 1H, *J* 10.3 Hz and 3.7 Hz, H-2 α), 5.77 (t, 1H, H-4 α), 5.83 (m, 2H, H-2 and H-4 β), 6.02 (t, 1H, H-3 β), 6.32 (m, 2H, H-1 β and H-3 α), 6.92 (d, 1H, *J* 3.7 Hz, H-1 α) and 7.28–8.15 (m, 20H, Ph).

2.4. Synthesis of methyl (2,3,4-tri-*O*-benzoyl-α-D-glucopyranosyl bromide) uronate, 2

To 9 g of **1** (14.4 mmol) was added 36 ml HBr (33% in acetic acid) followed by stirring in room temperature for 12 hours. The mixture was cooled to 0°C, diluted with 180 ml ice-cold dichloromethane and washed with saturated aqueous $NaHCO_3$, de-ionized water and brine. The organic phase was dried over $MgSO_4$, concentrated by evaporation and the residue dried in vacuum to give **2**, 7.8 g (93%). ^{1}H NMR ($CDCl_3$): δ (ppm) = 3.69 (s, 3H, CO_2CH_3), 4.85 (d, 1H, *J* 10.3 Hz, H-5), 5.34 (dd, 1H, *J* 9.9 Hz and 4.0 Hz, H-2), 5.72 (t, 1H, H-4), 6.27 (t, 1H, H-3), 6.85 (d, 1H, *J* 4.0 Hz, H-1) and 7.30–7.99 (m, 15H, Ph).

2.5. Synthesis of Methyl (Allyl 2,3,4-Tri-*O*-benzoyl-β-D-glucopyranoside) uronate, 3

Compound **2** (3.35 g, 5.7 mmol) was dissolved in 60 ml freshly distilled dichloromethane together with activated 4 Å molecular sieves under N_2 in a two-armed round-bottomed flask equipped with a condenser. To the solution was added 2 ml allyl alcohol (29.4 mmol) and 1.58 g Ag_2CO_3 (5.7 mmol). After stirring at 30°C for 48 hours the solution was filtered and concentrated by evaporation. The residue was purified by flash silica chromatography [hexane – ethyl acetate (3:2)] to give **3**, 1.50 g (47%). ^{1}H NMR ($CDCl_3$): δ (ppm) = 3.70 (s, 3H, CO_2CH_3), 4.17 (m, 1H, $OCH_2CH{=}CH_2$), 4.34 (d, 1H, *J* 9.5 Hz, H-5), 4.42 (m, 1H, $OCH_2CH{=}CH_2$), 4.91 (d, 1H, *J* 7.3 Hz, H-1), 5.16 and 5.26 (m, 2H, $OCH_2CH{=}CH_2$), 5.56 (dd, 1H, *J* 9.2 Hz and 7.7 Hz, H-2), 5.69 (t, 1H, H-4), 5.79 (m, 1H, $OCH_2CH{=}CH_2$), 5.90 (t, 1H, H-3) and 7.28– 7.96 (m, 15H, Ph). ^{13}C NMR ($CDCl_3$): δ (ppm) = 53.0, 70.2, 70.3, 71.6, 72.1, 73.0, 99.7, 118.2, 128.4–128.5, 129.9, 133.2-133.5, 165.1, 165.3, 165.7 and 167.5.

2.6. Synthesis of methyl (3-thioacetoxypropyl 2,3,4-tri-*O*-benzoyl-β-D-glucopyranoside) uronate, 4

To a solution of 41 mg 2,2′-Azobis(2-methylpropionitrile) (AIBN, 0.25 mmol) in 8.5 ml dioxane was added 560 mg of **3** (1 mmol). The solution flask was flushed with argon gas and cooled on ice, and 1.1 ml thioacetic acid (15.3 mmol) added. The mixture was subjected to a freeze-vacuum-thaw process three times, purged with argon gas and stirred at 75°C for 4 hours. The reaction was quenched by flushing with air, the solution concentrated by evaporation from toluene and the product purified by flash silica chromatography [hexane – ethyl acetate (gradient, 95–67% hexane)] to give **4**, 390 mg (61%). ^{1}H NMR ($CDCl_3$): δ (ppm) = 1.83 (m, 2H, $OCH_2CH_2CH_2SCOCH_3$), 2.24 (s, 3H, $SCOCH_3$), 2.81 (m, 2H, $OCH_2CH_2CH_2SCOCH_3$), 3.59 (m, 1H, $OCH_2CH_2CH_2SCOCH_3$), 3.69 (s, 3H, CO_2CH_3), 4.02 (m, 1H, $OCH_2CH_2CH_2SCOCH_3$), 4.34 (d, 1H, *J* 9.5 Hz, H-5), 4.84 (d, 1H, *J* 7.3 Hz, H-1), 5.52 (dd, 1H, *J* 9.5 Hz and 7.3 Hz, H-2), 5.67 (t, 1H, H-4), 5.90 (t, 1H, H-3) and 7.28–7.96 (m, 15H, Ph). ^{13}C NMR ($CDCl_3$): δ (ppm) = 25.7, 29.4, 30.6, 53.0, 68.7, 70.3, 71.6, 72.1, 73.0, 101.2, 128.4–129.2, 129.9, 133.4–133.6, 165.1, 165.3, 165.7, 167.5 and 195.9.

2.7. Synthesis of PEG diglucuronic acid, 5a and 5b

To a sealed round-bottomed flask thoroughly purged with nitrogen gas containing 150 mg of **4** (0.24 mmol) was added a degassed methanol –

deionized water mixture (5:1, 9 ml). The mixture was heated to 55°C and stirred until dissolution before cooling in ice and adding 1.5 ml degassed 3 M NaOH. After stirring at room temperature for 6 hours the solution was transferred to Dowex H^+ 50×8–100 sulfonic resin (Aldrich) in a sealed flask flushed with nitrogen gas and stirred at room temperature for 20 minutes. The solution was transferred to a sealed flask flushed with nitrogen gas, containing 50 mg PEGDA700 (0.14 mmol functional groups). A degassed 0.5 M $NaHCO_3$-solution was added until pH 9 was reached and the flask was agitated at room temperature for 15 hours. Methanol was removed by evaporation and the residue purified by gel-filtration using a Sephadex-G25 PD-10 pre-packed column (Amersham Biosciences). The eluted solution was mixed with Dowex H^+ and lyophilized to give **5a** as a yellow resin. Yield: 73 mg (83%). ^{1}H NMR (D_2O): δ (ppm) = 1.87 (m, 4H), 2.65, 2.71 and 2.80 (t, 4H each), 3.28 (t, 2H), 3.51 (m, 4H), 3.61–3.72 (m, ~60H), 3.75 (t, 4H), 3.94 (m, 4H), 4.26 (t, 4H) and 4.48 (d, 2H, *J* 8.0 Hz). Assignments of ^{1}H NMR-peaks are demonstrated in Figure 2. ^{13}C NMR (D_2O): δ (ppm) = 26.3, 27.7, 28.9, 34.3, 64.2, 68.6, 69.2, 69.7, 71.5, 72.9, 74.8, 75.4, 102.5, 172.6 and 174.7. MS (MALDI-TOF): M_n = 1231, M_w = 1243 and M_w/M_n = 1.01. Compound **5b** was synthesized with PEGDA2000 according to the preparation of **5a** and purified by dialysis (Spectra/Por 6 RC Dialysis membrane tubing MWCO 1000) followed by mixing with Dowex H^+ and freeze-drying. Yield: 106 mg (57%). ^{1}H NMR (D_2O): δ (ppm) = 1.87 (m, 4H), 2.64, 2.70 and 2.80 (t, 4H each), 3.27 (t, 2H), 3.51 (m, 4H), 3.60–3.72 (m, ~246H), 3.75 (m, 4H), 3.93 (m, 4H), 4.26 (t, 4H) and 4.47 (d, 2H, *J* 8.0 Hz). ^{13}C NMR (D_2O): δ (ppm) = 26.3, 27.6, 29.0, 34.3, 64.2, 68.6, 69.2, 69.7, 71.5, 72.9, 74.8, 75.4, 102.5, 172.7 and 174.7. MS (MALDI-TOF): M_n = 2545, M_w = 2565 and M_w/M_n = 1.01. T_m = 40–49°C.

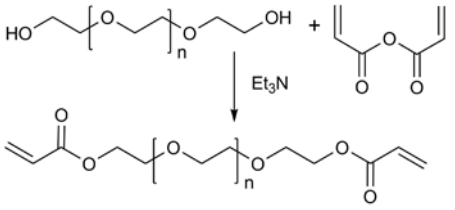

Figure 2. Synthesis of PEG diacrylate

3. Results and discussion

The model substance is versatile in the sense that the glucuronic acid derivative easily can be combined with appropriate macromolecules through a selective Michael-type addition that previously has been described by Lutolf *et al*. [10]. In this study PEG was chosen, which simplifies characterization with NMR spectroscopy due to the absence of functional groups on the main chain and brings properties to the model substance resembling hyaluronic acid in terms of solubility and purifica-

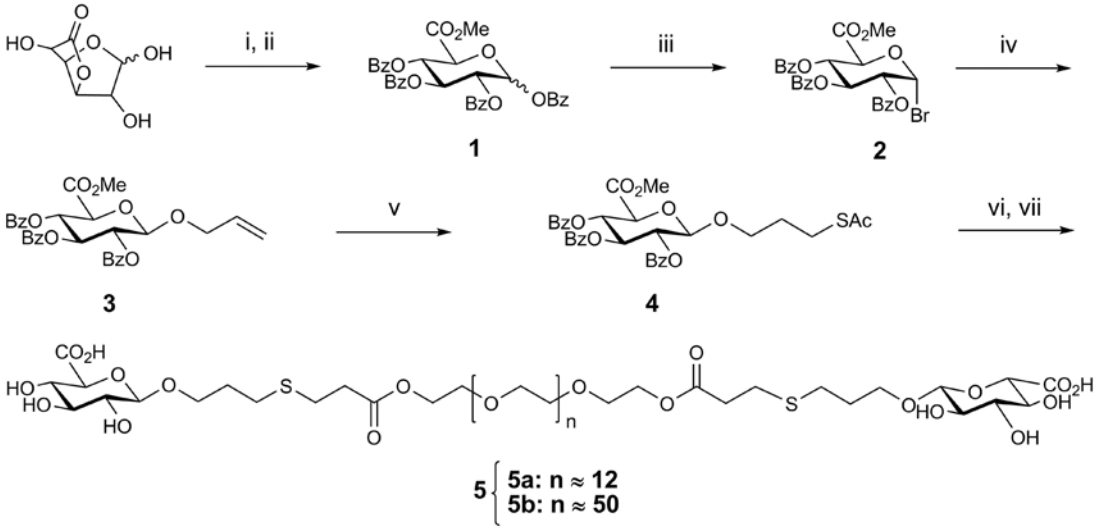

Figure 3. Synthesis of PEG diglucuronic acid. Reagents and conditions: : i) MeOH, NaOH, 10 h; ii) Pyridine, PhCOCl, overnight; iii) HBr 33% in AcOH, room temperaure, 12 h; iv) Allyl alcohol, Ag_2CO_3 30°C 48 h; v) AcSH, AIBN 75°C 4 h; vi) NaOH (3 M), 6 h, then Dowex H^+; vii) PEGDA, $NaHCO_3$ (0.5 M) pH 9, 15 h, then Dowex H^+

tion methods that can be utilized. PEG diacrylate was successfully synthesized from PEG with a molecular weight of 2000 g/mol according to Figure 2, whereas PEG diacrylate with a molecular weight of 700 g/mol was found commercially available.

The strategy employed for synthesizing the model substance (Figure 3) involved five steps beginning with the preparation of a benzoyl protected glucopyranoside uronate as a mixture of the α and β anomers (**1**), which further was converted to an α bromide (**2**) using methods previously published by

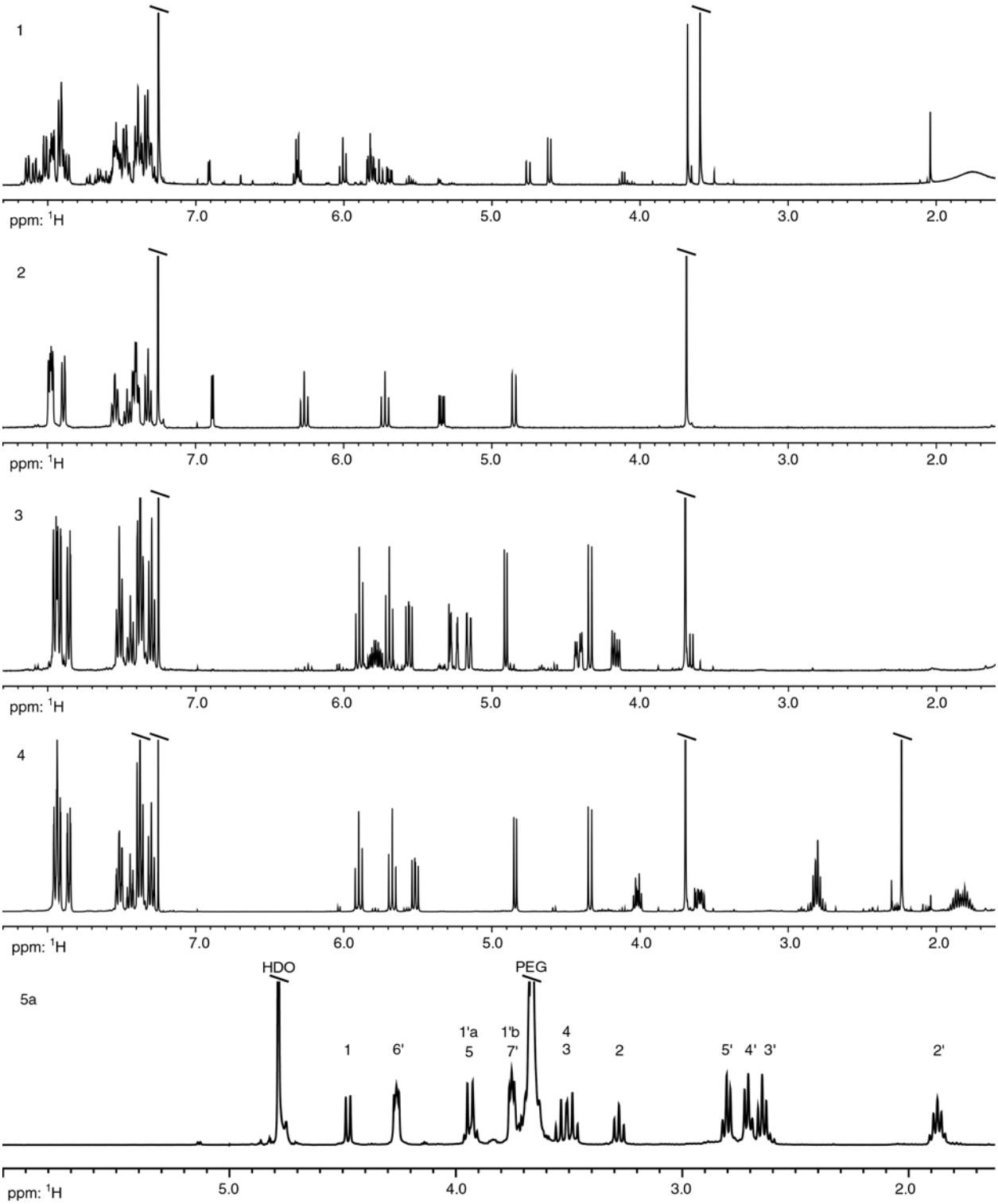

Figure 4. ^{1}H NMR spectra of compounds **1**–**5a** recorded at 400 MHz. Peaks for substance **5a** are assigned labels according to IUPAC nomenclature

Coutant and Jacquinet [11]. In the following step allyl alcohol was introduced to the bromide, which proved most successful by the classical Koenigs-Knorr glycosylation in the presence of silver carbonate [12]. Radical elongation of **3** with thioacetic acid afforded **4**, which was further converted to a thiol and simultaneously deprotected by treatment of sodium hydroxide under nitrogen while cooling. Deprotection performed without cooling, under otherwise same conditions, resulted in the formation of β-elimination product. An excess of the thio-glycoside was coupled with PEGDA under nitrogen without prior purification in order to avoid disulfide formation, and resulted in high yields of product (**5a** and **5b**). Although disulfides are readily formed in the presence of oxygen, thiols have shown to be ideal for the Michael-type addition to unsaturated esters [10]. The products were appropriately purified to remove salts and excess starting material.

Characterization of the final products (**5a** and **5b**) with NMR spectroscopy confirmed a high purity and a full conversion, as indicated by the complete absence of signals from acrylate protons and by the ratio of integrated signals originating from the anomeric protons on the glucuronic acid moieties (δ = 4.48 ppm) and protons on the main chain of PEG (δ = 3.65 ppm). A typical ^{1}H NMR spectrum of the model substance (**5a**) is demonstrated in Figure 4, along with spectra for compounds **1**–**4**. Performing COSY NMR experiments enabled assignment of overlapping signals. MALDI-TOF MS was used to determine molecular mass and molecular mass distributions of the conjugates, which also confirmed a high conversion degree. A typical MALDI-TOF mass spectrum of the model substance with uniformly distributed 44 g/mol spaced lines attributed to the PEG repeat unit is provided in Figure 5.

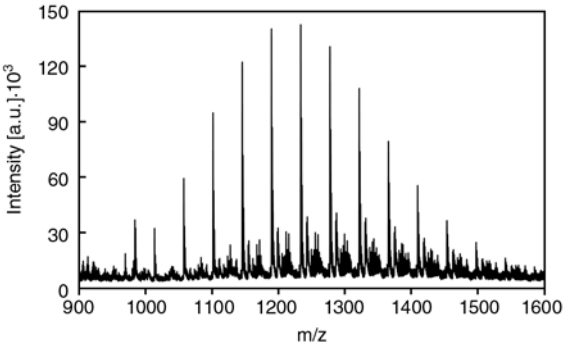

Figure 5. MALDI-TOF mass spectrum of PEG diglucuronic acid (**5a**)

On one hand, the higher molecular weight conjugate (**5b**) has the advantage of being solid at room temperature, adding the possibility to purify by precipitation. On the other hand a model substance with lower molecular weight (e.g. **5a**) is preferred characterization wise. In addition to use the glucuronic acid derivative as model substances for optimizing modification reactions, it may be used for the preparation of glycoconjugates that are of interest in the study of the biological role of carbohydrates. Although the described model substance currently is used for the development of new cross-linking chemistry for hyaluronic acid, it may also be applied for other D-glucuronic acid containing polysaccharides such as chondroitin sulfate, heparin and heparan sulfate.

4. Conclusions

A protocol for the preparation of a model substance for uronic acid containing polysaccharides has been developed. The model substance consists of a D-glucuronic acid – PEG conjugate which was synthesized in five steps. Selective Michael-type addition enabled coupling of the thiolated D-glucuronic acid derivative with full conversion to PEG-diacrylate of two different molecular weights. By conjugating the glucuronic acid derivative with different structures and architectures it is possible to obtain model substances which resemble polysaccharides while at the same time are easier to characterize. We believe that the protocol is a flexible route to the preparation of model substances which can be used in the optimization of modification reaction for high molecular weight polysaccharides.

Acknowledgements

The Swedish Research Council (VR) is acknowledged for the financial support of this work.

References

[1] Lee K. Y., Mooney D. J.: Hydrogels for tissue engineering. Chemical Reviews, **101**, 1869–1879 (2001).

[2] Hoffman A. S.: Hydrogels for biomedical applications. Advanced Drug Delivery Reviews, **54**, 3–12 (2002).

[3] Hubbell J. A.: Synthetic biodegradable polymers for tissue engineering and drug delivery. Current Opinions in Solid State and Materials Science, **3**, 246–251 (1998).

[4] Nitschke M., Götze T., Gramm S., Werner C.: Detachment of human endothelial cell sheets from thermoresponsive poly(NiPAAm-co-DEGMA) carriers. Express Polymer Letters, **1**, 660–666 (2007).

[5] Atala A., Lanza R. P.: Methods of tissue engineering. Academic Press, San Diego (2002).

[6] Campoccia D., Doherty P., Radice M., Brun P., Abatangelo G., Williams D. F.: Semisynthetic resorbable materials from hyaluronan esterfication. Biomaterials, **19**, 2101–2127 (1998).

[7] Shu X. Z., Liu Y., Luo Y., Roberts M. C., Prestwich G. D.: Disulfide cross-linked hyaluronan hydrogels. Biomacromolecules, **3**, 1304–1311 (2002).

[8] Segura T., Anderson B. C., Chung P. H., Webber R. C., Shull K. R., Shea L. D.: Crosslinked hyaluronic acid hydrogels: A strategy to functionalize and pattern. Biomaterials, **26**, 359–371 (2005).

[9] Ossipov D. A., Hilborn J.: Poly(vinyl alcohol)-based hydrogels formed by 'click chemistry'. Macromolecules, **39**, 1709–1718 (2006).

[10] Lutolf M. P., Tirelli N., Cerritelli S., Cavalli L., Hubbell J. A.: Systematic modulation of Michael-type reactivity of thiols through the use of charged amino acids. Bioconjugate Chemistry, **12**, 1051–1056 (2001).

[11] Coutant C., Jacquinet J-C.: 2-deoxy-2-trichloroacetamido-D-glucopyranose derivatives in oligosaccharide synthesis: From hyaluronic acid to chondroitin 4-sulfate trisaccharides. Journal of the Chemical Society: Perkin Transactions 1, **12**, 1573–1581 (1995).

[12] Koenigs W., Knorr E.: Über einige Derivate des Traubenzuckers und der Galactose. Berichte der Deutsche Chemische Gesellschaft, **34**, 957–981 (1901).

eXPRESS Polymer Letters Vol.2, No.8 (2008) 560–568
Available online at www.expresspolymlett.com
DOI: 10.3144/expresspolymlett.2008.68

Relationship between fiber degradation and residence time distribution in the processing of long fiber reinforced thermoplastics

H. Zhuang, P. Ren, Y. Zong, G. C. Dai*

State Key Laboratory of Chemical Engineering, East China University of Science and Technology, 200237 Shanghai, China

Received 14 May 2008; accepted in revised form 29 June 2008

Abstract. Long fiber reinforced thermoplastics (LFT) were processed by in-line compounding equipment with a modified single screw extruder. A pulse stimulus response technique using PET spheres as the tracer was adopted to obtain residence time distribution (RTD) of extrusion compounding. RTD curves were fitted by the model based on the supposition that extrusion compounding was the combination of plug flow and mixed flow. Characteristic parameters of RTD model including P the fraction of plug flow reactor (PFR) and d the fraction of dead volume of continuous stirred tank reactor (CSTR) were used to associate with fiber degradation presented by fiber length and dispersion. The effects of screw speed, mixing length and channel depth on RTD curves, and characteristic parameters of RTD models as well as their effects on the fiber degradation were investigated. The influence of shear force with different screw speeds and variable channel depth on fiber degradation was studied and the main impetus of fiber degradation was also presented. The optimal process for obtaining the balance of fiber length and dispersion was presented.

Keywords: *polymer composites, reinforcements, fiber degradation, RTD, LFT*

1. Introduction

Fiber reinforced thermoplastics are widely used for the advantages of weight savings, low production costs, and freedom of design. Long fiber reinforced thermoplastics (LFT) have been confirmed to possess significant improvement in the properties of stiffness, strength, and toughness over their counterparts of short fiber reinforced thermoplastics. Because of excellent mechanical properties, low production cost and good environmental protection, LFT has been broadly applied in the automotive industry over the last decade [1–2].

Longer fiber length and better fiber dispersion are the key factors to obtain excellent mechanical properties of LFT. The instance is that longer fiber length is in favor of enhancing strength and toughness, and the improvement of fiber dispersion is beneficial to increase stiffness [3]. However, fiber length was reduced seriously by undergoing interaction between fiber-equipment, fiber-fiber, and fiber-matrix during extrusion compounding of LFT [4]. As to fiber degradation indicated by fiber length and dispersion, the reduction of fiber length had been investigated, but few studies were focusing on fiber dispersion so far [5]. There is a conflict of factors which influence fiber length and dispersion during extrusion compounding of LFT, and how to obtain the optimal balance of fiber length and dispersion is the purpose of this study.

In the mixing process of polymer system, residence time distribution (RTD) plays a significant role in determining mixing capacity as well as components

*Corresponding author, e-mail: zhuanghui@vip.citiz.net

uniformity [6–7]. The extrusion compounding of polymer reaction, immiscible blend and reinforced plastics had been investigated by RTD analysis.

Measurements of RTD in a single-screw extruder were carried out during experimental studies of controlled chemical degradation of polypropylene (PP). A radioactive tracer method was employed, and the effect of screw speed, temperature, and reaction on RTD curves were examined [8]. In an extruder, the effect of screw configuration on residence time and mixing efficiency was studied for an immiscible PA6/PP blend. RTD was used to indicate the total mixing efficiency, and its association with the dispersion of minor phase [9]. The mechanism of fiber fracture and methods to reduce it through process improvement and machine design in fiber reinforced composites were studied by Karthik Ramani *et al*. It is found that the residence time, fill-up, and the intensity of mixing during extrusion compounding have a predominant effect on fiber fracture [10].

RTD can be studied by the introduction of a pulse tracer or by introduction of a step change in the concentration [11]. Also RTD can be determined by an analysis of melt flow, but it is very complicated. An alternative analysis is the construction of a flow pattern with conceptual models. The most widely reported models include a combination of plug flow and mixed flow [12–13]. Mean residence time (MRT) was used for evaluating the extent of fiber fracture, but no paper was reported using the RTD model for the evaluations between processing condition, machine design and fiber fracture.

In-line compounding equipment modified with a single screw extruder was used for processing LFT. PP and glass fiber were added into the extruder from primary hopper and downstream hopper respectively. Three factors of screw speed, mixing length, and channel depth which affected RTD curves were studied. Two characteristic parameters of RTD model were used for characterizing RTD curves. The effects on fiber degradation presented by fiber length and fiber dispersion were studied. Fiber degradation was associated with two characteristic parameters of RTD model, and also with above three factors. The influence of shear force with different screw speeds and variable channel depth on fiber degradation was studied and the main impetus of fiber degradation was also presented. The optimal process for obtaining the balance of fiber length and dispersion was the purpose of the study.

2. Experiment

2.1. Materials

Homo-polymer polypropylene (Y1600, Shanghai Petrochemical Co., Ltd., China) was used as matrix resin. Its melt flow index was 16.0 g/min at 230°C. Glass fiber of direct roving with filament diameter 17 μm (GF362, Jushi Group Co., Ltd., China) was used as the reinforcement.

2.2. Experimental condition

A modified single screw extruder SJ-45B from Beijing Plastics Machinery Institute (screw diameter was 45 mm and length to diameter ratio was 30) was used for processing LFT. Free flow screw of three leads was used for the study of extrusion compounding shown in Figure 1. Three screws of different channel depth (H_1 = 3 mm, H_2 = 6 mm and H_3 = 9 mm) were used in the study. Channel depth of 6 mm would be used unless otherwise noted.

As shown in Figure 2, three hoppers were equipped on the extruder, and the length from the first and the second hopper to the exit was 500 mm (L_1 = 500 mm) and 250 mm (L_2 = 250 mm) respectively. Mixing length was defined by the length from the first hopper or the second hopper to the exit. Unless otherwise noted, mixing length was 500 mm. PP was added into the extruder from the primary hopper. Extrusion temperature was controlled between 200 and 220°C. Glass fiber, at 30%

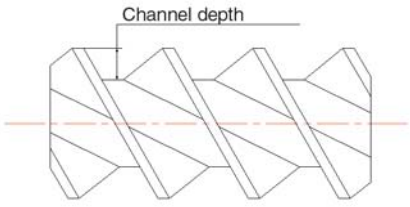

Figure 1. Schematic diagram of free flow screw

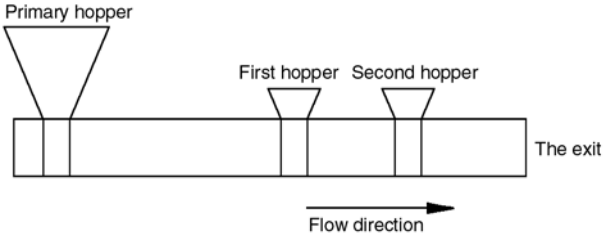

Figure 2. Diagram of the modified single screw extruder

of both PP and glass fiber by weight, was added into the extruder from the first hopper or the second hopper. The extrudate was processed into plates of requested size by a calender, for analysis and testing purpose. Four screw speeds (n_1 = 45.0 rpm, n_2 = 54.0 rpm, n_3 = 67.5 rpm, and n_4 = 81.0 rpm) were investigated.

2.3. Fiber length and dispersion

The fiber length measurements were conducted with a semi-image analyzer system. The matrix PP was removed by burning the plate off in a muffle furnace maintained at 500°C for 4 hr. The recovered glass fibers were dispersed in silicone-water suspension, and then the lengths of at least 800 fibers were measured by the semi-image analyzer system. Fiber length presented by number average (L_n) was determined in Equation (1):

$$L_n = \frac{\sum N_i L_i}{\sum N_i} \tag{1}$$

Fiber dispersion is defined as the weight fraction of fiber filaments in total glass fiber. After the matrix PP was direct burnt in a muffle furnace maintained at 500°C for 4 hr, the weight of residual ash was defined as W_0, and fiber bundles, which were not dispersed into fiber filaments selected manually was defined as W_1. Fiber dispersion was determined in Equation (2):

$$Dispersion = \frac{W_0 - W_1}{W_0} \tag{2}$$

2.4. RTD test

RTD curve was obtained using a pulse stimulus response technique, with black PET/poly (ethylene terephthalate) spheres as the tracer. 500 particles of the tracers were added into the extruder from the hopper that glass fiber had introduced, and the time was recorded simultaneously. The extruding plate of 100 mm width and 8 mm thickness was collected and black tracers in translucence PP can be seen clearly. The number of the tracers was counted at same time interval, and the fraction of the tracers in different time was obtained for RTD analysis. RTD curves were described as $F(\theta)$ versus θ curve. Mathematically, these relations are described by Equations (3) and (4):

$$E(t) = \frac{C}{\int_0^\infty C\mathrm{d}t} = \frac{C_i}{\sum C_i \Delta t_i} \tag{3}$$

$$F(t) = \int_0^\infty E(t)\mathrm{d}t = \frac{\sum_{i=0}^{t} C_i \Delta t}{\sum C_i \Delta t_i} \tag{4}$$

where C_i is the tracer concentration at time t.

The characteristic parameter of RTD curve, mean residence time (MRT) was calculates by Equation (5):

$$MRT = \int_0^\infty tE(t)\mathrm{d}t = \frac{\sum t_i C_i \Delta t_i}{\sum C_i \Delta t_i} \tag{5}$$

In order to compare RTD curves under different processing conditions, normalized time θ was defined by Equation (6):

$$\theta = \frac{t}{MRT} \tag{6}$$

and $F(\theta)$ was defined by Equation (7):

$$F(\theta) = F(t) \tag{7}$$

RTD curves of extrusion compounding at four screw speeds, two mixing length and three channel depth values have been measured. The analysis results of RTD curves were used to explain flow behavior of extrusion compounding, and more were associated with fiber degradation.

2.5. RTD model

The RTD curves were first modeled by considering extrusion compounding as the combination of mixed flow and plug flow by Wolf and Rescnick (1963). The model named Wolf model is expressed by Equation (8) [14]:

$$F(\theta) = u(\theta)\left[1 - e^{-\frac{\theta - P}{1-P}}\right] \tag{8}$$

$$u(\theta) = 0, \theta < P;\ u(\theta) = 1, \theta \geq p$$

where P is the fraction of PFR (plug flow reactor).

The flow in CSTR was taken for mixed flow and the flow in PFR was considered as plug flow, so Yeh *et al.* introduces *d*, the fraction of dead volume in CSTR into Wolf model, so the model named Yeh model is expressed by Equation (9) [15]:

$$F(\theta) = u(\theta)\left[1 - e^{-\frac{\theta - P}{(1-d)(1-P)}}\right] \quad (9)$$

$$u(\theta) = 0, \theta < P; \;\; u(\theta) = 1, \theta \geq p$$

The parameters *d* and *P* of above two models can be obtained by non-linear regression calculation, and were associated with fiber degradation.

3. Results and discussion

3.1. RTD model

RTD curve was shown as $F(\theta)$ versus θ for 81.0 rpm screw speed and 6 mm channel depth in Figure 3. The RTD curve suggested that flow behavior was between plug flow and mixed flow. There was some declination between Wolf model and experimental data; but the consistency between Yeh model and experimental data was good.

Parameter values derived from Wolf model and Yeh model were listed in Table 1. In Yeh model, additional parameter *d*, the fraction of dead volume in CSTR was presented besides *P*, the fraction of PFR indicted in Wolf model. As shown in Figure 3, Yeh model was better than Wolf model for fitting experimental data. The existence of parameter *d* indicated there was some flow-limited area during extrusion compounding.

3.2. Influence of processing factors

3.2.1. Screw speed

RTD curves with 6mm channel depth was illustrated in Figure 4 by $F(\theta)$ versus θ for different screw speeds. It suggested that the flow behavior of extrusion compounding was between plug flow and mixed flow.

Parameters values derived from Yeh model at different screw speeds were listed in Table 2. The fraction of PFR *P* and the fraction of dead volume

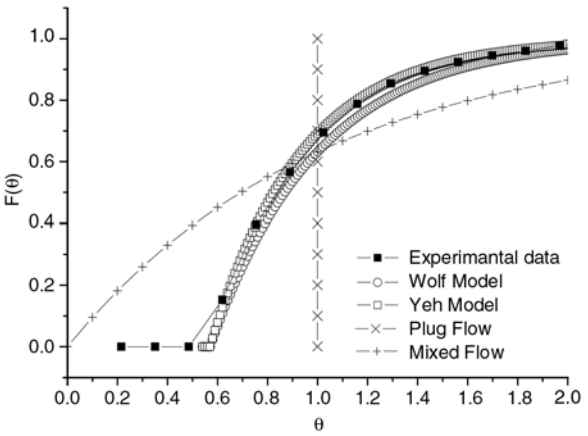

Figure 3. RTD curves as $F(\theta)$ versus θ with experimental data and different models

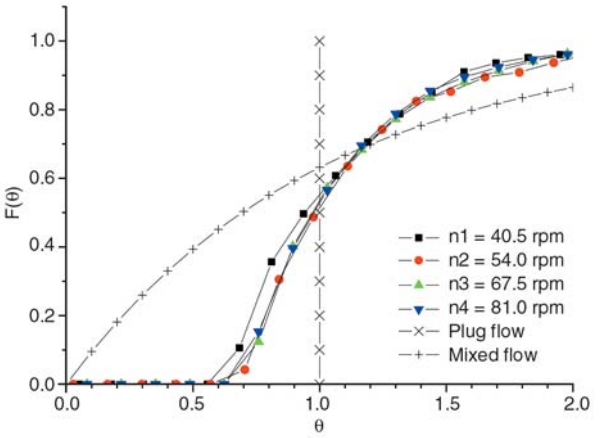

Figure 4. RTD curves as $F(\theta)$ versus θ at different screw speeds

Table 1. Parameter values derived from different models

Screw No.		Channel depth [mm]	Screw speed [rpm]	P	d
S2	Wolf model	6	81.0	0.57	–
S2	Yeh model	6	81.0	0.57	0.15

Table 2. Parameter values at different screw speeds

Screw No.	Channel depth [mm]	Screw speed [rpm]	Mixing distance [mm]	P	d
S2	6	40.5	500	0.56	0.14
S2	6	54.0	500	0.56	0.15
S2	6	67.5	500	0.56	0.15
S2	6	81.0	500	0.57	0.15

Table 3. Fiber length and dispersion at different screw speeds

Screw No.	Channel depth [mm]	Screw speed [rpm]	Fiber length [mm]	Fiber dispersion [%]
S2	6	40.5	12.78	30.58
S2	6	54.0	12.31	30.89
S2	6	67.5	11.82	31.54
S2	6	81.0	11.76	31.36

in CSTR *d* have no big variation at different screw speeds, which showed that the flow behaviors of extrusion compounding were almost the same. The results indicted that mixing capacity was slightly changed at different screw speeds.

Table 3 listed fiber length and dispersion at different screw speeds with 6mm channel depth. As the screw speed increased from 40.5 rpm to 81.0 rpm, the fiber length changed from 12.78 mm to 11.76 mm, and the dispersion increased from 30.58 to 31.36%. There were slightly change of fiber length and dispersion with increasing of screw speed. The results indicated that fiber length and dispersion would be somehow related to the value of *P* and *d*.

3.2.2. Mixing length

Figure 5 listed RTD curves were presented by $F(\theta)$ and θ for different mixing length. RTD curves showed that flow behavior of extrusion compounding was between plug flow and mixed flow, and flow behavior of longer mixing length trended towards mixed flow.

Parameters values at different mixing length derived from Yeh model were listed in Table 4. The fraction of PFR P was decreased with the extension of mixing length, and the fact showed that the trend of the flow behavior was towards mixed flow. The fraction of dead volume in CSTR *d* remained unchanged with the increment of mixing distance.

Table 5 listed fiber length and dispersion with different mixing length at 81.0 rpm screw speed and 6 mm channel depth. Fiber length was not changed

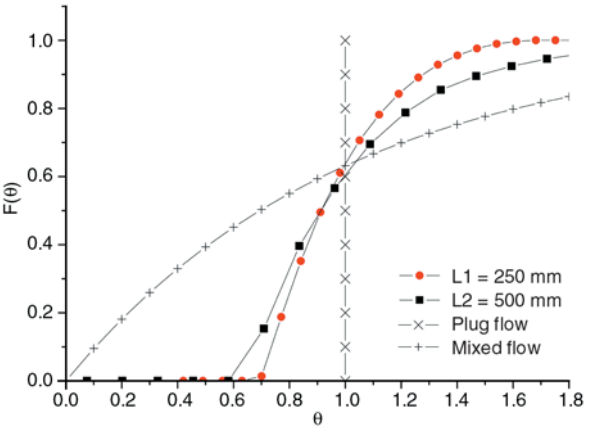

Figure 5. RTD curves as $F(\theta)$ versus θ at different mixing length

with the addition of mixing length, and fiber dispersion increased distinctly from 14.22 to 30.58%.

As to Yeh model, the extruder is considered as the combination of PFR and CSTR, extrusion compounding is regarded as the combination of plug flow and mixed flow. The results showed that fiber dispersion was increased with the increment of *P*, and the increment of *P* would impair fiber filament. Fiber length was not affected by the change of *P*, and the flow behavior of PFR, i.e. plug flow would not bring fiber to fracture severely.

3.2.3. Channel depth

3.2.3.1. Mixing length of 250 mm

RTD curves presented as $F(\theta)$ versus θ were shown in Figure 6 at 250 mm mixing length, with different channel depth. It indicted that flow behavior of extrusion compounding was between plug flow and

Table 4. Parameter values at different mixing length

Screw No.	Channel depth [mm]	Mixing length [mm]	Screw speed [rpm]	P	d
S2	6	250	81.0	0.74	0.15
S2	6	500	81.0	0.57	0.15

Table 5. Fiber length and dispersion at different mixing length

Screw No.	Channel depth [mm]	Screw speed [rpm]	Mixing length [mm]	Fiber length [mm]	Fiber dispersion [%]
S3	9	81.0	250	12.84	14.22
S3	9	81.0	500	12.78	30.58

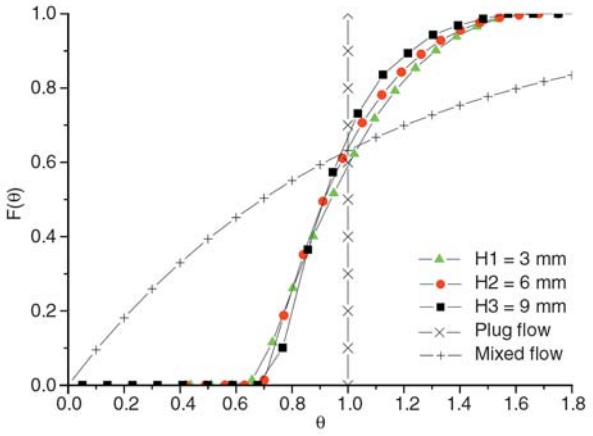

Figure 6. RTD curves as $F(\theta)$ versus θ at different channel depth for 250 mm mixing length

mixed flow, and flow behavior of bigger channel depth was close to plug flow.

Parameters values with different channel depth at 250 mm mixing length derived from Yeh model were listed in Table 6. The fraction of PFR *P* was not changed with the addition of channel depth. The fraction of dead volume in CSTR *d* was increased with the addition of channel depth, and the fact showed that flow behavior of bigger channel depth tended to plug flow.

Table 7 listed fiber length and dispersion with different channel depth and 250 mm mixing length. With the increasing of channel depth from 3 to 9 mm, fiber length increased from 10.10 to 16.85 mm and fiber dispersion reduced from 21.04 to 7.42%. The results showed that the increment of the fraction of dead volume in CSTR *d* implied the improvement of fiber length and the impairment of fiber dispersion.

As to Yeh model, the extruder is considered as the combination of PFR and CSTR, extrusion compounding is considered to be a combination of plug flow and mixed flow. The mixing in a dead volume of CSTR is limited. With same value of *P*, the addition of *d* reduced mixing capacity of extrusion compounding. The variation of fiber length and dispersion was due to the reduction of mixing capacity presented by the increasing of the fraction of dead volume in CSTR *d*.

3.2.3.2. Mixing length of 500 mm

RTD curves as $F(\theta)$ and θ with different channel depth at 500 mm mixing length were shown in Figure 7. RTD curves suggested that flow behavior of extrusion compounding was between plug flow and mixed flow. With the increasing of channel depth flow behavior approached to plug flow.

Parameter values with different channel depth at 500 mm mixing length derived from Yeh model were listed in Table 8. The fraction of PFR *P* was increased from 0.44 to 0.68 and showed that the flow behavior tended to plug flow with the increasing of channel depth. The fraction of dead volume in CSTR *d* was increasing from –0.02 to 0.20 with the increasing of channel depth, which showed that the screw of deeper channel behaved with less mixing capacity. The value of *d* (–0.02) for S1 screw

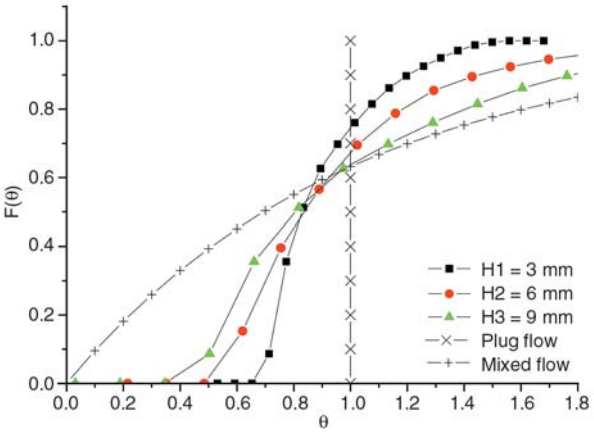

Figure 7. RTD curves as $F(\theta)$ versus θ at different channel depth for 500 mm mixing length

Table 6. Parameter values of *P* and *d* at different channel depth for 250 mm mixing length

Screw No.	Channel depth [mm]	Screw speed [rpm]	P	d
S1	3	81.0	0.76	0.04
S2	6	81.0	0.75	0.15
S3	9	81.0	0.74	0.29

Table 7. Fiber length and dispersion at different channel depth for 250 mm mixing length

Screw No.	Channel depth [mm]	Screw speed [rpm]	Fiber length [mm]	Fiber dispersion [%]
S1	3	81.0	10.10	21.04
S2	6	81.0	12.84	14.22
S3	9	81.0	16.85	7.42

Table 8. Parameter values of *P* and *d* at different channel depth for 500 mm mixing length

Screw No.	Channel depth [mm]	Screw speed [rpm]	P	d
S1	3	81.0	0.44	–0.02
S2	6	81.0	0.57	0.15
S3	9	81.0	0.68	0.21

Table 9. Fiber length and dispersion at different channel depth for 500 mm mixing length

Screw No.	Channel depth [mm]	Screw speed [rpm]	Fiber length [mm]	Fiber dispersion [%]
S1	3	81.0	7.61	65.64
S2	6	81.0	12.78	30.58
S3	9	81.0	14.74	24.44

indicated that there existed severe back mixing besides forward mixing.

Table 9 listed fiber length and dispersion with different channel depths at 500 mm mixing length. Fiber length increased from 7.61 to 12.78 mm and fiber dispersion reduced from 65.64 to 30.58% with the increasing of channel depth. Those changes of fiber degradation were due to mutual effect of the addition of both *P* and *d*.

3.3. Influence of shear force

In single screw extruder, shear rate could be expressed with constant channel depth and constant screw pitch by Equation (10) [16]:

$$\dot{\gamma} = \frac{\pi \cdot D \cdot n}{H} \tag{10}$$

where $\dot{\gamma}$ is simple shear rate, *D* is screw diameter, *n* is screw speed, and *H* is channel depth.

Shear force brought by the melt under different screw speeds was listed in Table 10. When screw speed increased from 40.5 to 81.0 rpm, shear force rose from 63.72 to 124.8 s^{-1}, glass degradation was not changed significantly based on the data listed in Table 3. Shear force brought by the melt under different channel depth was shown in Table 11. Whereas channel depth increased from 3 to 9 mm with 250 and 500 mm mixing length, shear force rose from 62.4 to 187.2 s^{-1}, glass degradation changed distinctly based on the data listed in Table 7 and Table 9. From the different changes of fiber degradation brought by the increasing of shear force, the it was concluded that shear force was not main impetus of fiber degradation.

In the process of LFT-PP extrusion, temperature range was during 200–220°C, and corresponding η was about 10^5 Pa·s, single shear rate was about 100 s^{-1} from the data in Table 10 and Table 11, see Table 8. So that the force $\dot{\gamma}\eta$ of glass fiber underwent during the process of LFT-PP extrusion would be about 10M Pa, as shown by Equation (11):

$$(\dot{\gamma}\eta) = 10^2 \cdot 10^5 = 10^7 \tag{11}$$

Salinas *et al.* posted essential condition presented by Equation (12) that fiber would fracture during the compounding [17]. As for glass fiber, $\dot{\gamma}\eta = 10^6$ MPa. The value of $\dot{\gamma}\eta$ that would bring glass fiber fracture is far more than that in the process of LFT-PP extrusion.

Table 10. Shear rate of S2 screw at different screw speeds

Screw No.	Channel depth [mm]	Screw speed [rpm]	Simple shear rate [s^{-1}]
S2	6	40.5	63.72
S2	6	54.0	83.20
S2	6	67.5	104.00
S2	6	81.0	124.80

Table 11. Shear rate under different channel depth with 500 mm mixing dept

Screw No.	Channel depth [mm]	Screw speed [rpm]	Simple shear rate [s^{-1}]
S1	3	81.5	62.4
S2	6	81.5	124.8
S3	9	81.5	187.2

$$\dot{\gamma}\eta \approx \frac{2\sigma^c(\ln 2r - 1.75)}{r^2} \quad (12)$$

As described by Wolf, during mixing glass fiber length was reduced by undergoing three interactions of fiber-equipment, fiber-fiber, and fiber-polymer [6]. Normally shear force of glass fiber applied by the melt would not bring glass fiber to be fractured because actual shear force resulted by the melt was far less than theoretical shear force derived by Salines as described above. But there are some regions such as the gap between screw edge and barrel or highly turbulent flow where fiber fracture would happen, the extent that brought glass fiber to fracture should be small. The main mechanism which brings glass fiber to facture would be fiber-equipment, and fiber-fiber interaction, and above two interactions would be improved by the enhancement of mixing capacity that could be presented by the characteristic parameters of RTD model such as *P* and *d*.

4. Conclusions

Fiber degradation expressed by fiber fracture and fiber filament could be interpreted by characteristic parameters of RTD model such as the fraction of PFR *P* and the fraction of dead volume in CSTR *d*. Fiber fracture characterized by fiber length was only increased with the increment of the fraction of dead volume in CSTR *d*. Fiber filament evaluated by fiber dispersion was impaired with the increasing of the fraction of PFR *P* and the fraction of dead volume in CSTR *d*.

P and *d* were almost unaffected by the addition of screw speed, and there was a small reduction of fiber length and mild increment of fiber dispersion at same time. *P* was decreased from 0.74 to 0.57 and *d* showed no change with the addition of mixing length.There was a distinct increase of fiber dispersion from 14.22 to 30.58% and no change of fiber length with the increment of *P*.

With the increasing of channel depth from 3 to 9 mm for 250 mm mixing length, *P* was almost same while there was significant increasing of *d* from 0.04 to 0.29. Fiber length was increased from 10.10 to 16.85 mm and fiber dispersion was decreased from 21.04 to 7.42% with the addition of *d*. With the increasing of channel depth from 3 to 9 mm for 500 mm mixing length, *P* and d showed significant change. *P* was added from 0.44 to 0.68 and *d* was increased from –0.02 to 0.21 respectively. Fiber length was increased from 7.61 to 14.74 mm and fiber dispersion was reduced from 65.64 to 24.44% with the increment of *P* and *d*.

Screw speed and channel depth would bring some change of shear force. Shear force rise from 63.72 to 124.8 s^{-1} with screw speed increasing from 40.5 to 81.0 rpm, glass degradation was not changed significantly. Whereas shear force rise from 62.4 to 187.2 s^{-1} with channel depth increasing from 3 to 9 mm, glass degradation was changed distinctly. The result was derived that shear force was not main impetus of fiber degradation.

Fiber degradation was brought by undergoing three interactions of fiber-equipment, fiber-fiber, and fiber-polymer during the extrusion. The main mechanism which brings glass fiber to facture would be fiber-equipment, and fiber-fiber interaction improved by the enhancement of mixing capacity that could be presented by the characteristic parameters of RTD model such as *P* and *d*.

From the influence of process condition and screw configuration on fiber length and dispersion, 6mm channel depth and 500 mm mixing length of free flow screw was appreciate for the optimal balance of fiber length and dispersion.

References

[1] Karian H. G.: Handbook of polypropylene and polypropylene composites. Marcel Dekker, New York (1999).

[2] Schemme M.: Long fibre reinforced thermoplastics. Kunststoffe, **93**, 106–109 (2003).

[3] Bailey R., Kraft H.: A study of fibre attrition in the processing of long fibre reinforced thermoplastics. International Polymer Processing, **2**, 94–101 (1987).

[4] Fisa B.: Mechanical degradation of glass fibers during compounding with polypropylene. Polymer Composites, **6**, 232–241 (1985).

[5] Kuroda M. M. H., Scott C. E.: Initial dispersion mechanisms of chopped glass fiber in polystyrene. Polymer Composites, **23**, 395–405 (2002).

[6] Wolf D., Holin N., White D. H.: Residence time distribution in a commercial twin-screw extruder. Polymer Engineering and Science, **26**, 640–646 (1986).

[7] Lidor G., Tadmor Z.: Theoretical analysis of residence time distribution functions and strain distribution functions in plasticating screw extruders. Polymer Engineering and Science, **16**, 450–462 (1976).

[8] Tzoganakis C., Tang Y., Vlachopoulos J., Hamielec A. E.: Measurements of residence time distribution for the peroxide degradation of polypropylene in a single-screw plasticating extruder. Journal of Applied Polymer Science, **37**, 681–693 (1989).

[9] Vainio T. P., Harlin A., Seppälä J. V.: Screw optimization of a co-rotating twin-screw extruder for a binary immiscible blend. Polymer Engineering and Science, **35**, 225–232 (1995).

[10] Ramani K., Bank D., Kraemer N.: Effect of screw design on fiber damage in extrusion compounding and composite properties. Polymer Composites, **16**, 258–266 (1995).

[11] Hornsby P. R., Singh D. P., Sothern G. R.: Determination of residence time distribution in polymer processing apparatus using tracer techniques. Polymer Testing, **5**, 77–97 (1985).

[12] Yeh A-I., Jaw Y-M.: Modeling residence time distributions for single screw extrusion process. Journal of Food Engineering, **35**, 211–232 (1998).

[13] Chen L., Pan Z., Hu G-H.: Residence time distribution in screw extruders. AIChE Journal, **39**, 1455–1464 (1993).

[14] Wolf D., Rescnick W.: Residence time distributions in real system. Industrial and Engineering Chemistry Fundamentals, **2**, 287–293 (1963).

[15] Yeh A. I., Jaw Y. M.: Modeling residence time distribution for single-screw extrusion process. Journal of Food Engineering, **35**, 211–232 (1998).

[16] Booy M. L.: The influence of non-Newtonian flow on effective viscosity and channel efficiency in screw pumps. Polymer Engineering and Science, **21**, 93–99 (1981).

[17] Salinas A., Pittman J. F. T.: Bending and breaking fibers in sheared suspensions. Polymer Engineering and Science, **21**, 23–31 (1981).

eXPRESS Polymer Letters Vol.2, No.8 (2008) 569–578
Available online at www.expresspolymlett.com
DOI: 10.3144/expresspolymlett.2008.69

Study on the combustion behavior of high impact polystyrene nanocomposites produced by different extrusion processes

G. Sanchez-Olivares[1], *A. Sanchez-Solis*[1*], *G. Camino*[2], *O. Manero*[1]

[1]Instituto de Investigaciones en Materiales, Universidad Nacional Autónoma de México. A.P. 70-360, Mexico, D. F., 04510, Mexico
[2]Politecnico di Torino – Sede di Alessandria, Viale Teresa Michel 5, 15100 Alessandria, Italy

Received 15 May 2008; accepted in revised form 9 July 2008

Abstract. The combustion behavior of a blend made of high impact polystyrene (HIPS) with sodium montmorillonite (MMT-Na^+) and triphenyl phosphite (TPP), as a halogen-free flame retardant, is analyzed in detail in this work. The blend is processed through various extrusion methods aimed to improve clay dispersion. The UL94 method in vertical position, oxygen index and cone calorimetric measurements assess HIPS blend behavior in combustion. TGA, FTIR, SEM and X-ray measurements, together with mechanical and rheological tests evaluate the thermal degradation, morphology, intercalation and degree of dispersion of particles. The use of a static-mixing die placed at the extreme of a single screw extruder improves clay platelets distribution and reduces the peak heat release rate better than employing a twin screw extrusion process. In addition, mechanical and rheological properties are affected substantially by changing the extrusion process. A correlation between clay dispersion and HIPS fire retardant properties is found, as the peak heat release rate decreases with good clay dispersion in cone calorimetric tests.

Keywords: *nanocomposites, thermal properties, rheology, HIPS, TPP*

1. Introduction

The combustion behavior of polymeric materials has been given attention due to its implications in safety for various industrial sectors. Polymer behavior under combustion is usually tested employing the oxygen index [1] and the UL94 [2] standard, and its behavior under forced combustion is commonly evaluated in cone calorimetric [3–5] tests.

To reduce the polymer combustion, various materials have been developed, such as flame retardant additives. In the past, these materials were halogen-based [6–10], but a major setback to their fire-retardant action is the production of toxic and corrosive vapors with optically dense smokes. Alternative materials sought to substitute the use of halogen-based additives include those phosphorous-based [11], and recently polymer nanocomposites [12–16]. The fact that combustion is reduced in the presence of nanoparticles with less generation of toxic compounds and enhanced barrier, thermal and mechanical properties of the polymer matrix, has motivated research on nanocomposite additives [17, 18].

Procedures to obtain polymer nanocomposites include in-situ polymerization and melt mixing extrusion among others. The latter presents advantages such as the use of commercially available equipment for large volume capacities. The melt extrusion process applied to the production of

*Corresponding author, e-mail: sancheza@servidor.unam.mx

nanocomposites requires the control of various factors, such as the shear stress, residence time, affinity of the particles to the polymer matrix and screw configuration [19–23].

In particular, high impact polystyrene (HIPS) presents high impact resistance but is a highly-flammable material. In a recent study on the HIPS rate of combustion [24], it was found that, contrary to what was expected, the addition of sodium montmorillonite (MMT-Na^+) nanoparticles increases the burning rate. However, when they are blended with triphenyl phosphite (TPP), the burning rate is decreased considerably.

The main objective of this work is the analysis of the processes aimed to reduce the flammability properties of HIPS with the use of clays and a non-halogenated flame-retardant additive, maintaining the original mechanical properties of HIPS, mainly the impact resistance. The use of different extrusion processes is intended to improve the clay and flame-retardant agent dispersion to reduce the HIPS flammability. The extrusion processes considered include intermeshing counter-rotating twin-screw, single-screw with a static-mixing die and the latter with sonication transducers placed on the die itself.

2. Experimental part

2.1. Materials

High impact polystyrene (HIPS) from Resirene, MEXICO had a density of 1.05 g/cm^3 (according to ASTM D792 norm) a melting temperature of 220°C, a glass-transition temperature of 100°C (as determined by DSC with a heating rate of 10°C/min under nitrogen atmosphere) and a melt index 2.5 g/10 min (according to ASTM D1238). Butadiene content is 15 wt% (as determined by thermogravimetry (TGA), at a heating rate of 2°C/min under nitrogen). Sodium montmorillonite clay (MMT-Na^+) was provided by Nanocor, Inc, USA (ionic exchange capacity of 135 meq/100 g). Triphenyl phosphite (TPP), an uncolored liquid with density of 1.184 g/ml at 25°C was provided by Crompton Corporation, USA, and used as received.

2.2. Equipment

A conical twin-screw intermeshing counter-rotating extruder (Haake Rheocord 90 TW-100) of 331 mm length with 31.1 mm initial diameter and 19.7 mm end diameter, and a single screw extruder with 20 mm diameter (*L*/*D* ratio of 27) with a static mixing die, which had conical compression and depression sections to produce extensional flows, were used to prepare the HIPS blends. Four 50 watts piezoelectric elements at a frequency of 25 Hz are attached to the die to produce sonication waves. Drying of samples before processing was carried out in a Pagani dehumidifier at 100°C during 8 h. A Demag-Ergotech 50-200 (*L*/*D* ratio of 20) mould-injection machine was used to produce specimens for UL94 vertical position tests and for mechanical properties. Specimens for oxygen index and cone calorimeter tests were obtained by compression molding in a Laboratory Press Gibitre Instrument. Cone calorimeter tests were carried out in a Fire Testing Technology (FTT) cone calorimeter apparatus in the horizontal position. Tensile properties were measured in an Instron 1125 machine under a constant strain-rate of 50 mm/min according to ASTM D638. Impact tests were performed following ASTM D256 Izod-notched type. XRD-analyses were performed on compression-molded 30×30×0.5 mm samples with a Thermo ARL diffractometer X-tra 48 using Cu-K_α X-ray source (λ = 1.540562 Å), step-size 0.02° at 2°·min^{-1} scanning rate in the range 2–10°. Combined thermogravimetry/Fourier transform infrared (TGA/FTIR) studies were carried out using a Perkin Elmer Pyris 1 thermogravimetric analyzer interfaced to a Perkin Elmer Spectrum GX Fourier transform infrared spectrophotometer at a scan rate of 10°C/min under inert (nitrogen) gas flow (30.0 cc/min). Rheological properties were measured on a TA Instrument AR-1000-N controlled stress rheometer with parallel plates of 25 mm diameter. Element mapping analysis were taken on a fractured surface with an Electronic Microscopic scanning LEO Model LEO1450VP (s/n CS-2278) and EDS with a Microson Oxford Inca Energy 200 (s/n CS2207).

2.3. Procedure

To evaluate the dispersion and distribution of the clay particles and TPP in the HIPS matrix, three extrusion processes were considered: intermeshing counter-rotating twin-screw, single-screw with a static-mixing die and single screw with the same die and sonication transducers attached to the die.

The purpose to use the static mixer was to produce strong extensional flows intended to improve the particle dispersion and its distribution in the polymer matrix. The blend composition is HIPS plus 5 phr clay and 5 phr TPP (HIPS-TPP/clay). The procedure to obtain the blends is described as follows:

1. Dried clay, ~1% residual water measured in a KERN MLB 50-3 powder dryer equipment, and TPP were mixed (1:1) under continuous stirring maintained at 90–105°C to render a homogeneous suspension (TPP/clay).
2. This blend and HIPS were fed using a top feeder equipment attached to the extruder under the following conditions:

a) Counter-rotating intermeshing twin-screw extrusion (CR-TS). Rotation speed was 70 rpm at processing temperature of 190°C.
b) Single-screw extrusion with the static mixing die (SS-SMD). Rotational speed was 30 rpm at 255°C.
c) Single-screw extrusion with four sonication transducers each one with 50 W power attached to the static mixing die (SS-SMD-U). The frequency generator was set at 25 Hz. Processing temperature was 255°C with rotational speed of 30 rpm.

3. Results and discussion

3.1. X-ray and element mapping

Figure 1 shows the X-ray patterns of both the TPP-clay system and the HIPS-TPP/clay blends. The diffraction peak of the TPP-clay system appears. In contrast, the HIPS-TPP/clay blends prepared following the three extrusion processes present a similar spectrum with absence of diffraction peaks in the range $2\theta = 2–10°$ revealing some intercalation that might have occurred during mixing.

According to the element mapping analysis (Figure 2), the blend processed via single-screw with the static mixing die (Figures 2a and 2b) and with sonication (Figures 2c and 2d) show dispersed agglomerates containing mainly silicon atoms. TPP distribution obtained after the single-screw extrusion (Figures 2a–2d) shows phosphorous and silicon containing particles in similar patterns. On the other hand, with the twin-screw extrusion (Figure 2e), no phosphorous particles are detected, indicating that TPP is not dispersed, but presumably

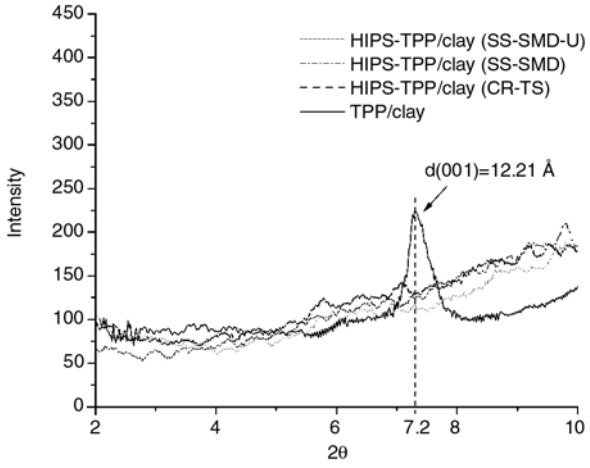

Figure 1. X-ray analysis of the HIPS-TPP/clay blend. (CR-TS), twin screw counter-rotating; (SS-SMD), single screw with the static mixing die; (SS-SMD-U) single screw with the static mixing die and sonication.

lies inside the micron-size clay agglomerates. Consequently, TPP distribution depends on the dispersion pattern of the clay particles. These results indicate that the extensional stresses generated in the static mixing die improve clay and hence TPP dispersion, as compared to the twin-screw extrusion results.

3.2. TPP/clay blend

The thermal stability and degradation processes of TPP after mixing with the clay were studied by FTIR analysis and thermogravimetry techniques. Samples include clay, TPP and the blend TPP/clay (1:1 weight). An important result is that the thermal stability of TPP is enhanced when it is mixed with the clay. Figure 3 reveals that the clay itself possesses high thermal stability since the weight loss is small. At the processing temperature, 190°C, the weight loss of the clay is 7.5% meanwhile TPP has a weight loss of 14% but weight loss of only 2.5% is measured when TPP is intercalated in the clay. This analysis demonstrates that the TPP thermal stability is enhanced when intercalated, avoiding losses by volatilization during processing. By means of TG-FTIR analysis, the gaseous species produced during TPP degradation were measured, and also those generated by the TPP/clay blend (results not shown). Spectra show absence of new compounds to those formed during pure TPP degradation, indicating that TPP intercalated in the clay and pure TPP decompose following a similar

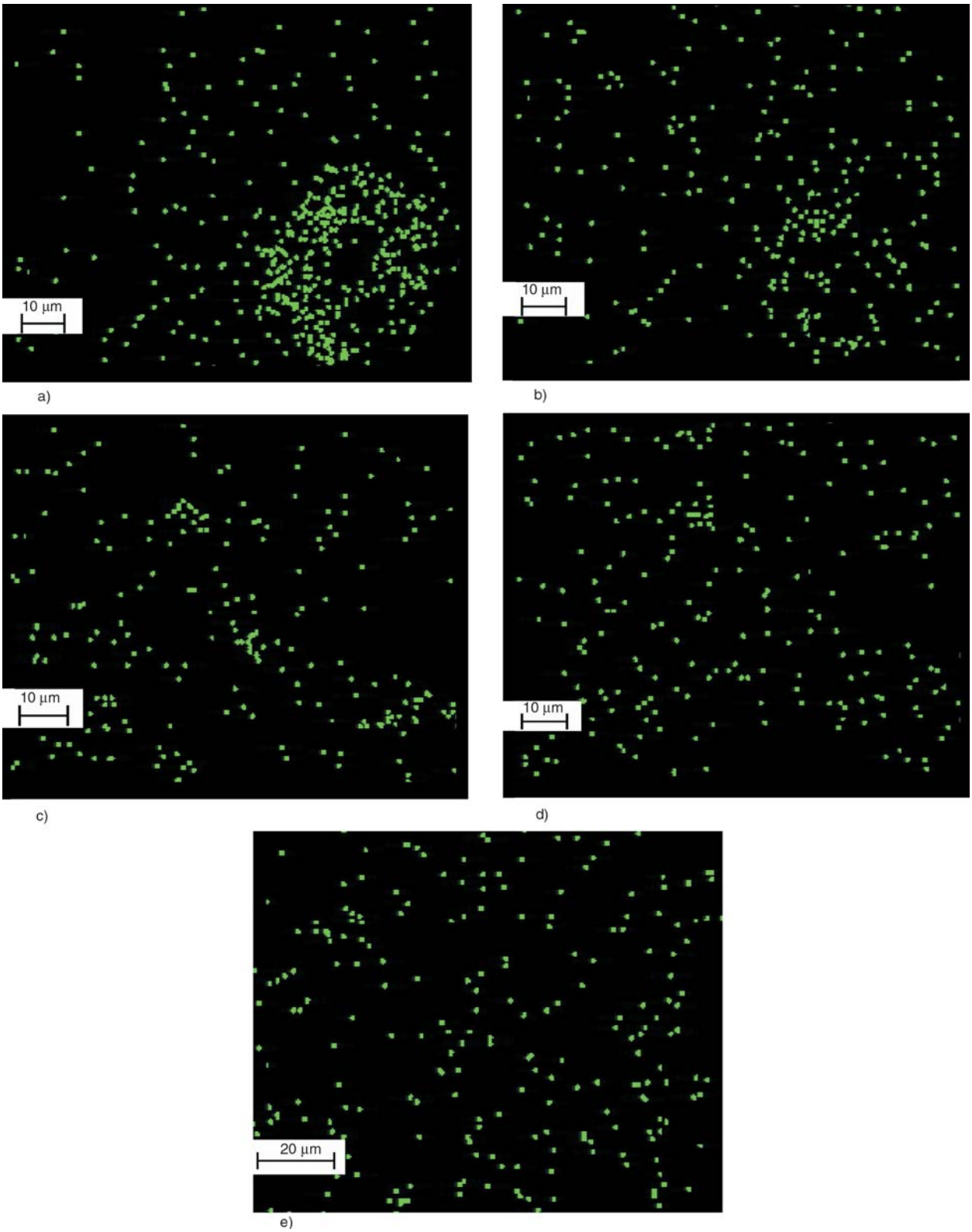

Figure 2. Element mapping for HIPS-TPP/clay blends. a) SS-SMD Silicon particles, b) SS-SMD Phosphorous particles, c) SS-SMD-U Silicon particles, 2d) SS-SMD-U Phosphorous particles, e) CR- TS Silicon particles. Magnification 1000X.

mechanism. Figure 4 presents the residues spectrum after TPP/clay decomposition, showing that only silicon compounds of the clay remain. Compounds containing Si–O and SiO_3^{2-} are characterized in the region of 1100–1000 and 470–460 cm^{-1} respectively [25, 26]. The absorptions at 3437–1631 cm^{-1} are due to KBr impurities.

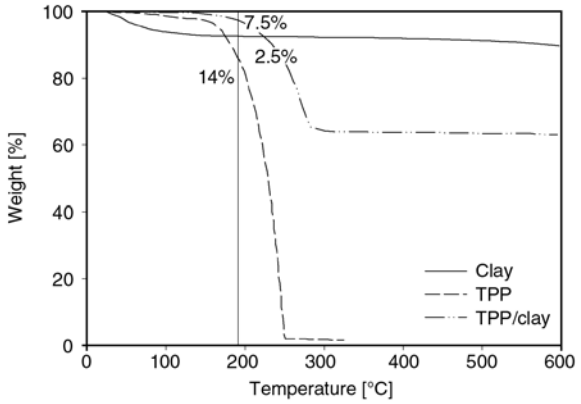

Figure 3. TGA measurements for Clay, TPP and TPP/clay. Heating rate is 10°C/min under nitrogen atmosphere. Weight loss data at 190°C.

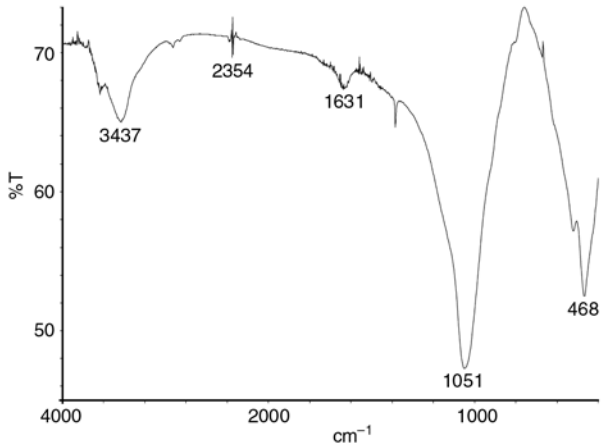

Figure 4. TGA-FTIR residues of TPP/clay (1:1)

3.3. Behavior under combustion for oxygen index and UL94-V tests

In Table 1 the oxygen index and UL94-V tests results are disclosed. Both show that the extrusion processes do not substantially influence the flammability properties of the HIPS-TPP/clay blend, since the behavior in combustion is similar to that of pure HIPS and the material continues burning after the first application of the flame (10 seconds). The flame reaches the holding clamp and the material drips and ignites the cotton, so no improvements are observed in UL94 flammability classifications despite the different extrusions processes employed. Oxygen index values are also similar, with variations up to 1.4% with respect to that of HIPS.

Table 1. Oxygen index and UL94-V results

Material	Oxygen index [%]	UL94 vertical position
HIPS	18.8	non classified
HIPS-TPP/clay (CR-TS)	19.2	non classified
HIPS-TPP/clay (SS-SMD)	19.6	non classified
HIPS- TPP/clay (SS-SMD-U)	19.4	non classified

(CR-TS), twin screw counter-rotating; (SS-SMD), single screw with the static mixing die; (SS-SMD-U), single screw with the static mixing die and sonication

3.4. Behavior under forced combustion in cone calorimetric test

Cone calorimetric data are summarized in Table 2. The parameters evaluated were time to ignition, the total heat evolved (THE), the specific extinction area (SEA), the smoke and carbon monoxide yield (CO), and the heat release rate, specially its maximum value, (pkHRR). The heat release rate is an important parameter in fire safety since it determines the fire extent and its rate of propagation. The combustion behavior shows differences depending on the extrusion process. The time to ignition for the three extrusion processes is shorter than that of HIPS, attaining the shortest time in the single-screw with the static mixing die process. This reduction in the ignition time may be attributed to the presence of nanoparticles, which induce larger mobility of the polymer melt by particle alignment with the flow to combustion zone [27, 28] and this could be promoting the initiation of the combustion in shorter times. The mobility of the polymer melt is related to the drop in viscosity. This viscosity reduction is enhanced by augmented proportion of low molecular weight polymer molecules formed either by thermal degradation of high

Table 2. Calorimetric cone data

Material	Ignition time [s]	Residues [%]	pkHRR [kW/m²]	ΔpkHRR [%]	THE [MJ/m²]	SEA [m²/kg]	CO [g/g]	ΔCO [%]
HIPS	78	0	793	–	87	929	82	–
HIPS-TPP/clay (CR-TS)	42	5	814	+3	75	773	74	–10
HIPS-TPP/clay (SS-SMD)	37	4	693	–13	89	1320	84	+3
HIPS-TPP/clay(SS-SMD-U)	49	4	724	–6	87	1339	86	+6

(CR-TS), twin screw counter-rotating; (SS-SMD), single screw with the static mixing die; (SS-SMD-U), single screw with static mixing die and sonication

molecular weight polymer molecules or by increasing concentration due to the adhesion of the high molecular weight chains to the clay platelets. The low molecular weight compounds contribute to rapidly generate volatile compounds that may be burned at the initial stage of the ignition process. In the case of the HIPS-TPP/clay system, the two blends obtained in the single-screw process present lower viscosity along the entire shear-rate range. This enhanced fluidity may be related to the lower ignition time. The char yield is similar in the three samples (4–5%) which closely corresponds to the clay concentration in the samples.

The heat-release rate results of the HIPS-TPP/clay blend are shown in Figure 5. The pkHRR is reduced by 13% with respect to that of HIPS in the single screw process with the static mixing die. In the blend obtained with the sonication system, the pkHRR is reduced by 6%. On the contrary, in the twin screw extrusion process, an increase of 3% is measured but the average specific mass loss rate decreases by 5% (not shown). The reduction in the heat release rate can then be correlated with the TPP and clay particle dispersion and distribution in the polymer. As the particle dispersion improves using the mixing die, the generation of a char layer at the surface of the melt under combustion is likely, acting as a barrier-insulator and hence retarding energy transfer and mass loss. However, this layer is weak, since it is not formed by stable residues at the decomposition temperature, and hence they are burned during the combustion process, this is depicted on Figure 5 where the shape of the curve shows two slope changes on line behavior. Regarding the effect of TPP in the combustion process, it apparently acts as a flame-retardant agent in the gas phase, since the smoke production (SEA) increases by 40% and the CO yield increases by 3 and 6% for the two single screw extrusion processes (see Table 2). It is feasible that the increasing smoke production is caused by partially-aromatized product decomposition during

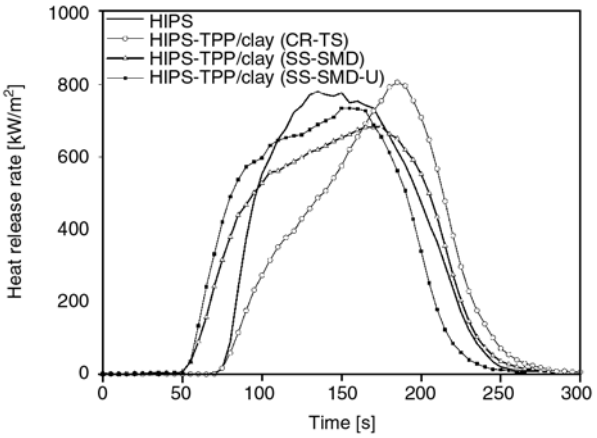

Figure 5. Heat release rate versus time for the HIPS-TPP/clay blend. (CR-TS): twin screw counter-rotating. (SS-SMD): single screw with the static mixing die. (SS-SMD-U): single screw with the static mixing die and sonication.

char formation that might volatilize before complete charring. Meanwhile, HIPS and the HIPS-clay system share the same reduced smoke production.

The particle distribution affects substantially the heat release rate. The clay particles containing intercalated TPP must have a good dispersion to obtain an effect on the heat release rate. In fact, reports [29] on fire behavior of nanocomposites have pointed out that poor dispersion at the micrometer level is unable to diminish the heat release rate substantially. The absence of nanometer-scale particles is related to an increase in the heat release rate.

3.5. Thermal stability

TGA under nitrogen atmosphere with a heating rate of 10°C/min was used to assess the thermal stability of the HIPS-TPP/clay blend produced under the three extrusion methods. The results are reported in Table 3 and in Figure 6. Table 3 shows the initial degradation temperature, corresponding to the temperature at which the weight loss of the sample attains 10% (T_{10}), the main degradation tempera-

Table 3. Degradation temperature and percentage of residues. HIPS-TPP/clay blend

Sample	T_{10} [°C]	T_{50} [°C]	Residues [%]
HIPS	382	403	1.5
HIPS-TPP/clay (CR-TS)	370	403	4.4
HIPS-TPP/clay (SS-SMD)	377	408	4.8
HIPS-TPP/clay (SS-SMD-U)	379	409	5.0

(CR-TS), twin screw counter-rotating; (SS-SMD), single screw with the static mixing die (SS-SMD-U); single screw with the static mixing die and sonication

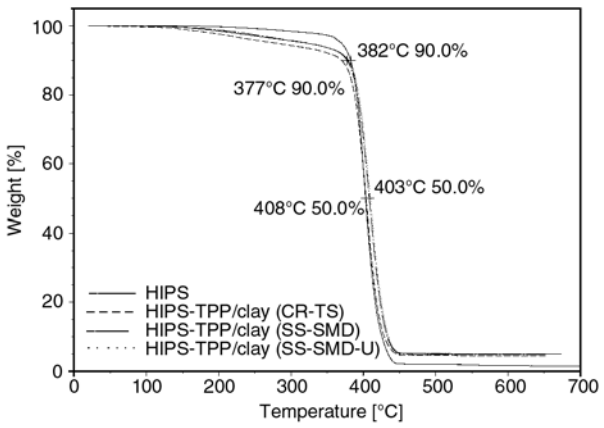

Figure 6. TGA of HIPS-TPP/clay. Same caption as in Figure 5.

ture (T_{50}) and the percentage of residues remaining at 600°C. A lower initial degradation temperature is preferred since the formation of the char layer occurs earlier, but a higher main degradation temperature is sought to achieve better thermal stability.

Figure 6 shows the mass loss versus temperature, revealing that the sample produced in the twin-screw process presents lower initial degradation temperature (–12°C) with respect to that of HIPS, but it presents the same T_{50} of HIPS. This contrasts with the samples produced in the single-screw processes, where T_{10} is lower, but T_{50} increases 5–6°C with respect to that of HIPS. Thermal stability is enhanced by a small extent with better TPP/clay particle dispersion produced in the mixing die.

3.6. Rheological properties

In the HIPS-TPP/clay blend, Figure 7 reveals the influence of the extrusion processes on the shear viscosity. The single-screw process with the mixing die affects the viscosity strongly, diminishing it with respect to that of HIPS and that of the twin-screw process throughout the range of shear rates. Plasticizing effects of TPP are discarded because the same proportion of TPP is used in all blends. Polymer degradation due to the strong flow in the die is possible. In the large shear rate range, it has been reported that with enhanced dispersion, the particles promote increasing orientation of the blend as the shear rate augments [30], and this effect induces enhanced flow of the polymer melt.

Figure 8a shows again the effect of the mixing die on the temperature dependence of the complex viscosity. Viscosity is lower in the blend produced

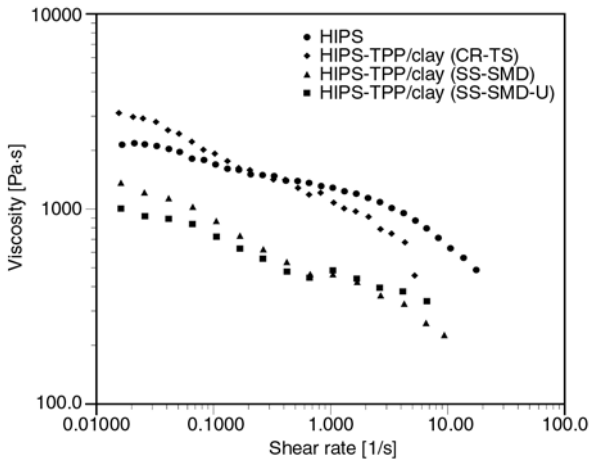

Figure 7. Shear viscosity as a function of the shear rate of the HIPS-TPP/clay blend. Same caption as in Figure 5.

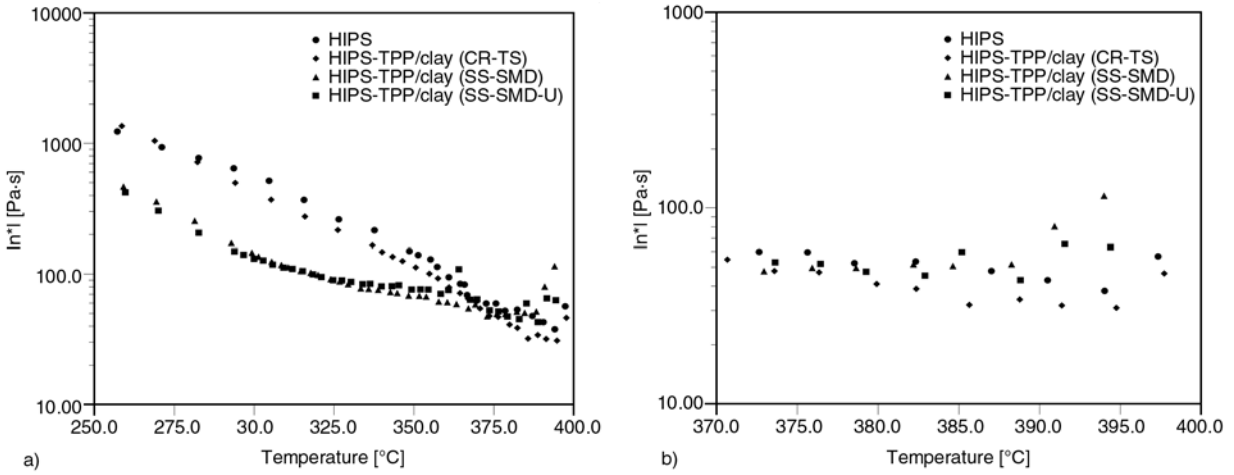

Figure 8. HIPS-TPP/clay blend. a) Complex viscosity versus temperature, b) magnification of the complex viscosity plot. Test conditions: angular frequency 1 rad/s and rate of 10°C. Same caption as in Figure 5.

using the mixing die at low temperatures, although the slope is smaller than that of the blend produced in the twin-screw process. Upon increasing temperature, the curves meet. In the high temperature range, the sudden increase of the complex viscosity at a critical temperature signals the initial stage of thermal degradation and formation of charring material [31]. This increase occurs at lower temperature for the samples obtained using the mixing die. Figure 8b shows a zoom of the last segment of the curves for HIPS and the twin-screw process. The degradation temperature in this case is 397°C, whereas with the mixing die single-screw process this is 382°C. The decrease in the initial degradation temperature by rheological measurements agrees with the results of the thermogravimetric analysis, where the initial decomposition temperature decreases with respect to that of HIPS when using the single screw device. Enhanced particle dispersion induces larger mobility and enhanced melt flow.

Figures 9a, 9b and 9c show the influence of the extrusion processes on the viscoelastic properties of the HIPS-TPP/clay blend. The storage modulus versus frequency of the blend produced in the single screw processes (with and without sonication) is similar, demonstrating a negligible effect of the sonication on the elasticity of the blends. Throughout the frequency range the elasticity of the blend produced in the single screw process is lower than the elasticity of the blend produced in the twin-screw process. At low frequencies (0.1–1.0 rad/s) the modulus of these blends decreases with respect to that of HIPS, revealing a degradation of the system as it passes through the die or an enhanced fluid-like behavior brought about by the presence of the particles. In all cases, the effect of the clay particles is apparent, as the slope of G' at small frequencies decreases from the limiting value of 2. The storage modulus in samples subjected to the twin screw process shows no difference with that of HIPS at low frequencies, and an increase in the high frequency range due to increased entanglement density or particle-polymer interactions.

The loss modulus of samples produced with the mixing die decreases with respect to that of HIPS in the low frequency range, similarly to the behavior of the shear viscosity (not shown). In the sample produced via the twin screw process, the loss modulus increases with respect to that of HIPS, again in agreement with the shear viscosity results.

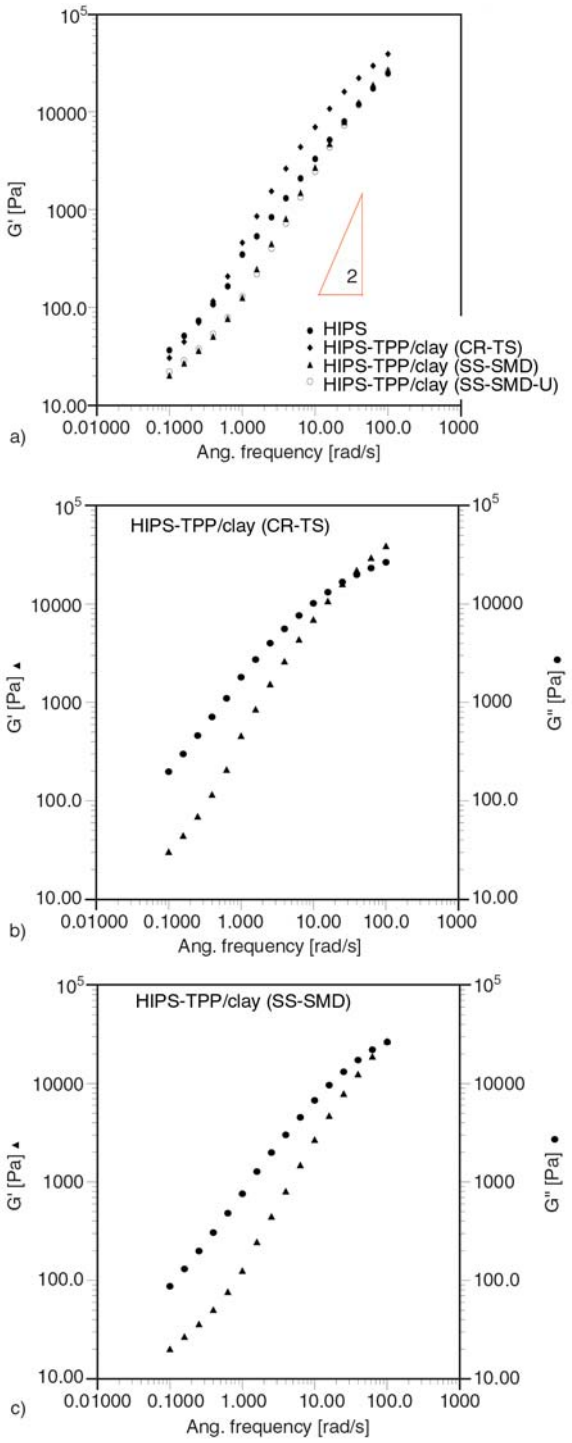

Figure 9. HIPS-TPP/clay blend. a) Storage modulus versus frequency. Same caption as in Figure 5. b) Storage and loss modulus versus frequency. Twin-screw process. c) Storage and loss modulus versus frequency. Single screw process.

In Figures 9b and 9c, G' and G'' versus frequency for samples made with the twin-screw and single-screw processes are shown, respectively. The

Table 4. Mechanical properties HIPS-TPP/clay blends

Extrusion process	Tensile strength [MPa]	Young's modulus [MPa]	Strain at break [%]	Izod impact [J/m]
HIPS	26	1017	35	161
HIPS-TPP/clay (CR-TS)	20	1017	12	166
HIPS-TPP/clay (SS-SMD)	25	930	7	105
HIPS-TPP/clay (SS-SMD-U)	27	989	8	98

(CR-TS), twin screw counter-rotating; (SS-SMD), single screw with the static mixing die (SS-SMD-U); single screw with the static mixing die and sonication

crossing point of both moduli signals the characteristic frequency of the systems, the reciprocal of which is the main relaxation time of the blend. It is apparent that the relaxation time of the blend produced in the single-screw process is smaller (0.01 s) than that of the blend that underwent the twin-screw process (0.033 s). Again, a smaller relaxation time is associated to an enhanced fluid-like behavior in shear flow when using the mixing die.

3.7. Mechanical properties

Table 4 discloses the mechanical properties under tension and impact tests of the HIPS-TPP/clay blends. Similar behavior of the blends produced using the mixing die reveals no influence of sonication. Young's modulus, strain at break and impact resistance show a decrease as compared to the HIPS values, except the tensile strength, revealing polymer degradation produced in the mixing die. This is absent in samples produced in the twin screw process, where the mixing die is not used, although the strain at break is reduced.

4. Conclusions

This study demonstrates that the HIPS-TPP/clay blend properties (flammability, combustion, thermal, rheological and mechanical) depend on the dispersion and distribution of the particles in the polymer matrix. Three extrusion processes were considered to produce different degrees of particle dispersion. When this is good (single-screw with the static mixing die process), the peak in the heat release rate diminishes in cone-calorimetric tests. The contrary occurs (twin screw process) when particle dispersion is not uniform. The sonication system with power and frequency employed has negligible effect in clay dispersion, and in the rheological and mechanical properties. A positive result is the reduction in the heat release rate due to good dispersion, but the negative effect is a reduction of the mechanical and impact properties of the blend when is processed with the mixing die

Mechanical and rheological properties are modified with respect to those of HIPS when the static mixing die is used, revealing an effect (lower viscosity) produced by degradation of the polymer as the blend passes through the die.

The TPP volatilization is reduced when it is mixed with the clay at the processing temperature, effectively increasing the efficiency of TPP as flame-retardant agent.

Results indicate an improved reduction of flammability associated to a better dispersion of the clay and TPP in HIPS due to the extrusion process used, although the price is the reduction of the mechanical properties by degradation. The paper contributes to the understanding of the balance sought between mechanical properties and reduction in flammability

Acknowledgements

We thank the financial support from the PAPIIT-UNAM project IN-103207/19 and also we acknowledge the technical support of L. Baños, M. Canseco, F. Calderas and E. Sanchez from IIM-UNAM, and F. Canta, M. Lavaselli, A. Sarra, E. Arrobio and C. Ciccarelli from Politecnico di Torino.

References

[1] ASTM D2863 (EN ISO 4589): Plastics. Thermal properties. Standard test method for measuring the minimum oxygen concentration to support candle-like combustion of plastics (oxygen index) (1999).

[2] ASTM D3801: Plastics. Thermal properties. Standard test method for measuring the comparative extinguishing characteristics of solid plastics in a vertical position, measuring (1999).

[3] ASTM E1354 (EN ISO 5660): Plastics. Standard test method for heat and visible smoke release rates for materials and products using an oxygen consumption calorimeter (1999).

[4] Schartel B., Bartholmai M., Knoll U.: Some comments on the use of cone calorimeter data. Polymer Degradation and Stability, **88**, 540–547 (2005).
[5] Schartel B., Hull T. R.: Development of fire-retarded materials-interpretation of cone calorimeter data. Fire and Materials, **31**, 327–354 (2007).
[6] Sprenkle W. E., Southern J. H.: Rubber-modified polystyrene impact as a function of flame-retardant additive solubilization. Journal of Applied Polymer Science, **26**, 2229–2238 (1981).
[7] Utevski L., Scheinker M., Georlette P., Lach S.: Flame retardancy in UL-94 V-0 and in UL-94 5VA high impact polyatyrene. Journal of Fire Sciences, **15**, 375–389 (1997).
[8] Yang C-P., Sheen B-S.: Effect of tetrabromobisphenol. A diallyl ether on the flame retardancy of high impact strength polystyrene. Journal of Applied Polymer Science, **37**, 3185–3194 (1989).
[9] Song J. H.: Typical flame retardant/additive chemicals for commercial FR-HIPS and FR-ABS resins. Journal of Vinyl and Additive Technology, **1**, 196–204 (1995).
[10] Granzow A., Savides C.: Flame retardancy of polypropylene and impact polystyrene: phosphonium bromide/ammonium polyphosphate system. Journal of Applied Polymer Science, **25**, 2195–2204 (1980).
[11] Levchik S. V., Bright D. A., Moy P., Dashevsky S.: New developments in fire retardant non-halogen aromatic phosphates. Journal of Vinyl and Additive Technology, **6**, 123–128 (2000).
[12] Gilman J. W.: Flammability and thermal stability studies of polymer layer-silicate (clay) nanocomposites. Applied Clay Science, **15**, 31–49 (1999).
[13] Gilman J. W., Jackson C. L., Morgan A. B., Harris R. Jr., Manias E., Giannelis E. P., Wuthenow M., Hilton D., Philips S. H.: Flammability properties of polymer-layered-silicate nano-composites. Polypropylene and polystyrene nanocomposites. Chemistry of Materials, **12**, 1866–1873 (2000).
[14] Porter D., Metcalfe E., Thomas M. J.: Nanocomposite fire retardants- A review. Fire and Materials, **24**, 45–52 (2000).
[15] Morgan A. B.: Flame retarded polymer layered silicate nanocomposites: A review of commercial and open literature systems. Polymers for Advanced Technology, **17**, 206–217 (2006).
[16] Morgan A. B., Wilkie C. A.: Flame retardant polymer nanocomposites. John Wiley and Sons, Hoboken (2007).
[17] Okamoto M.: Polymer/clay nanocomposites. in 'Encyclopedia of nanoscience and nanotechnology' (Ed: Nalwa H. S.) American Scientific Publishers, Stevenson Ranch, vol 8, 791–843 (2004).
[18] Gilman J. W., Kashiwagi T.: Polymer-layer silicate nanocomposites with conventional flame retardants. in 'Polymer-clay nanocomposites.' (eds.: Pinnavaia T. J., Beall G. W.) John Wiley and Sons, Baffins Lane, vol 10, 193–206 (2000).
[19] Dennis H. R., Hunter D. L., Chang D., Kim S., White J. L., Cho J. W., Paul D. R.: Effect of melt processing conditions on the extent of exfoliation in organoclay-based nanocomposites. Polymer, **42**, 9513–9522 (2001).
[20] Wang K., Liang S., Du R., Zhang Q., Fu Q.: The interplay of thermodynamics and shear on the dispersion of polymer nanocomposite. Polymer, **45**, 7953–7960 (2004).
[21] Lertwimolnum W., Vergnes B.: Influence of compatibilizer and processing conditions on the dispersion of nanoclay in a polypropylene matrix. Polymer, **46**, 3462–3471 (2005).
[22] Peltola P., Välipakka E., Vuorinen J., Syrjälä S., Hanhi K.: Effect of rotational speed of twin screw extruder on the microstructure and rheological and mechanical properties of nanoclay-reinforced polypropylene nanocomposites. Polymer Engineering and Science, **46**, 995–1000 (2006).
[23] Modesti M., Lorenzetti A., Bon D., Besco S.: Effect of processing conditions on morphology and mechanical properties of compatibilized polypropylene nanocomposites. Polymer, **46**, 10237–10245 (2005).
[24] Sanchez-Olivares G., Sanchez-Solis A., Manero O.: Effect of montmorillonite clay on the burning rate of high-impact polystyrene. International Journal of Polymeric Materials, **57**, 245–257 (2008).
[25] Lin-Vien D., Colthup N. B., Fateley W. G., Grasselli J. G.: The handbook of infrared and Raman characteristic frequencies of organic molecules. Academic Press Inc., San Diego (1991).
[26] Bebthley F. F., Smithson L. D., Rozek A. L.: Infrared spectra and characteristic frequencies. Interscience Publishers, New York (1968).
[27] Sanchez-Solis A., Garcia-Rejon A., Manero O.: Production of nanocomposites of PET-monmorillonite clay by an extrusion process. Macromolecular Symposia, **192**, 281–292 (2003).
[28] Sanchez-Solís A., Romero-Ibarra I., Estrada M. R., Calderas F., Manero O.: Mechanical and rheological studies on polyethylene terephthalate-montmorillonite nanocomposites. Polymer Engineering and Science, **44**, 1094–1102 (2004).
[29] Costache M. C., Heidecker M. J., Manias E., Camino G., Frache A., Beyer G., Gupta R. K., Wilkie C.: The influence of carbon nanotubes, organically modified montmorillonites and layered double hydroxides on the thermal degradation and fire retardancy of polyethylene, ethylene-vinyl acetate copolymer and polystyrene. Polymer, **48**, 6532–6545 (2007).
[30] Lim Y. T., Park O. O.: Rheological evidence for the microstructure of intercalated polymer/layered silicate nanocomposites. Macromolecular Rapid Communications, **21**, 231–235 (2000).
[31] Marosfői B., Matkó Sz., Anna P., Marosi Gy.: Fire retarded polymer nanocomposites. Current Applied Physics, **6**, 259–261 (2006).

eXPRESS Polymer Letters Vol.2, No.8 (2008) 579–588
Available online at www.expresspolymlett.com
DOI: 10.3144/expresspolymlett.2008.70

Synthesis of tri-block copolymers through reverse atom transfer radical polymerization of methyl methacrylate using polyurethane macroiniferter

*H. Verma, T. Kannan**

Department of Chemistry, University of Delhi, North Campus, Delhi – 110 007, India

Received 28 May 2008; accepted in revised form 9 July 2008

Abstract. Reverse atom transfer radical polymerization was successfully used for the first time to synthesis tri-block copolymers. Poly (methyl methacrylate)-*block*-polyurethane-*block*-poly (methyl methacrylate) tri-block copolymers were synthesized using tetraphenylethane-based polyurethane as a macroiniferter, copper(II) halide as a catalyst and *N*, *N*, *N′*, *N″*, *N″*-pentamethyldiethylenetriamine as a ligand. Controlled nature of the polymerization was confirmed by the linear increase of number average molecular weight with increasing conversion. Mole contents of poly (methyl methacrylate) present in the tri-block copolymers were calculated using proton nuclear magnetic resonance spectroscopy and the results were comparable with the gel permeation chromatography results. Differential scanning calorimetric results confirmed the presence of two different types of blocks in the tri-block copolymers.

Keywords: *polymer synthesis, molecular engineering, atom transfer radical polymerization, tri-block copolymers, polyurethane, poly(methyl methacrylate)*

1. Introduction

Living polymerization remains the main tool to synthesize diverse homopolymers and block copolymers of predetermined molecular weight and composition [1–3]. Controlled radical polymerization (CRP) [4–11] is another tool to improve chemoselectivity of radical polymerization. Atom transfer radical polymerization (ATRP) is the most robust CRP method to synthesize different types of polymers because of its simple polymerization conditions [12, 13]. In ATRP, simple and easily available chemicals such as organic halides and transition metal halides in their lower oxidation state are used as initiators and catalysts respectively [14, 15]. Besides their innumerable advantages, the major disadvantage of this normal ATRP is toxicity of the initiator and easy oxidation of the catalyst [16]. To overcome these difficulties Wang and Matyjaszewski proposed reverse ATRP as an alternative to normal ATRP [17]. Reverse ATRP differs from normal ATRP in its initiation process. In the case of initiators, organic halides are used in normal ATRP where as conventional radical initiators such as peroxide or azo compounds are used in reverse ATRP. Similarly, in the case of catalysts, more stable transition metal halides in their higher oxidation state are used in reverse ATRP whereas less stable transition metal halides in their lower oxidation state are used in normal ATRP [17]. Monomers such as styrene [17], methyl methacrylate [18, 19] and methyl acrylate [17, 20] were successfully polymerized through reverse ATRP using conventional initiators such as benzoyl peroxide and 2,2′-azobis(isobutyronitrile). But these initiators cannot undergo reversible deactivation and due to this, the concentration of the primary radicals is

*Corresponding author, e-mail: tharani@chemistry.du.ac.in

very high even in the presence of strong deactivators such as $CuCl_2$ especially at the early stage polymerization [17]. To overcome this, recently iniferters (*ini*tiator-trans*fer* agent-*ter*minator) were used instead of conventional initiators.

1,1,2,2-Tetraphenylethane-1,2-diol (TPED) is a well known radical initiator for the polymerization of vinyl monomers [21]. Though it contains a well known tetraphenylethane iniferter group in its structure, it doesn't act as an iniferter in controlled radical polymerization. This is due to the formation of benzophenone and monomer free radical in the initiation step. Due to this reason, the initiation mechanism of TPED is different from other tetraphenylethane derivatives [22]. 1,1,2,2-Tetraphenyl-1,2-dicyanoethane (TPDE) polymerizes vinyl monomer through controlled radical polymerization. As a result, TPDE acts as an iniferter whereas TPED neither acts as an iniferter nor follows controlled radical polymerization [22]. If the –OH groups of TPED are modified it can also act as an iniferter. Hence in the present investigation the hydroxyl groups of TPED have been modified by reacting it with NCO terminated polyurethane and the resulting polyurethane-based macroiniferter (PU-TPE) is used in reverse ATRP. Iniferter-based reverse ATRP initiating systems such as diethyl-2,3-dicyano-2,3-diphenylsuccinate/$FeCl_3$/triphenylphosphine (PPh_3) [23], 2,3-dicyano-2,3-di(*p*-tolyl)succinate/$CuCl_2$/bpy [24], 1,1,2,2-tetraphenyl-1,2-ethanediol (TPED)/$FeCl_3$/PPh_3 [16, 25], tetraethylthiuram disulphide/CuBr/bpy [26] were successfully used to polymerize vinyl and acrylate monomers. These initiating systems lower the concentration of primary radicals in the initiating step as in the case of normal ATRP. Unlike organic iniferters, macroiniferters were not used in reverse ATRP so far by any research group. Though multi-block copolymers were synthesized through macroiniferters [27–29], there was no report on the synthesis of tri-block copolymers through reverse ATRP. In fact, Matyjaszewski reported in his review that tri-block copolymers cannot be synthesized through reverse ATRP [30]. Hence in the present investigation, for the first time, synthesis of poly(methyl methacrylate)-*block*-polyurethane-*block*-poly(methyl methacrylate) (PMMA-*b*-PU-*b*-PMMA) tri-block copolymers through reverse ATRP is reported. During this study, tetraphenylethane containing polyurethane was used as a macroiniferter, cupric halide ($CuBr_2$ or $CuCl_2$) was used as a catalyst and *N*, *N*, *N*′, *N*″, *N*″-pentamethyldiethylenetriamine (PMDETA) was used as a ligand to polymerize methyl methacrylate.

2. Experimental section

2.1. Materials

Toluene diisocyanate (TDI; mixture of 80% 2,4 and 20% 2,6-TDI isomers), dibutyltin dilaurate (DBTDL), calcium hydride, and PMDETA were used as received from Aldrich, U.S.A. Acetonitrile, benzophenone, $CuBr_2$ and $CuCl_2$ were used as received from CDH, India. Analytical grade *N*, *N*-dimethylformamide (DMF; CDH, India) was distilled under reduced pressure and the middle portions were used after storing over type 4 Å molecular sieves. The inhibitor present in methyl methacrylate (MMA; CDH, India) was removed using a conventional method. It was then distilled under reduced pressure and the middle portion was stored at 0–4°C until use. Poly(tetramethyleneoxide) glycol of molecular weight 1000 (PTMG; Aldrich, USA) was purified by heating at 105°C under reduced pressure for 3 h just before use. All other chemicals were of analytical grades and were used as received.

2.2. Synthesis of TPED and tetraphenylethane-based polyurethane macroiniferter (PU-TPE)

TPED was prepared from benzophenone and 2-propanol as reported in the literature [22]. PU-TPE was synthesized based on the reported method using one mole of PTMG, two moles of TDI and one mole of TPED [27–29]. Here the completion of the reaction between NCO and OH was monitored and confirmed using Fourier-transform infrared (FT-IR) spectroscopy. The peak corresponds to NCO group was observed at 2264 cm^{-1}. This peak was gradually reduced and at the end of the reaction this peak was completely disappeared.

2.3. Reverse ATRP of MMA using PU-TPE/CuX_2/PMDETA initiating system

For the polymerization of MMA, first PU-TPE was dissolved in DMF and known quantity of

PMDETA, CuX_2 (X = Br or Cl) and MMA were added successively. The homogeneous reaction mixture was degassed by three alternate freeze-pump-thaw cycles, sealed under vacuum and placed in a thermo-stated oil bath controlled to ±0.01°C for selected time. At the end of the stipulated period of time, the reaction mixture was removed from the oil bath and the reaction was arrested by dipping in an ice-salt mixture. The resulting solution was poured into a 10-fold excess of methanol and the precipitate was filtered using sintered-glass crucible, washed with methanol and dried in vacuum. The dried samples were washed thoroughly with acetone and acetonitrile to remove traces of homo PU and homo PMMA respectively. The resulting pure block copolymers were dried in vacuum and weighed.

2.4. Characterization

Number-average ($\overline{M}_n$) and weight-average ($\overline{M}_w$) molecular weights and molecular weight distribution (MWD) were determined by gel permeation chromatography (GPC) using polymer laboratories GPC 50 integrated system equipped with differential refractometer (RI Detector) and PLgel 5 μm MIXED-C column. Tetrahydrofuran was used as an eluent at a flow rate of 1.0 ml/min and the molecular weight calibrations were done using polystyrene standards. Differential scanning calorimetry (DSC) was carried out using DSC Q200 instrument (TA instruments, USA) at a heating rate of 10°C/min under N_2 atmosphere and thermo gravimetric analysis (TGA) was carried out using DTG-60 instrument (Shimadzu, Japan) at a heating rate of 10°C/min under N_2 atmosphere. Fourier-transform nuclear magnetic resonance (FT-NMR) spectra were recorded on a Bruker DPX-300 NMR instru-

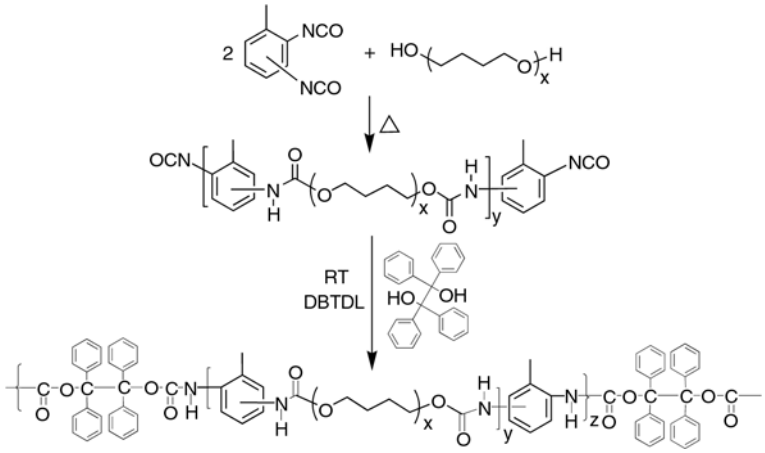

Figure 1. Synthesis of PU-TPE

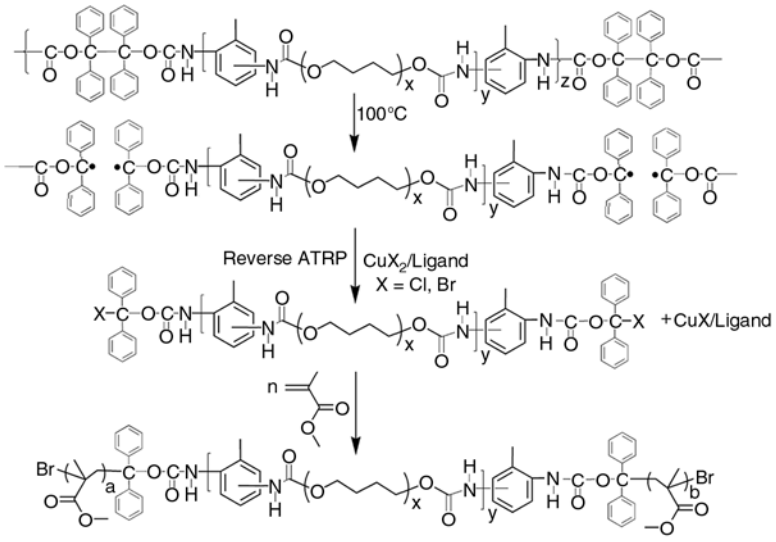

Figure 2. Synthesis of PMMA-*b*-PU-*b*-PMMA tri-block copolymers through reverse ATRP

ment using deuterated dimethyl sulfoxide as the solvent and tetramethylsilane as the internal standard. FT-IR spectra were recorded as KBr pellets on a Nicolet Impact 400 FT-IR spectrophotometer.

3. Results and discussion

Figure 1 and Figure 2 show the synthetic route for the preparation of PU-TPE macroiniferter and PMMA-*b*-PU-*b*-PMMA tri-block copolymers respectively. Here the concentration of PU-TPE was calculated using number of TPE groups present in PU-TPE using $\overline{M}_n$ obtained from GPC (cf. Tables 1 and 2). Since PU-TPE formed two radicals in the initiation step, the ratio of PU-TPE, CuX_2 (X = Br or Cl) and PMDETA was maintained at 1:2:2 respectively. To select the polymerization temperature, initially the polymerization was carried out at 80°C, but there was no polymerization and the polymerization was sluggish at 90°C. However, in the case of the polymerization at 100°C, the reaction was not sluggish and hence 100°C was chosen as a polymerization temperature for the present investigation. DMF was chosen as a solvent as it was good solvent for PU-TPE macroiniferter.

3.1. Mechanism of polymerization

To understand the mechanism of polymerization, effect of changing time on the polymerization of MMA was carried out and the results are presented in Tables 1 and 2. Here, for the calculation of conversion, weight of $[MMA]_0$ was considered and weight of $[PU\text{-}TPE]_0$ was not considered as there

Table 1. Effect of time on reverse ATRP of MMA using $CuCl_2$ at 100°C

Code No.	Time [h]	Conversion[a] [%]	Molar content of PMMA[b] [%]	$\overline{M}_n \cdot 10^{-3}$ [th][c]	GPC results			f[d]
					$\overline{M}_n \cdot 10^{-3}$	$\overline{M}_w \cdot 10^{-3}$	$\overline{M}_w/\overline{M}_n$	
PU-TPE	0	0	0	–	20.0	29.8	1.49	–
TBCP 1	1	3.5	21.2	21.4	23.5	44.8	1.91	0.90
TBCP 2	3	8.7	50.1	23.5	28.7	53.0	1.85	0.81
TBCP 3	6	15.7	62.3	26.3	31.0	55.1	1.78	0.84
TBCP 4	9	21.0	76.2	28.4	34.2	58.4	1.71	0.83
TBCP 5	12	26.3	92.1	30.5	37.4	61.7	1.65	0.81
TBCP 6	18	33.3	106.7	33.3	40.0	63.2	1.58	0.83

[a]conversion determined gravimetrically

[b]molar content of PMMA was calculated by comparing integration values of the peaks derived from PTMO and $-CH_3$ protons of PMMA blocks on ^1H NMR spectra [33]

[c] $\overline{M}_{n,th}$ = {([MMA]$_0$/2[PU-TPE]) × monomer conversion} + molecular weight of PU-TPE

[d] $f = \overline{M}_{n,th} / \overline{M}_{n,GPC}$

Polymerization conditions: $[PU\text{-}TPE]_0$ = 0.288 mmol; $[PMDETA]_0 = [CuCl_2]_0$ = 0.576 mmol; $[MMA]_0$ = 57.6 mmol; 5.94 m/l of DMF solution.

Table 2. Effect of time on reverse ATRP of MMA using $CuBr_2$ at 100°C

Code No.	Time [h]	Conversion[a] [%]	Molar content of PMMA[b] [%]	$\overline{M}_n \cdot 10^{-3}$ [th][c]	GPC results			f[d]
					$\overline{M}_n \cdot 10^{-3}$	$\overline{M}_w \cdot 10^{-3}$	$\overline{M}_w/\overline{M}_n$	
PU-TPE	0	0	0	–	20.0	29.8	1.49	–
POLY 1	1	6.0	28.9	22.4	24.6	54.1	2.20	0.91
POLY 2	3	13.8	56.2	25.5	29.8	60.8	2.04	0.85
POLY 3	6	22.5	72.1	29.0	33.2	64.7	1.95	0.87
POLY 4	9	31.2	96.2	32.5	37.9	70.5	1.86	0.85
POLY 5	12	39.9	114.1	35.9	41.0	73.3	1.79	0.87
POLY 6	18	52.9	154.7	41.1	49.0	83.8	1.71	0.84

[a]conversion determined gravimetrically

[b]molar content of PMMA was calculated by comparing integration values of the peaks derived from PTMO and $-CH_3$ protons of PMMA blocks on ^1H NMR spectra [33]

[c] $\overline{M}_{n,th}$ = {([MMA]$_0$/2[PU-TPE]) × monomer conversion} + molecular weight of PU-TPE

[d] $f = \overline{M}_{n,th} / \overline{M}_{n,GPC}$

Polymerization conditions: $[PU\text{-}TPE]_0$ = 0.288 mmol; $[PMDETA]_0 = [CuBr_2]_0$ = 0.576 mmol; $[MMA]_0$ = 57.6 mmol; 5.94 m/l of DMF solution.

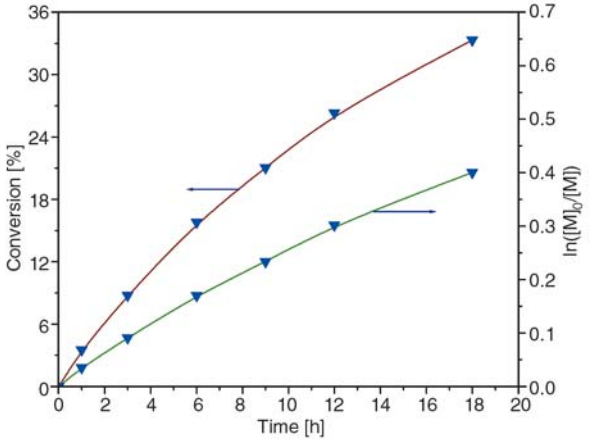

Figure 3. Time-conversion and time-ln([M]$_0$/[M]) plots for the polymerization of MMA at 100°C using PU-TPE/PMDETA/$CuCl_2$ initiating system. [PU-TPE]$_0$ = 0.288 mmol; [PMDETA]$_0$ = [$CuCl_2$]$_0$ = 0.576 mmol; [MMA]$_0$ = 57.6 mmol; 5.94 m/l of DMF solution.

was no change of weight of PU-TPE during the change of polymerization time. Figure 3 presents the kinetics of the polymerization of MMA at 100°C initiated by PU-TPE/$CuCl_2$/PMDETA initiating system. The straight line obtained in time-ln([M]$_0$/[M]) plot indicates that the concentration of growing radicals was steady throughout the polymerization. Moreover, as shown in Figure 4, $\overline{M}_{n,GPC}$, number average molecular weight from GPC, increases with increasing monomer conversion which is a clear evidence for the 'living' nature of the PU-TPE/$CuCl_2$/PMDETA initiating system. Maximum conversion obtained for the PU-TPE/$CuCl_2$/PMDETA initiating system was 33.3% and $\overline{M}_n$ of the tri-block copolymers reached upto 40 000 at 18 h (Table 1, TBCP 6). MWD of the tri-block copolymers was fairly narrow (Table 1, 1.91–1.58) and became narrower as conversion increases. Apparent initiator efficiency ($f = \overline{M}_{n,th} / \overline{M}_{n.GPC}$, where $\overline{M}_{n,th}$ denotes threotical number average molecular weight) of PU-TPE/$CuCl_2$/PMDETA initiating system was also calculated and it was found to be high for TBCP 1 (Table 1, 0.90) and low for TBCP 2 and TBCP 5 (Table 1, 0.81). Apparent initiator efficiency, f, describes the intrinsic efficiency of the initiator and its value gives us an idea about the extent of unavoidable radical-radical irreversible termination reactions are taking place in a particular polymerization reaction. The low f valve shows the presence of more irreversible termination reactions [31].

To study the effect of nature of the catalyst, $CuBr_2$ was used instead of $CuCl_2$ for the polymerization of MMA and the results are presented in Table 2. Similar to the previous system, PU-TPE/$CuBr_2$/PMDETA initiating system also shows 'livingness' during the formation of the tri-block copolymers. Figures 5 and 6 present time-vs-conversion-vs-ln([M]$_0$/[M]) and conversion-vs-$\overline{M}_n$-vs-MWD plots for TPE-PU/$CuBr_2$/PMDETA initiating system respectively. Maximum conversion obtained in this case was 52.9% and $\overline{M}_n$ was 49 000 at 18 h (Table 2, POLY 6). Initiator efficiency was also

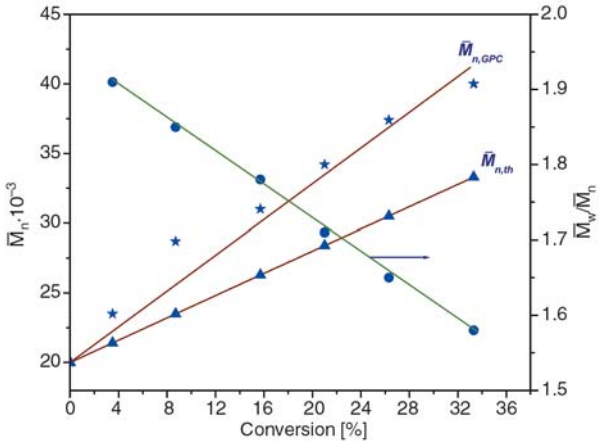

Figure 4. Conversion-$\overline{M}_n$ and conversion-$\overline{M}_w / \overline{M}_n$ plots for the polymerization of MMA at 100°C using PU-TPE/PMDETA/$CuCl_2$ initiating system. [PU-TPE]$_0$ = 0.288 mmol; [PMDETA]$_0$ = [$CuCl_2$]$_0$ = 0.576 mmol; [MMA]$_0$ = 57.6 mmol; 5.94 m/l of DMF solution.

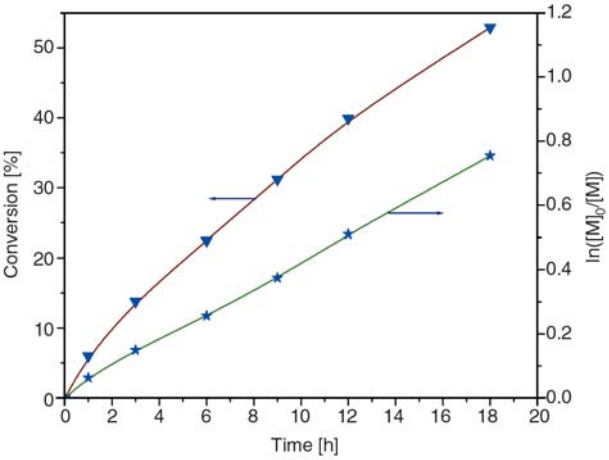

Figure 5. Time-conversion and time-ln([M]$_0$/[M]) plots for the polymerization of MMA at 100°C using PU-TPE/PMDETA/$CuBr_2$ initiating system. [PU-TPE]$_0$ = 0.288 mmol; [PMDETA]$_0$ = $CuBr_2$]$_0$ = 0.576 mmol; [MMA]$_0$ = 57.6 mmol; 5.94 m/l of DMF solution.

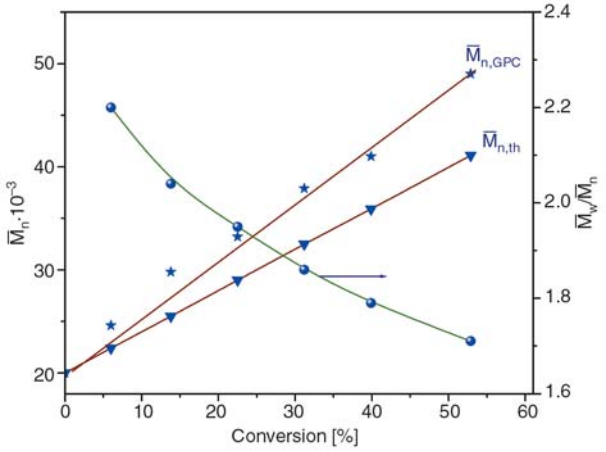

Figure 6. Conversion-$\overline{M}_n$ and conversion-$\overline{M}_w/\overline{M}_n$ plots for the polymerization of MMA at 100°C using PU-TPE/PMDETA/$CuBr_2$ initiating system. $[PU\text{-}TPE]_0$ = 0.288 mmol; $[PMDETA]_0$ = $[CuBr_2]_0$ = 0.576 mmol; $[MMA]_0$ = 57.6 mmol; 5.94 m/l of DMF solution.

calculated for this system and it was found to be high for POLY 1 (Table 2, 0.91) and low for POLY 6 (Table 2, 0.84). The conversion in $CuCl_2$ system is lower than the $CuBr_2$ system but based on the MWD values former system is more controlled than the latter system. As R–Cl bond is more stronger than R–Br bond, $CuCl_2$ acts as a good deactivator of the radical generated from PU-TPE than $CuBr_2$ and as a result conversion in $CuCl_2$ system was lower than the $CuBr_2$ system. There is a little lack of linearity especially in the time-vs-conversion-vs-ln($[M]_0/[M]$) plots (Figure 3 and Figure 5) and this might be due to the lack of inefficient deactivation by CuX_2 (X = Cl, Br)/PMDETA complex, which lead to the irreversible radical-radical termination. However 'living' nature of both the initiating systems was confirmed by linear increase of $\overline{M}_n$ with conversion plots. Moreover 'living' nature was further supported by the good aggrement between $\overline{M}_{n,th}$ and $\overline{M}_{n,GPC}$ values and MWD became narrower as the conversion increases.

3.2. Spectral studies

The formation of PU-TPE and PMMA-*b*-PU-*b*-PMMA was confirmed by ^{1}H NMR spectroscopy. Figure 7 shows ^{1}H NMR spectra of PU-TPE and PMMA-*b*-PU-*b*-PMMA tri-block copolymer obtained at 6 h (Table 2, POLY 3). The spectral data of PU-TPE and PMMA-*b*-PU-*b*-PMMA tri-

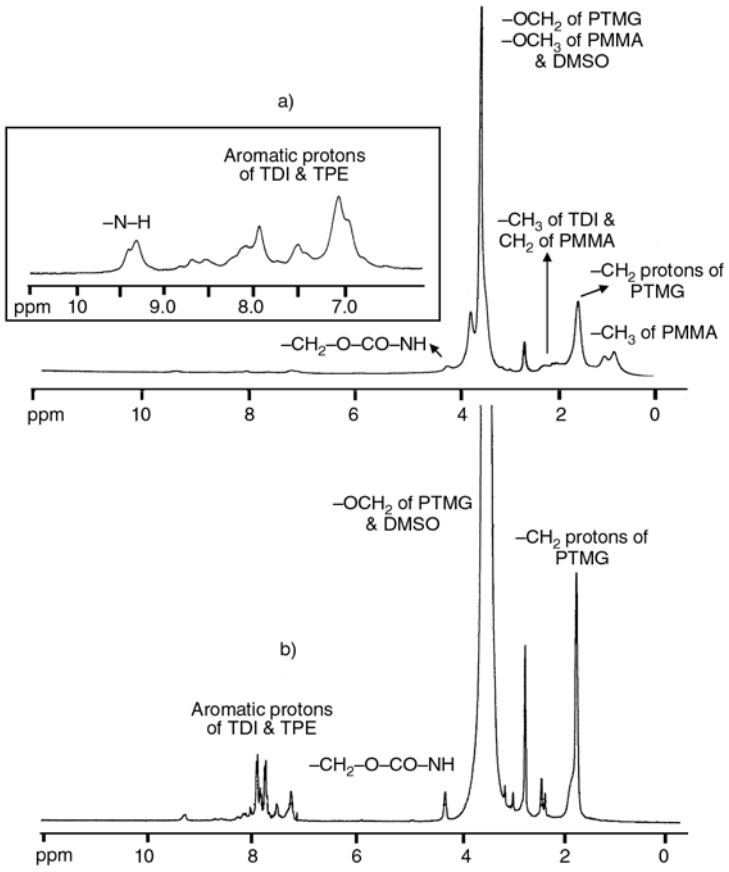

Figure 7. ^{1}H NMR spectra of (a) PMMA-*b*-PU-*b*-PMMA tri-block copolymer POLY 3 and (b) PU-TPE

Table 3. ^{1}H NMR data of PU-TPE and PMMA-*b*-PU-*b*-PMMA tri-block copolymer, POLY 3

PU-TPE		PMMA-*b*-PU-*b*-PMMA tri-block copolymer, POLY 3	
^{1}H	**Chemical shift [ppm]**	**^{1}H**	**Chemical shift [ppm]**
–N–H	8.01–9.15	–N–H	8.01–9.17
C_6H_3 of TDI, TPE	7.07–7.86	C_6H_3 of TDI, TPE	7.08–7.89
$C_6H_3(CH_3)NH$	2.05–2.12	$C_6H_3(CH_3)NH$, $–CH_2$ of PMMA	1.82–2.15
$–CH_2–$ of PTMG	1.51	$–CH_2–$ of PTMG	1.53
$–O–CH_2–$ of PTMG, DMSO	3.15	$–O–CH_2–$ of PTMG, $–OCH_3$ of PMMA, DMSO	3.1–3.7
$–CH_2–O–CO–NH$	4.07	$–CH_2–O–CO–NH$	4.11
		$–OCH_3$ of PMMA	3.5
		$–CH_3$ of PMMA	0.82–1.18
		$–CH_3$ of PMMA (*rr*)	0.82
		$–CH_3$ of PMMA (*mr*)	1.0
		$–CH_3$ of PMMA (*mm*)	1.18

block copolymer is given in Table 3. In the ^{1}H NMR spectrum of PU-TPE the aromatic protons derived from TDI and TPE were merged and appeared at 7.07–7.86 ppm. The –N–H protons of urethane groups and methyl protons derived from TDI were appeared at 8.01–9.15 ppm and 2.05–2.12 ppm respectively. The peaks correspond to $–CH_2–$ and $–OCH_2–$ protons of PTMG resonate at 1.51 and 3.15 ppm respectively. The $–OCH_2–$ of PTMG which is attached to urethane group appeared at 4.07 ppm. In the ^{1}H NMR spectrum of the tri-block copolymer obtained at 6 h (Table 2, POLY 3), the $–CH_3$ protons of PMMA resonated at 0.82, 1.00 and 1.18 ppm which correspond to syndiotactic (*rr*), atactic (*mr*) and isotactic (*mm*) PMMA respectively. The $–OCH_3$ protons of PMMA and $–OCH_2–$ protons of PTMG merged with DMSO and appeared between 3.1–3.7 ppm. The $–CH_2–$ protons of PTMG present in the tri-block copolymer appeared at 1.53 ppm. The methyl protons derived from TDI and $–CH_2–$ protons of PMMA merged and appeared at 1.82–2.15 ppm. Aromatic protons (derived from TDI and TPE groups) and –N–H protons of urethane resonated at 7.08–7.89 ppm and 8.01–9.17 ppm respectively. The $–OCH_2–$ of PTMG present in tri-block copolymer attached to urethane group was appeared at 4.11 ppm. The tacticity ratio of PMMA in POLY 3 is *rr*:*mr*:*mm* = 54:39:7 which is more or less similar to the reported tacticity ratio of PMMA prepared by ATRP [32]. The molar content of PMMA in the tri-block copolymers can easily be found out by comparing molecular weights (obtained by GPC) of PU-TPE and tri-block copolymers which are given in Tables 1 and 2. It can also be found out by comparing peak integration ratio of $–CH_2–CH_2–$ group of PTMG at 1.5 ppm and methyl protons of PMMA blocks at 0.82–1.18 ppm through ^{1}H NMR technique as described in the literature [33]. The molar content values are given in Tables 1 and 2 and these values are comparatively similar to the molar content values from GPC. Presence of peaks corresponds to PMMA blocks and PU-TPE in the ^{1}H NMR spectrum of PMMA-*b*-PU-*b*-PMMA more likely to confirm the formation of the tri-block copolymers.

The macroiniferter and the tri-block copolymer (Table 2, POLY 3) synthesized were further characterized by FT-IR spectroscopy to confirm the structure and the spectra are shown in Figure 8. Table 4 shows the FT-IR spectral data of PU-TPE and PMMA-*b*-PU-*b*-PMMA tri-block copolymers. In the FT-IR spectrum of PU-TPE, the stretching vibrations of urethane carbonyl group is at 1743 cm^{-1} and bands at 2800–3048 cm^{-1} are associated with aliphatic and aromatic –C–H asymmet-

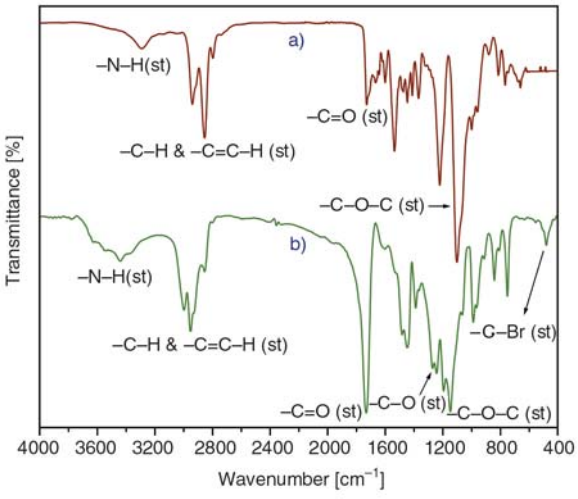

Figure 8. FT-IR spectra of (a) PU-TPE and (b) PMMA-*b*-PU-*b*-PMMA tri-block copolymer POLY 3

Table 4. FT-IR data of PU-TPE and PMMA-*b*-PU-*b*-PMMA tri-block copolymer, POLY 3

PU-TPE		PMMA-*b*-PU-*b*-PMMA tri-block copolymer, POLY 3	
Functional group	**Wave number [cm^{-1}]**	**Functional group**	**Wave number [cm^{-1}]**
–C=O (urethane)	1743 (st)	–C=O (NHCOO, PMMA)	1737 (st)
–C–H, –C=C–H (–CH in PU)	2800–3048 (st)	–C–H, –C=C–H (PU, PMMA)	2851–3010 (st)
–C–H (CH_2 in PU)	1441–1483 (bend)	–C–H (CH_2 in PU, PMMA)	1439–1485 (bend)
–C–H (CH_3 in TDI)	1371 (bend)	–C–H (CH_3 in TDI & PMMA)	1391 (bend)
–C–N (urethane)	1230 (st)	–C–N (urethane)	1233 (st)
–C–O–C–	1100 (st)	–C–O–C–	1136 (st)
–C=C– (TPE, TDI)	1603 (st)	–C=C– (TPE, TDI)	1660 (st)
–C=C– (TPE, TDI)	991 (bend)	–C=C– (TPE, TDI)	991 (bend)
–N–H (urethane)	3300 (st)	–N–H (urethane)	3353–3550 (st)
–N–H (urethane)	1533 (bend)	–N–H (urethane)	1528 (bend)
–C=C–H (CH in TPE, TDI)	749 (bend; out of plane)	–C=C–H (CH in TPE, TDI)	749 (bend; out of plane)
		–C–O– (ester group of PMMA)	1275 (st)
		–C–Br	490 (st)

ric and symmetric stretching vibrations present in –CH_2–, –CH_3 groups and phenyl rings. The peak present at 1230 cm^{-1} corresponds to –C–N– stretching vibrations present in urethane groups. The peak at 1100 cm^{-1} is due to the stretching vibrations of ether –C–O–C– groups and stretching vibrations of –C=C– appear at 1603 cm^{-1}. Stretching and bending vibrations of –N–H are observed at 3300 and 1533 cm^{-1} respectively. In the FT-IR spectrum of PMMA-*b*-PU-*b*-PMMA tri-block copolymer, the stretching vibrations of urethane groups and ester carbonyl groups of PMMA blocks with increased intensity merged and appear at 1737 cm^{-1}. The –C–H stretching vibrations of aromatic and aliphatic –CH in PU and PMMA are observed in the region 2851–3010 cm^{-1} and –N–H stretching vibrations are observed in the region 3353–3550 cm^{-1}. The stretching and bending vibrations of aromatic –C=C– (derived from TPE and TDI) are appeared at 1660 and 991 cm^{-1} respectively. Methine out-of-plane bending vibrations of –C=C–H present in aromatic rings of TDI and TPE groups appeared at 749 cm^{-1} and the stretching vibrations of ether –C–O–C– groups are observed at 1136 cm^{-1}. The stretching vibrations of –C–N– and –C–O– present in –NHCOO– groups and PMMA blocks appeared at 1233 and 1275 cm^{-1} respectively. The new peak appeared at 490 cm^{-1} is due to the stretching vibrations of terminal C–Br groups which were formed during the reverse ATRP of MMA. The –C–H bending vibrations of methylene groups present in PU and PMMA are observed from 1439 to 1485 cm^{-1}. The peak corresponding to –C–H bending vibrations of –CH_3 groups present in PU blocks (from TDI) and PMMA blocks is observed at 1391 cm^{-1}. The presence of all peaks corresponds to PU-TPE in tri-block copolymer and appearance of new peaks corresponds to PMMA blocks (cf. Table 4) further support the probable formation of PMMA-*b*-PU-*b*-PMMA tri-block copolymers.

3.3. Thermal studies

The PMMA-*b*-PU-*b*-PMMA tri-block copolymer obtained at 6 h (Table 2, POLY 3) was characterized by DSC. As shown in Figure 9, the T_g of the polyol segment present in PU-TPE and PMMA-*b*-PU-*b*-PMMA tri-block copolymers is observed at –59 and –61°C respectively. The T_g of the PMMA block is observed at 120°C which is more or less similar to the literature value of PMMA with the tacticity ratio of *rr*:*mr*:*mm* = 54:39:7 [34]. The presence of glass transition temperatures of soft and

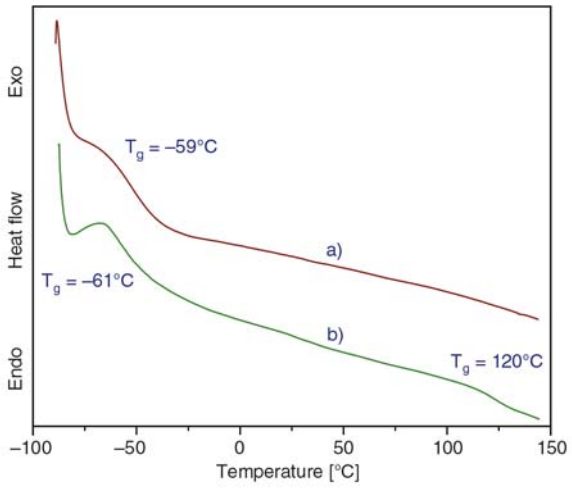

Figure 9. DSC curves of (a) PU-TPE and (b) PMMA-*b*-PU-*b*-PMMA tri-block copolymer POLY 3

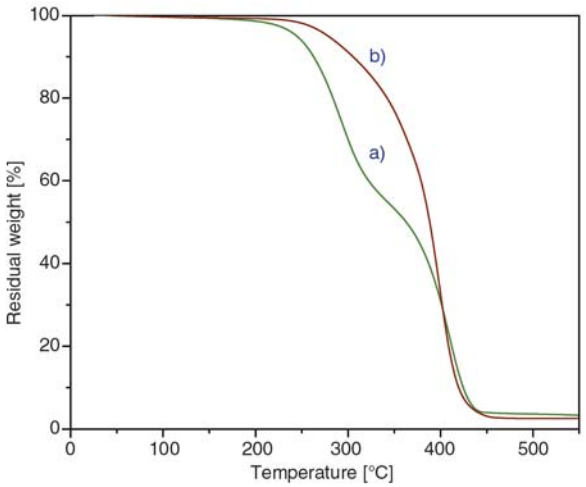

Figure 10. TGA curves of (a) PU-TPE and (b) PMMA-*b*-PU-*b*-PMMA tri-block copolymer POLY 3

hard segments may be taken as an evidence for the formation of PMMA-*b*-PU-*b*-PMMA tri-block copolymers. Thermal stability of PU-TPE and PMMA-*b*-PU-*b*-PMMA tri-block copolymer (Table 2, POLY 3) was studied and the results are presented in Figure 10. PU-TPE undergoes two-stage decomposition; one is around 284°C which is due to the decomposition of the NHCOO groups and another is around 404°C which is due to the decomposition of PTMG blocks. In the case of tri-block copolymers, the decomposition is not in stages but the overall thermal stability of PMMA-*b*-PU-*b*-PMMA tri-block copolymers is higher than the PU-TPE. Thermal degradation of standard radically prepared PMMA under nitrogen atmosphere proceeds in three steps corresponding to the cleavage of the head-to-head linkage (~165°C), the chain-end initiation from the vinylidene ends (~270°C), and random scission within the polymer chain (~360°C) [35]. Thermal degradation of the polymers synthesized using present initiating system occurred around 400°C which shows the presence random scission only. Similar type of results has been reported by Granel *et al.* for the controlled radical polymerization of methacrylic monomers in the presence of Ni(II) complex [36]. This result further indicates absence of abnormal linkages in the tri-block copolymers and confirms virtual absence of irreversible termination reactions.

4. Conclusions

For the first time polyurethane-based macroiniferter, PU-TPE has been used to synthesize PMMA-*b*-PU-*b*-PMMA tri-block copolymers through reverse ATRP. This is the first example of the synthesis of tri-block copolymers through reverse ATRP. 'Living' nature of the propagating radicals was further confirmed by time-$\ln([M]_0/[M])$ and conversion-$\overline{M}_n$ kinetic plots. $\overline{M}_{n,th}$ of the tri-block copolymers was found to be more or less similar to $\overline{M}_{n,GPC}$. The molar percentage of PMMA calculated through ^{1}H NMR is matching with GPC results. The results from spectral and thermal studies support the formation of PU-TPE and PMMA-*b*-PU-*b*-PMMA tri-block copolymers.

Acknowledgements

The authors would like to thank Council of Scientific and Industrial Research (CSIR), New Delhi, India for financial support to this project (No. 01(1964)/05/EMR-II dated 12th April, 2005).

References

[1] Szwarc M.: 'Living' polymers. Nature, **176**, 1168–1169 (1956).
[2] Szwarc M., Levy M., Milkovich R.: Polymerization initiated by electron transfer to monomer. A new method of formation of block copolymers. Journal of American Chemical Society, **78**, 2656–2657 (1956).
[3] Matyjaszewski K., Kubisa P., Penczek S.: Kinetics and mechanism of the cationic polymerization of tetrahydrofuran in solution. 1. THF-CCl_4 system. Journal Polymer Science, Part A: Polymer Chemistry, **13**, 763–784 (1975).
[4] Otsu T., Yoshida M.: Role of initiator-transfer agent-terminator (iniferter) in radical polymerizations: Polymer design by organic disulfides as iniferters. Makromolecular Chemistry Rapid Communication, **3**, 127–132 (1982).
[5] Webster O. W.: Living polymerization methods. Science, **251**, 887–893 (1991).
[6] Wayland B. B., Poszmik G., Mukerjee S. L., Fryd M.: Living radical polymerization of acrylates by organocobalt porphyrin complexes. Journal of American Chemical Society, **116**, 7943–7944 (1994).
[7] Steenbock M., Klapper M., Müllen K.: Triazolinyl radicals new additives for controlled radical polymerization. Macromolecular Chemistry and Physics, **199**, 763–769 (1998).
[8] Moad G., Rizzardo E., Thang S. H.: Radical addition fragmentation chemistry in polymer synthesis. Polymer, **49**, 1079–1131 (2008).
[9] Fischer H.: The persistent radical effect: A principle for selective radical reactions and living radical polymerizations. Chemical Reviews, **101**, 3581–3610 (2001).

[10] Chung T. C., Janvikul W., Lu H. L.: A novel 'stable' radical initiator based on the oxidation adducts of alkyl-9-BBN. Journal of American Chemical Society, **118**, 705–706 (1996).

[11] Braunecker W. A., Itami Y., Matyjaszewski K.: Osmium mediated radical polymerization. Macromolecules, **38**, 9402–9404 (2005).

[12] Matyjaszewski K., Xia J.: Atom transfer radical polymerization. Chemical Reviews, **101**, 2921–2990 (2001).

[13] Kamigaito M., Ando T., Sawamoto M.: Metal-catalyzed living radical polymerization. Chemical Reviews, **101**, 3689–3745 (2001).

[14] Zhu Y. J., Tan Y. B., Du X.: Preparation and self-assembly behavior of polystyrene-block-poly (dimethylaminoethyl methacrylate) amphiphilic block copolymer using atom transfer radical polymerization. Express Polymer Letters, **2**, 214–225 (2008).

[15] Barim G., Demirelli K., Coskun M.: Conventional and atom transfer radical copolymerization of phenoxycarbonylmethyl methacrylate-styrene and thermal behavior of their copolymers. Express Polymer Letters, **1**, 535–544 (2007).

[16] Chen X-P., Qiu K-Y.: Synthesis of well-defined polystyrene by radical polymerization using 1,1,2,2-tetraphenyl-1,2-ethanediol/$FeCl_3$/PPh_3 initiating system. Journal of Applied Polymer Science, **77**, 1607–1613 (2000).

[17] Wang J-S., Matyjaszewski K.: 'Living'/controlled radical polymerization. Transition-metal-catalyzed atom transfer radical polymerization in the presence of a conventional radical initiator. Macromolecules, **28**, 7572–7573 (1995).

[18] Xia J., Matyjaszewski K.: Homogeneous reverse atom transfer radical polymerization of styrene initiated by peroxides. Macromolecules, **32**, 5199–5202 (1999).

[19] Li P., Qiu K-Y.: Copper(II) compound catalyzed living radical polymerization of methyl methacrylate in the presence of benzoyl peroxide. Macromolecules, **35**, 8906–8908 (2002).

[20] Anand V., Agarwal S., Greiner A., Choudhary V.: Synthesis of methyl methacrylate and N-aryl itaconimide block copolymers via atom-transfer radical polymerization. Polymer International, **54**, 823–828 (2005).

[21] Braun D., Becker K. H.: Aromatische Pinakole als Polymerisationsinitiatoren. Die Angewandte Makromolekulare Chemie, **6**, 186–189 (1969).

[22] Tharanikkarasu K., Radhakrishnan G.: Tetraphenylethane iniferters. 3. 'Living' radical polymerization of methyl methacrylate using toluene-diisocyanate-based polyurethane iniferter. Journal of Macromolecular Science, Part A: Pure and Applied Chemistry, **33**, 417–437 (1996).

[23] Qin D-Q., Qin S-H., Chen X-P., Qiu K-Y.: Living/controlled radical polymerization of methyl methacrylate by reverse ATRP with DCDPS/$FeCl_3$/ PPh_3 initiating system. Polymer, **41**, 7347–7353 (2000).

[24] Qin D-Q., Qin S-H., Qiu K-Y.: A reverse ATRP process with a hexasubstituted ethane thermal iniferter diethyl 2,3-dicyano-2,3-di(*p*-tolyl)succinate (DCDTS) as the initiator. Macromolecules, **33**, 6987–6992 (2000).

[25] Chen X-P., Qiu K-Y.: Synthesis of well-defined poly(methyl methacrylate) by radical polymerization with a new initiation system TPED/$FeCl_3$/PPh_3. Macromolecules, **32**, 8711–8715 (1999).

[26] Li P., Qiu K-Y.: Reverse atom transfer radical polymerization of styrene in the presence of tetraethylthiuram disulfide. Polymer, **43**, 3019–3024 (2002).

[27] Kim B. K., Tharanikkarasu K., Lee J. S.: Polyurethane-polymethacrylic acid multi-block copolymer dispersions through polyurethane macroiniferters. Colloid and Polymer Science, **277**, 285–290 (1999).

[28] Tharanikkarasu K., Radhakrishnan G.: Tetraphenylethane iniferters-9. Diphenylmethane diisocyanate-based polyurethane-polystyrene block copolymers through 'living' radical mechanism. European Polymer Journal, **33**, 1779–1786 (1997).

[29] Tharanikkarasu K., Radhakrishnan G.: Tetraphenylethane iniferters: Polyurethane-polystyrene multiblock copolymers through 'living' radical polymerization. Journal of Applied Polymer Science, **66**, 1551–1560 (1997).

[30] Braunecker W. A., Matyjaszewski K.: Recent mechanistic developments in atom transfer radical polymerization. Journal of Molecular Catalysis, A: Chemical, **254**, 155–164 (2006).

[31] Destarac M., Matyjaszewski K., Boutevin B.: Polychloroalkane initiators in copper-catalyzed atom transfer radical polymerization of (meth)acrylates. Macromolecular Chemistry and Physics, **201**, 265–272 (2000).

[32] Wang J-S., Matyjaszewski K.: Controlled/'living' radical polymerization. Halogen atom transfer radical polymerization promoted by a Cu(I)/Cu(II) redox process. Macromolecules, 28, 7901–7910 (1995).

[33] Higaki Y., Otsuka H., Takahara A.: Facile synthesis of multiblock copolymers composed of poly(tetramethylene oxide) and polystyrene using living free-radical polymerization macroinitiator. Polymer, **47**, 3784–3791 (2006).

[34] Brandrup J., Immergut E. H., Grulke E. A.: Polymer handbook. John Wiley and Sons, Toronto (1989).

[35] Hatada K., Kitayama T., Fujimoto N., Nishiura T.: Stability and degradation of polymethacrylates with controlled structure. Journal of Macromolecular Science, Part A: Pure and Applied Chemistry, **30**, 645–667 (1993).

[36] Granel C., Dubois P., Jérôme R., Teyssié P.: Controlled radical polymerization of methacrylic monomers in the presence of a bis(ortho-chelated) arylnickel(II) complex and different activated alkyl halides. Macromolecules, **29**, 8576–8582 (1996).

eXPRESS Polymer Letters Vol.2, No.8 (2008) 589–601
Available online at www.expresspolymlett.com
DOI: 10.3144/expresspolymlett.2008.71

Azo polymers with electronical push and pull structures prepared via RAFT polymerization and its photoinduced birefringence behavior

H. Z. Cao[1], W. Zhang[1], J. Zhu[1], X. R. Chen[2], Z. P. Cheng[1], J. H. Wu[2], X. L. Zhu[1]*

[1]Key Laboratory of Organic Synthesis of Jiangsu Province, School of Chemistry and Chemical Engineering, Soochow (Suzhou) University, 215006 Suzhou, China
[2]Institute of Information Optical Engineering, Soochow (Suzhou) University, 215006 Suzhou, China

Received 12 May 2008; accepted in revised form 9 July 2008

Abstract. Two methacrylate monomers containing azo and electronical push and pull structure, e.g. 2-Methyl-acrylic-acid-2-{[4-(4-cyano-phenylazo)-3-methyl-phenyl]-ethyl-amino-ethyl ester (MACP) with cyano substituted and 2-Methyl-acrylic-acid-2-{ethyl-[4-(4-methoxy-phenylazo)-3-methyl-phenyl]-amino}-ethyl ester (MAMP) with methoxy substituted, were synthesized and polymerized using 2-cyanoprop-2-yl dithiobenzoate (CPDB) as chain transfer agent and 2,2'-azobisisobutyronitrile (AIBN) as initiator. The results showed that the polymerization displayed characteristics of 'living'/controlled free radical polymerization. Thus, the obtained polymers, polyMACP (pMACP) and polyMAMP (pMAMP), had controlled molecular weights and narrow molecular weights distribution. The chain extension experiments of pMACP and pMAMP using styrene as the second monomer were successfully carried out. The photo-induced *trans-cis-trans* isomerization kinetic of pMACP and pMAMP in chloroform solution were described. Marked differences in rate for the *trans-cis* and *cis-trans* isomerization of pMACP and pMAMP were observed in chloroform solution due to the different electronic effects in these two polymers. Photoinduced birefringence and surface relief grating (SRG) of the pMACP and pMAMP were investigated in thin film state.

Keywords: *polymer synthesis, azopolymers, photo-induced birefringence, surface relief grating (SRG), reversible addition-fragmentation chain transfer polymerization (RAFT)*

1. Introduction

Azobenzene-containing polymers received more and more attentions in this decade for their potential applications in many fields, such as optical data storage [1, 2], nonlinear optical materials [3, 4], holographic memories [5, 6], chiroptical switches [7, 8] and surface relief gratings (SRG) [9, 10]. The photo-responsive properties of the azopolymers are based on the *trans-to-cis* and *cis-to-trans* photo isomerizations of azo chromophores, which leads to considerable changes in their molecular shape and dipole moments [11, 12]. It is generally accepted that in the surface relief gratings (SRG) forming process, the large-scale mass transport of the azopolymer chains is caused by the photoinduced *trans-cis-trans* isomerization cycles of azo chromophores, which results in the surface modulation in a reversible way. A considerable amount of literature has been devoted to the dynamic processes of the SRGs formation and several models have been proposed to describe the mechanism of the large photoinduced mass transport [13–16].

On the other hand, the optically induced birefringence can be produced on azobenzene-containing

*Corresponding author, e-mail: xlzhu@suda.edu.cn

polymers by linearly polarized (LP) photoexcitation of the azobenzene group, which undergoes *trans-cis-trans* isomerization [17, 18] , giving rise, after repeated photoexcitation and isomerization cycles, to a net excess of azobenzene moieties oriented with their transition dipole moments perpendicularly to the direction of the pump electric field. The anisotropic distribution of chromophores provides birefringence and linear dichroism of the film can be erased by irradiation with depolarized or circularly polarized (CP) light, thus reproducing the original isotropy in the material. According to Rabek's report [19], azo compounds can be divided into three classes: azobenzene type, aminoazobenzene type and pseudo-stilbene type. Azobenzene containing compounds with electronical push and pull structures (pseudo-stilbene type) and aminoazobenzene type molecules can isomerize from *cis* configuration back to *trans* configuration very quickly at room temperature. However, the thermal *cis-trans* isomerization in azobenzene-type molecules is relatively slow, and it is even possible to isolate the *cis* isomer [20].

Typically, the azobenzene containing polymers can be obtained through two ways: incorporating azobenzene chromophores into the backbones directly during the polymerization process [21–23], and postpolymerization modification technique [24–27]. Generally, conventional free radical polymerization (uncontrolled radical polymerization) can be used for the facile synthesis of polymers with side-chain containing azobenzene chromophores with high functionality. However, the structures of polymers obtained by this way can not be tailored and are usually ill-defined. Anionic polymerization has been used to synthesize well-defined end-functional polymers with predetermined molecular weights and narrow molecular weight distributions. However, the reaction conditions are very stringent and the range of polymerisable monomers is quite limited. The 'living'/ controlled free radical polymerization (LFRP) [28–39], developed rapidly during the past decade, was a frequently used technology in the preparation of well-defined polymers. Among the LFRP techniques, the reversible addition-fragmentation chain transfer (RAFT) polymerization is considered as one of the most versatile method with wide range of polymerisable monomer and undemanding polymerization conditions.

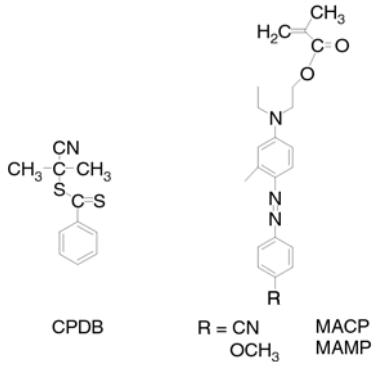

Figure 1. Chemical structures of 2-cyanoprop-2-yl dithiobenzoate (CPDB), 2-methyl-acrylic-acid-2-{[4-(4-cyano-phenylazo)-3-methyl-phenyl]-ethyl-amino}-ethyl ester (MACP) and 2-methyl-acrylic-acid-2-{ethyl-[4-(4-methoxy-phenylazo)-3-methyl-phenyl]-amino}-ethyl ester (MAMP)

Herein, we report a detailed study of RAFT polymerization of two methacrylate monomers, bearing azobenzene moieties with different push and pull substituted groups at 4-position in the benzene rings, e.g. MACP with cyano group substituted while MAMP with methoxy substituted (as showed in Figure 1). To study the effect of the polarity of substitutional groups, cyano and methoxy on the photo-responsive behaviors, the photo-induced *trans-cis-trans* isomerization kinetic of the polymers from RAFT polymerization were described. Furthermore, photoinduced birefringence and SRGs of these polymers were investigated in thin film state.

2. Experimental section

2.1. Materials

Methacryloyl chloride was purchased from Haimen Best Fine Chemical Industry Co. Ltd. (Jiangsu, China) and used after distillation. Styrene (St, 99%, Shanghai Chemical Reagent Co. Ltd. China) was washed with a 5% sodium hydroxide aqueous solution and then with deionized water until neutralization. After being dried with anhydrous magnesium sulfate overnight, it was distillated over CaH_2 under vacuum and stored at –18°C. 2,2'-azobisisobutyronitrile (AIBN, 97%, Shanghai Chemical Reagent Co. Ltd. China) was recrystallized from ethanol twice, dried under vacuum at room temperature, and stored at –18°C. Anisole and chloroform (analytical grade) were purchased from Shanghai Chemical Reagent Co. Ltd (China) and used after

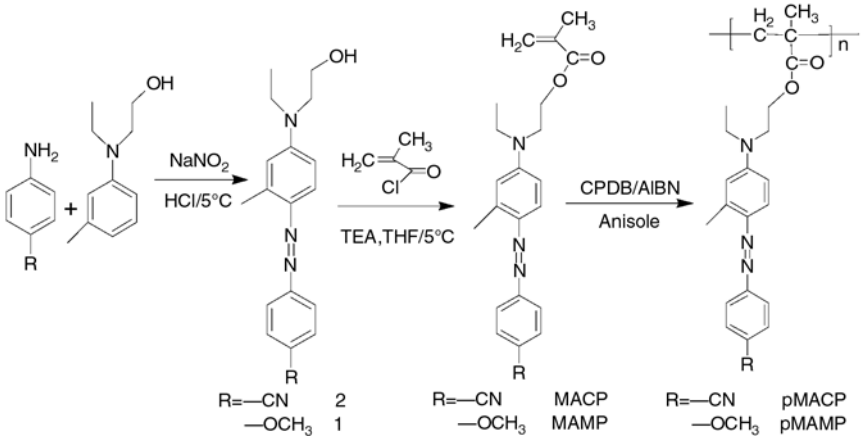

Figure 2. The synthetic routes of MACP, MAMP, pMACP and pMAMP

distillation. N-Ethyl-N-2-hydroxyethylm-toluidine (TCI, Tokyo Kasei Kogyo Co. Ltd. Japan, 99%) and 4-aminobenzonitrile (Alfa, A Johnson company, USA, 98%) were used as received. 2-Cyanoprop-2-yl dithiobenzoate (CPDB, as in Figure 2) was synthesized according to the literature [40]. The synthetic routes of MACP and MAMP are presented in Figure 2. Other materials were purchased from Shanghai Chemical Reagent Co. Ltd. China and purified according to the standard method.

2.2. Synthesis of MAMP and MACP

2-{Ethyl-[4-(4-methoxy-phenylazo)-3-methyl-phenyl]-amino}-ethanol (1)

4-Methoxyanhiline (4.96 g, 40 mmol) was dissolved in an aqueous solution of sodium nitrite (3.38 g in 40 ml of deionized water). The obtained solution was cooled to 0–5°C and then hydrochloric acid (16 ml) in 100 ml deionized water was added slowly with stirring. After stirring for further 30 min, carbamide (0.48 g, 8 mmol) was added to demolish the residual sodium nitrite with tracking by starch-iodide paper. Then the diazonium salt solution was obtained. A solution of N-ethyl-N-2-hydroxyethylm-toluidine (8.78 g, 48 mmol), glacial acetic (15 ml) and deionized water (30 ml) prepared beforehand was slowly added to the diazonium salt solution at 0–5°C. The mixture was vigorously stirred for 30 min in ice bath and aqueous sodium hydroxide solution was added to adjust the pH to 5–7. The solution was heated to 40–50°C gradually and kept for 15 min, and then it was cooled for 2 h. The solid was filtered and dried under vacuum at room temperature. After recrystallized from ethanol-water mixture (3:2, v:v), the compound 1 was obtained as a yellow crystalline solid (7.5 g, 68%). ^{1}H NMR ($CDCl_3$): 7.80–7.88(d, 2H), 7.66–7.73(d, 1H), 6.89–7.03(d, 2H), 6.62(s, 2H), 3.80–3.90(t, 5H), 3.46–3.60(m, 4H), 2.69(m, 3H), 1.58(s, 1H), 1.14–1.28(t, 3H). Anal. Calcd. for $C_{18}H_{23}N_3O_2$: C 68.98, H 7.40, N 13.41; found: C 68.65, H 7.41, N 12.95.

2-Methyl-acrylic-acid-2-{ethyl-[4-(4-methoxy-phenylazo)-3-methyl-phenyl]-amino}-ethyl ester (MAMP)

Compound 1 (6.2 g, 20 mmol), dry THF (50 ml) and triethylamine (2.8 ml) was added to a round-bottom flask, then the mixture was cooled with ice bath. Methacryloyl chloride (1.9 ml, 22 mmol) diluted in dry THF (10 ml) was added dropwise to the cooled compound 1 solution. The resultant mixture was vigorously stirred for 1 h at 0–5°C and then at room temperature for further 6 h. The solution was filtered and the solvent was removed by rotary evaporation. The crude product was dissolved in dichloromethane and washed with deionized water three times, then dried with anhydrous magnesium sulfate overnight. Finally, the obtained crude product was purified by column chromatography (silica gel H) with petroleum ether/ethyl acetate = 4:1 (v:v) as eluent to give a yellow crystalline solid MAMP (4.3 g, 56.4%). ^{1}H NMR ($CDCl_3$): 7.81–7.93(d, 2H), 7.72–7.75(s, 1H), 6.97–7.01(d, 2H), 6.62(s, 2H), 6.13(s, 1H), 5.6(s, 1H), 4.32–4.39(t, 2H), 3.89(s, 3H), 3.66–3.72(t, 2H), 3.45–3.57(m, 2H), 2.7(s, 3H), 1.96(s, 3H),

1.22–1.27(t, 3H). Anal. Calcd. for $C_{22}H_{27}N_3O_3$: C 68.9, H 7.15, N 10.73; found: C 69.27, H 7.13, N 11.02.

4-{4-[Ethyl-(2-hydroxy-ethyl)-amino]-2-methyl-phenylazo}-benzonitrile (2)

The compound 2 was synthesized using a similar procedure as compound 1 as a red crystalline solid (9.29 g, 75.4%). ^{1}H NMR ($CDCl_3$) 7.84–7.94(d, 2H), 7.75–7.84(s, 1H), 7.65–7.78(d, 2H), 6.62(s, 2H), 3.88(s, 2H), 3.47–3.65(m, 4H), 2.68(s, 3H), 1.56(s, 1H), 1.18–1.30(t, 3H). Anal. Calcd. for $C_{18}H_{20}N_{4O}$: C 69.93, H 6.69, N 18.61; found: C 70.11, H 6.54, N 18.17.

2-Methyl-acrylic-acid-2-{[4-(4-cyano-phenylazo)-3-methyl-phenyl]-ethyl-amino}-ethyl ester (MACP)

MACP was synthesized using a similar procedure as MAMP. It was purified by column chromatography (silica gel H) with petroleum ether/ethyl acetate = 10:1 (v:v) as eluent, producing a red crystalline solid MACP (4.8 g, 63%). ^{1}H NMR ($CDCl_3$): 7.86–7.91(d, 2H), 7.78–7.82(d, 1H), 7.71–7.76(d, 2H), 6.62–6.64(t, 2H), 6.11(s, 1H), 5.59(s, 1H), 4.33–4.39(t, 2H), 3.66–3.78(t, 2H), 3.44–3.59(m, 2H), 2.69(s, 3H), 1.92–1.98(d, 3H), 1.22–1.29(t, 3H). Anal. Calcd. for $C_{22}H_{24}N_4O_2$: C 69.90, H 6.54, N 14.77; found: C 70.19, H 6.43, N 14.88.

2.3. RAFT Polymerization of MACP and MAMP

The following procedure was typical as in Figure 2: a master batch of AIBN (4.1 mg, 0.025 mmol) and CPDB (33.2 mg, 0.15 mmol) was dissolved in anisole (10 ml) and aliquot of 1 ml was placed in a 5 ml ampoule with MAMP (381.5 mg, 1.00 mmol) added in advance. The contents were purged with argon for approximately 20 min to eliminate the oxygen. Then, the ampoules were flame-sealed and placed in an oil bath held by a thermostat at 80°C to polymerize. After predetermined time, each ampoule was quenched in ice water and opened. The reaction mixture was diluted with 2 ml of THF and precipitated into 200 ml of methanol. The polymers were dried under vacuum at room temperature to constant weight. The conversion was determined by gravimetry. The RAFT polymerization of MACP was used a similar procedure as that of MAMP. The polymers from MACP and MAMP are referred as pMACP and pMAMP, respectively.

2.4. Chain extension of pMACP and pMAMP with styrene (St) as the second monomer

The RAFT polymerization of St was carried out with the similar procedure as mentioned above, except that CPDB was replaced by pMACP and pMAMP obtained from the polymerization of MACP and MAMP.

2.5. Preparation of the polymer film

pMACP or pMAMP was dissolved in chloroform with concentration of 0.1 g·ml^{-1}. The obtained azo-polymer solutions were filtered by mesh filter with 0.2 μm of pore size. Thin films were prepared on glass substrates by spin coating at 2500 rpm. The thickness of the film was controlled to be in the interval of 100–200 nm. After dried in vacuum oven for 24 h, the amorphous film with good optical quality was obtained and stored in desiccator for further study.

2.6. Instruments for characterization

^{1}H NMR spectra were obtained on an Inova 400 MHz spectrometer using $CDCl_3$ as a solvent. Gel permeation chromatography (GPC) analysis was carried out on waters 1515 chromatography equipped with a refractive index detector with THF as an eluent and poly(methyl methacrylate) (PMMA) as standard sample. The UV-vis absorption spectra of the polymers in chloroform solutions were determined on a Shimadzu-RF540 spectrophotometer. Film thickness was measured on Ambios-step XP-2 profiler. The birefringence was

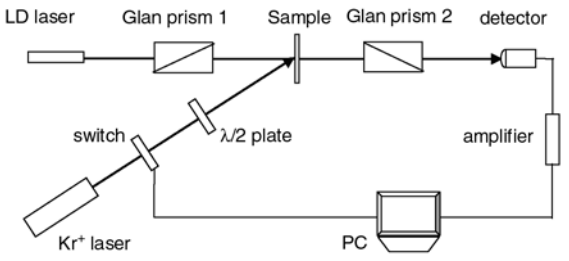

Figure 3. Setup for producing and detecting the birefringence effect of the sample

measured with a pump Kr^+ laser beam (413.1 nm, 5 mW/cm^2) polarized at 45° with respect to the probe beam polarization. The experimental setup is shown in Figure 3. The sample was placed between two crossed polarizers. The transmitted probe beam (650 nm diode laser) was detected by a photoelectric cell and connected to a computer through an amplifier. The photoinduced birefringence values of the films were obtained from transmitted intensity measurements. The other experimental setup for surface relief gratings (SRGs) fabrication was similar to that reported in the literature [41]. A linearly polarized Kr^+ laser beam (413.1 nm, 30 mW/cm^2) was used as the light source. SRGs were optically inscribed on the polymer films with p-polarized interfering laser beams. The surface morphology of the gratings was determined by atomic force microscopy (AFM) (NT-MDT SOLVER P47-PRO). The diffraction efficiency of the gratings was monitored by measuring the first-order diffracted beam intensity of an unpolarized low power diode laser beam (650 nm) in transmission mode.

3. Results and discussion

3.1. RAFT polymerizations of MAMP and MACP

RAFT polymerization technique was considered as the one of the most versatile methods to synthesize polymers with well-defined structure under the moderate conditions. The RAFT polymerization of azo monomer has been demonstrated in the literatures [37, 38]. The MACP and MAMP with electronic push and pull structures were designed in order to improve the thermal *cis-trans* isomerization rate [19, 20]. The RAFT polymerizations of MACP at 70°C and MAMP at 80°C in anisole solution were carried out with CPDB as a RAFT agent and AIBN as an initiator ($[MACP]_0$:$[AIBN]_0$:$[CPDB]_0$ = 200:1:3, $[MAMP]_0$:$[AIBN]_0$:$[CPDB]_0$ = 200:0.5:3). It was found that at 70°C, the RAFT polymerization of MAMP was very slow. After 336 hours of polymerization, only 20.1% of conversion was obtained ($[MAMP]_0$:$[AIBN]_0$:$[CPDB]_0$ = 200:1:3). The RAFT temperature of MAMP was thus set at 80°C. The polymerization results were summarized in Figure 4 and Figure 5. As shown in Figure 4, the corresponding plot of $\ln([M]_0/[M])$ versus the polymerization time was linear, which indicated that the propagating radical concentrations were almost constant during the processes of the polymerization. The polymerization rate of MACP was much faster than that of MAMP even in a lower reaction temperature, e.g. 70°C for MACP and 80°C for MAMP.

Figure 5 shows the dependence of $M_{n(GPC)}$s and PDIs on the monomer conversions. The $M_{n(GPC)}$s increased linearly with increasing monomer conversion, which was consistent with the polymerization proceeding in a controlled fashion. However, the $M_{n(GPC)}$s were slightly higher than the theoretical values at the early stage of the polymerization, and lower than the theoretical values at relatively

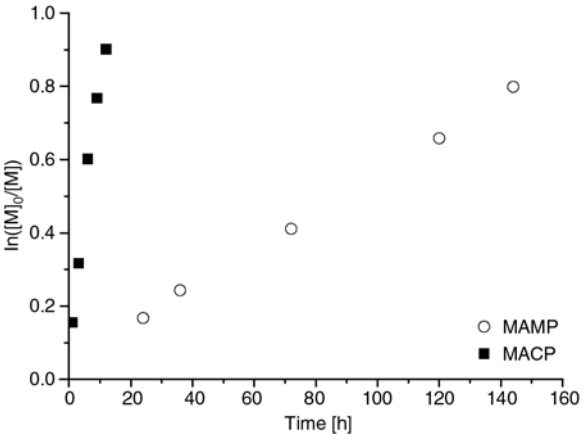

Figure 4. Relationships between $\ln([M]_0/[M])$ and the polymerization time for the RAFT polymerization of MACP at 70°C and MAMP at 80°C in anisole solution. $[MACP]_0$:$[AIBN]_0$:$[CPDB]_0$ = 200:1:3; $[MAMP]_0$:$[AIBN]_0$:$[CPDB]_0$ = 200:0.5:3.

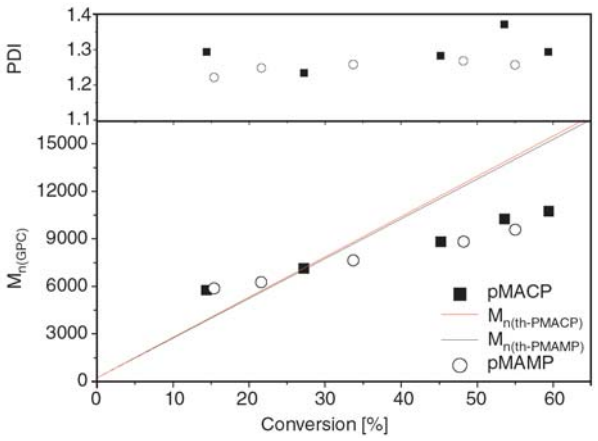

Figure 5. Evolution of $M_{n(GPC)}$ and PDI with monomer conversion for the RAFT polymerization of MACP at 70°C and MAMP at 80°C in anisole. Polymerization conditions are the same as in Figure 4.

high conversions. The theoretical molecular weight ($M_{n(th)}$) was calculated as Equation (1):

$$M_{n(th)} = \frac{[\text{monomer}]_0}{[\text{CPDB}]_0} \cdot MW_{\text{monomer}} \cdot \text{conversion} + \text{MW}_{\text{CPBD}} \quad (1)$$

where, $[\text{monomer}]_0$ and $[\text{CPDB}]_0$ were the initial concentration of monomer and CPDB, respectively, $\text{MW}_{\text{monomer}}$ and MW_{CPDB} were the molecular weights of monomers and CPDB, respectively. At the beginning of the polymerization, some positive deviation of $M_{n(GPC)}$s from the theoretical values ($M_{n(th)}$s) may be due to the incomplete usage of RAFT agent [42]. And at high monomer conversions, some negative deviation may be due to the side reactions of the initiator or initiator-derived radicals with the RAFT agent [32–36, 40]. On the other hand, the GPC standard calibration samples of PMMA may be the other cause of some deviations for $M_{n(GPC)}$ from the theoretical values. The PDIs of the polymers were relatively low up to high conversions in all cases (PDI≤1.37).

3.2. Synthesis of block copolymer (pMACP-b-PS, pMAMP-b-PS)

In order to further investigate the living behavior of the polymerization, the obtained polymer pMACP (M_n = 10560 g·mol^{-1}, PDI = 1.23) and pMAMP (M_n = 6440 g·mol^{-1}, PDI = 1.26), were used as the macro-RAFT agents to conduct chain extension experiments using styrene as the second monomer, respectively. The results were summarized in Table 1. The GPC profiles of the original macro-RAFT agent and chain extended polymer are shown in Figure 6, which demonstrated obvious peak shift from the macro-RAFT agent to the chain extended polymers. The molecular weight increased from 10560 to 16720 g·mol^{-1} for pMACP and 6440 to 10570 g·mol^{-1} for pMAMP, respectively, which demonstrated that most of the original polymer chains were active. The GPC traces of chain extended polymers showed trail at the position of original macro-RAFT agent. This should be caused by the non-dithioester terminated polymer (named as dead polymer) existed in the original macro-RAFT agent.

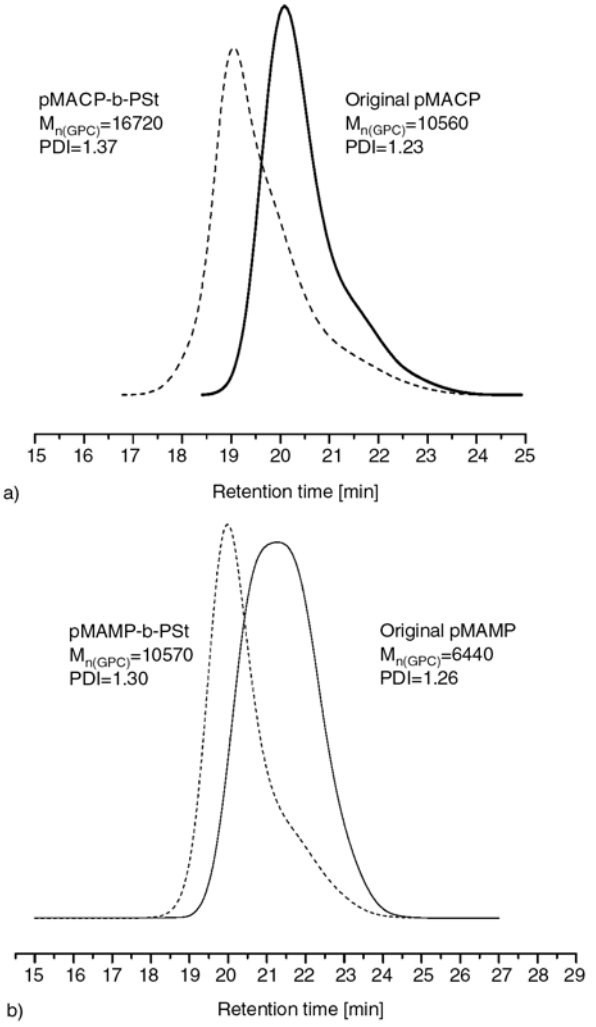

Figure 6. GPC traces for pMACP-*b*-PS (a) and pMAMP-*b*-PS (b) for chain extension using pMACP and pMAMP as macro-RAFT agents, respectively

3.3. Photochemical behaviors

As mentioned in the introduction part, azobenzene unit showed photo sensitive behaviors. The obtained polymers, pMACP and pMAMP, had high density of azobenzene units in their side chains. Thus, the *trans-cis* and *cis-trans* photo isomeriza-

Table 1. Chain-extension results using pMACP and pMAMP as the macro-RAFT agents and styrene as the monomer. $[\text{St}]_0$:$[\text{macro-RAFT}]_0$:$[\text{AIBN}]_0$ = 1000:3:1, 70°C, 12 h.

Label	Macro-RAFT agent		Conversion [%]	After chain extension	
	M_n	PDI		M_n	PDI
pMACP-*b*-PS	10560	1.23	21	16720	1.37
pMAMP-*b*-PS	6440	1.26	14	10570	1.30

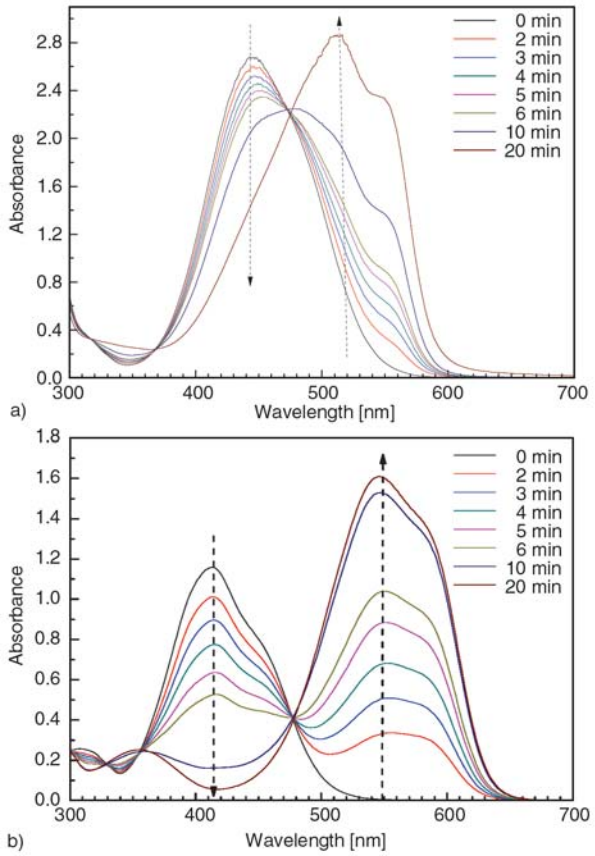

Figure 7. Changes in the UV-vis absorption spectra of pMACP (a – $M_{n(GPC)}$ = 10550 g·mol^{-1}, PDI = 1.30) and pMAMP (b – $M_{n(GPC)}$ = 8580 g·mol^{-1}, PDI = 1.27) under different irradiation time of 365 nm of UV light in chloroform solution at room temperature. The concentration of the solution was 2.5·10^{-6} mol·L^{-1}.

tion of pMACP and pMAMP in $CHCl_3$ solutions were studied. The polymer solutions were irradiated with 365 nm of UV light [43]. The UV-vis spectra of the samples after irradiated under 365 nm of UV light for different time were recorded as shown in Figure 7. The electronical properties of substituted group on azobenzene ring showed obvious effect on the photo isomerization behavior of polymer. It was interesting to find that the pMACP with electron donor (substituted amino group) and acceptor (cyano group) structure inside showed the enhanced absorption at 511 and 550 nm corresponding to n-π^* transition in *cis* isomer. At the same time, the absorption band corresponding to π-π^* transition in *trans* isomer at around 445 nm decreased remarkable (Figure 7a). During the *trans-cis* isomerization, the absorption peak at 521 and 445 nm showed serious overlap each other, which results in the appearance of a 'red-shift' peak from 445 to 528 nm. In the case of pMAMP with only the electron donor groups (substituted amino group and methoxy group), the similar results as pMACP under the irradiation of 365 nm light were observed, e.g. the enhancement of cis isomer n-π^* transition peak at 545 nm and weaken of *trans* isomer π-π^* transition peak at 412 nm. The red shift of π-π^* transition in electron-donor/acceptor substituted azobenzene, e.g. pMACP at 445 nm, compared with that of the electron-donating groups

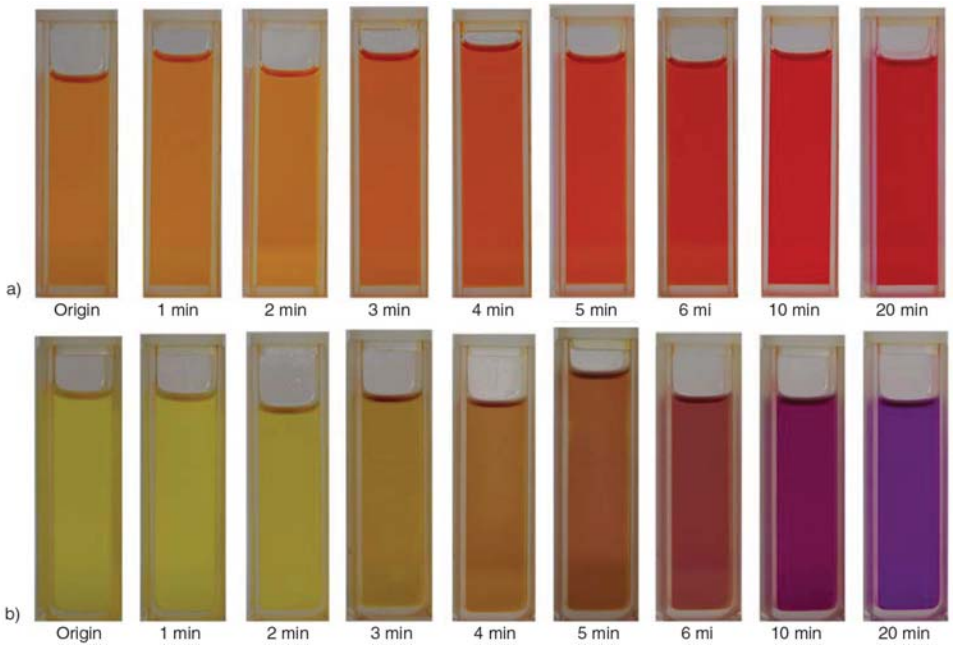

Figure 8. Color changes of pMACP and pMAMP in $CHCl_3$ solution with different irradiation time under 365 nm of UV light at room temperature. The concentration of the solution was 2.5·10^{-6} mol·L^{-1}. (a) for pMACP and (b) for pMAMP. The pMACP and pMAMP polymers used are the same as present in Figure 5.

substituted azobenzene, e.g. pMAPM at 412 nm, was observed [44]. While the *n*-π* transition is nearly constant in these cases, e.g. ranged from 520 to 550 nm [44]. It should be further noted that the red-shift value of pMAMP was much higher than that of pMACP, e.g. about 136 nm for pMAMP and 110 nm for pMACP, as showed in UV-vis spectra among the *trans-cis* transformation. Thus the color change of pMAMP solution under UV light of 365 nm irradiation should be more obvious than that of pMACP.

As shown in Figure 8, the color of pMAMP solution changed gradually from light yellow to purple with the irradiation time under 365 nm of UV light. However, it gradually changed from yellow to red for the color of pMACP solution under the irradiation of 365 nm of UV light. After 20 min of irradiation, further prolongation of the irradiation time did not show any color changes in both cases, which indicated that the *trans-cis* isomerization of azobenzene chromophores reached saturation after 20 min of irradiation.

The *trans-cis* isomerization showed thermally reversible properties in these two polymers solutions. The UV-vis spectra of the samples in chloroform during the thermal *cis-trans* isomerization process at 50°C for different time were traced and recorded as shown in Figure 9. The *cis-trans* isomerization completed after 12 h for pMACP, while it was 60 h for pMAMP. This result indicated that the electron donor-acceptor substitution on azobenzene ring would show significant effect on cis-trans isomerization rate [44]. Such isomerization rate of electron donor substituted azobenzene (pMAMP) was much slower than that of electron donor-acceptor substituted azobenzene (pMACP). To further testified such behavior, the photo isomerization kinetics were investigated using a similar method appeared in literature [43].

The *trans-to-cis* isomerization rates were recorded by determining the absorbance at 450 nm for pMACP and 415 nm for pMAMP, respectively, corresponding to the π-π* transition, after different irradiation time under 365 nm of UV light. The results are shown in Figure 10. The *cis-to-trans* isomerization rates were determined by tracking the UV-vis spectra for the pre-*tran-cis* isomerization saturated polymer solutions irradiated with 470 nm of UV light. The spectra changes of the reverse *cis-trans* photoisomerization at different time intervals

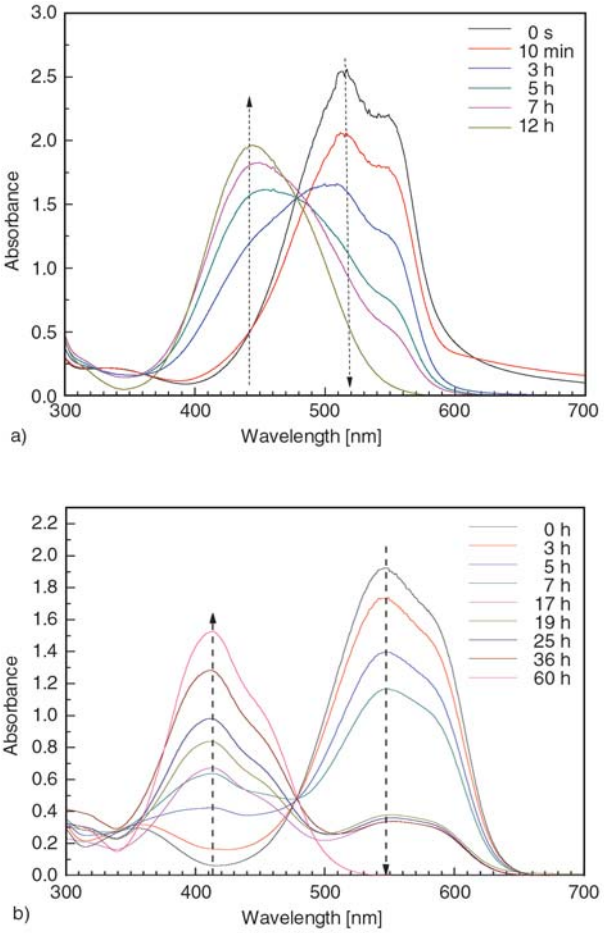

Figure 9. Changes in the UV-vis absorption spectra of pMACP (a – $M_{n(GPC)}$ = 10550 g·mol^{-1}, PDI = 1.30) and pMAMP(b – $M_{n(GPC)}$ = 8580 g·mol^{-1}, PDI = 1.27) in chloroform solution during the thermal *cis-trans* isomerization process at 50°C. The concentration of the solution was 2.5·10^{-6} mol·L^{-1}.

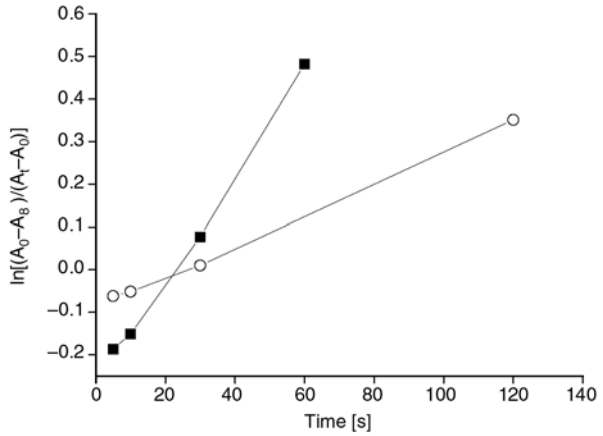

Figure 10. First-order plots for *trans-cis* isomerization of pMACP (■) and pMAMP (o). The concentration of polymer solution was 2.5·10^{-6} mol·L^{-1}, and the data were respectively recorded by monitor the absorbance at 450 and 415 nm for pMACP and pMAMP with different time interval under 365 nm of UV light irradiation.

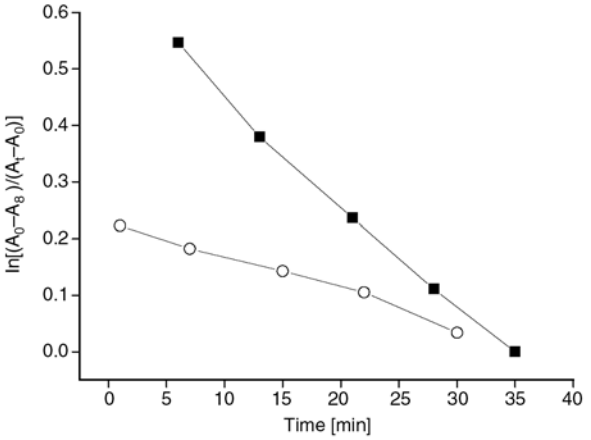

Figure 11. First-order plots for *cis-trans* isomerization of pMACP (■) and pMAMP (o). The concentration of polymer solution was $2.5 \cdot 10^{-6}$ mol·L^{-1}, and the data were respectively recorded by monitor the absorbance at 450 and 415 nm for pMACP and pMAMP with different time interval under 470 nm of UV light irradiation.

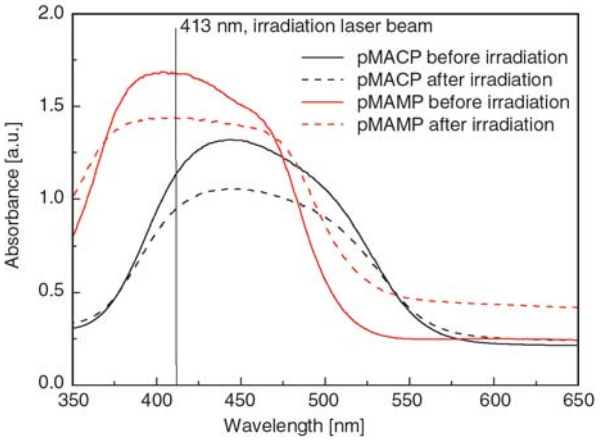

Figure 12. UV-vis absorption spectra of the films of pMACP ($M_{n(GPC)}$ = 8810 g·mol^{-1}, PDI = 1.28) and pMAMP ($M_{n(GPC)}$ = 8820 g·mol^{-1}, PDI = 1.27) on quartz glass before and after irradiation by 413 nm of UV light

are shown in Figure 11. The first-order rate constants were determined by fitting the experimental data to the Equation (2) [45, 46]:

$$\ln\left(\frac{A_\infty - A_0}{A_\infty - A_t}\right) = -k_{tc}t \tag{2}$$

where A_t, A_0 and A_∞ are absorbance at the maximum wavelength of 450 nm for pMACP and 415 nm for pMAMP at time t, time zero and infinite time (300 s in current experiment), respectively. The first-order plots according to this equation for *trans-cis* isomerization and *cis-trans* isomerization of azobenzene chromophore were shown in Figure 10 and Figure 11, respectively. The *trans-cis* photoisomerization rate constant, k_{tc}, as measured at room temperature in $CHCl_3$ were 0.0123 s^{-1} for pMACP and 0.0036 s^{-1} for pMAMP, respectively. The *cis-trans* photoisomerization rate constant, k_{tc}, as measured at room temperature in $CHCl_3$ were 0.0187 min^{-1} for pMACP and 0.0063 min^{-1} for pMAMP, respectively. The rates of *trans-cis* and *cis-trans* isomerization of pMAMP were slower than those of pMACP. The reason could be attributed to the donor-acceptor effect which effectively increased the energy of the N=N π-bonding orbital, thus lower the energy of the π*-antibonding orbital, then lowering the overall energy of the π-π* transition [47].

3.4. Photoinduced birefringence

It is well-known that a good matching of the absorption wavelength with the wavelength of the pumping laser has a positive effect on storage efficiency [10]. Being the absorption spectra of the investigated polymers quite similar, a laser light operating at 413.1 nm, in resonance with their intense electronic transition in the visible (Figure 12), has been used in the irradiation experiments in order to gain the same pumping efficiency. To assess the presence of photo-induced birefringence, films from pMACP ($M_{n(GPC)}$ = 8810 g·mol^{-1}, PDI = 1.28) and pMAMP ($M_{n(GPC)}$ = 8820 g·mol^{-1}, PDI = 1.27) were prepared by spin coating method. The film thicknesses were 107 nm for pMACP and 120 nm for pMAMP. Polymers films were irradiated with linearly polarized radiation (writing step) at 413.1 nm of wavelength under 5 mW/cm^2 of light intensity (I). After irradiation, the polymers showed high photo-induced linear birefringence (Figure 13) due to the homogeneously regular alignment of azobenzene chromophores, as evidenced by using a probe radiation at 650 nm, where the samples exhibit negligible absorption. The birefringence values can be determined by fitting the experimental data to the Equation (3):

$$\Delta n = \frac{\lambda}{\pi d}\arcsin\sqrt{\frac{I}{I_0 \sin^2 2\theta}} = \frac{\lambda}{\pi d}\arcsin\sqrt{\frac{I}{I_0}} \tag{3}$$

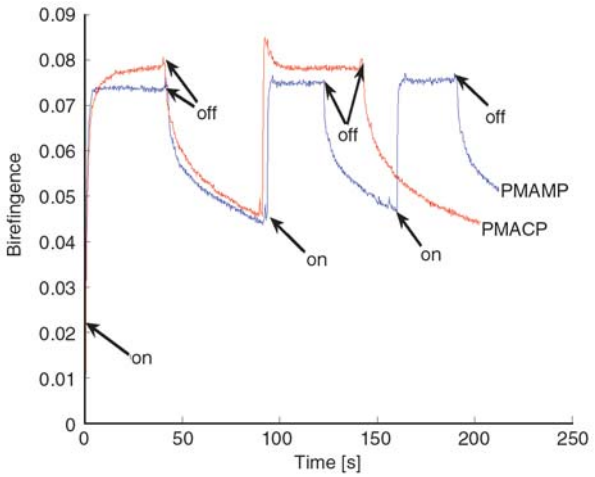

Figure 13. Photoinduced birefringence of pMACP ($M_{n(GPC)}$ = 8810 g·mol^{-1}, PDI = 1.28) and pMAMP ($M_{n(GPC)}$ = 8820 g·mol^{-1}, PDI = 1.27) films

where θ = 45°, Δn is the birefringence, λ is the wavelength of detection laser, d is the thickness of sample, I_0 is the intensity of polarized incident laser and I is the detected transition laser intensity after turn on the pump beam, θ is the angle of polarization between the pump beam and detect laser. Here, θ is 45°.

The birefringence was induced immediately under irradiation with a linearly polarized UV laser as the result of the alignment of the azo chromophores perpendicular to the laser polarization occurred on account of the *trans-cis-trans* isomerization of azo moieties. The rate of inducing birefringence of these polymer films was similar under the same writing beam power. Thus, these two substitution group (–CN and –OCH_3) bearing on the azobenzene chromophore did not show obvious effects on birefringence due to the similar size of these two groups [20]. The birefringence stabilized after turn on the inducing UV laser about 4 s for pMAMP and 6 s for pMACP. The maximum value of the photoinduced birefringence was about 0.073 for pMAMP and 0.079 for pMACP, respectively. After turn off the inducing UV laser, the birefringence was lost due to the azo chromophores relaxation. Finally, the birefringence of these two polymer films seems to be stabilized lower than 0.04. After that, the cycle between the birefringence induction and relaxation can be repeated in the same manner with the same level of birefringence at the same rate.

3.5. Photoinduced surface relief grating

For optical storage properties, creation of local holographic gratings is very important, and it is customary to report the diffraction efficiencies achieved on various materials [48]. SRG forming behavior of the synthesized azo polymers was characterized by the inscription rates and the saturation levels of SRG formation. The first order diffraction efficiency of the SRGs recorded *in situ* was used to characterize the surface modification [49–52]. The results were also compared with the surface deformation obtained from the AFM images. Low intensity of Kr^+ laser irradiation (30 mW/cm^2) was applied for the writing experiments in order to avoid the possible side effects caused by high intensity laser irradiation. For the comparable results, the laser intensity was kept the same during the experiments. The film thicknesses were 185 nm for pMACP and 200 nm for pMAMP.

It is worth to discuss the possible effects of polarity of the azobenzene groups on the SRG. Figure 14 shows the diffraction efficiency as a function of irradiation time for the films of pMACP ($M_{n(GPC)}$ = 8810 g·mol^{-1}, PDI = 1.28) and pMAMP ($M_{n(GPC)}$ = 8820 g·mol^{-1}, PDI = 1.27). In both cases, the diffraction efficiency of the SRGs increased with irradiation time and no difference of diffraction efficiency between them was found.

The formation of the SRG was confirmed by AFM images. Figure 15. (a 1) and 15. (b 1) show atomic force microscopy (AFM) image of the sinusoidal surface relief structures with regular spaces formed

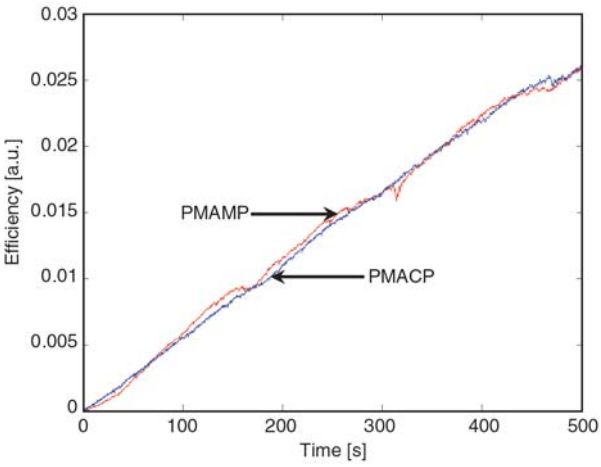

Figure 14. First-order diffraction efficiency signal for the gratings inscribed in pMACP ($M_{n(GPC)}$ = 8810 g·mol^{-1}, PDI = 1.28) and pMAMP ($M_{n(GPC)}$ = 8820 g·mol^{-1}, PDI = 1.27)

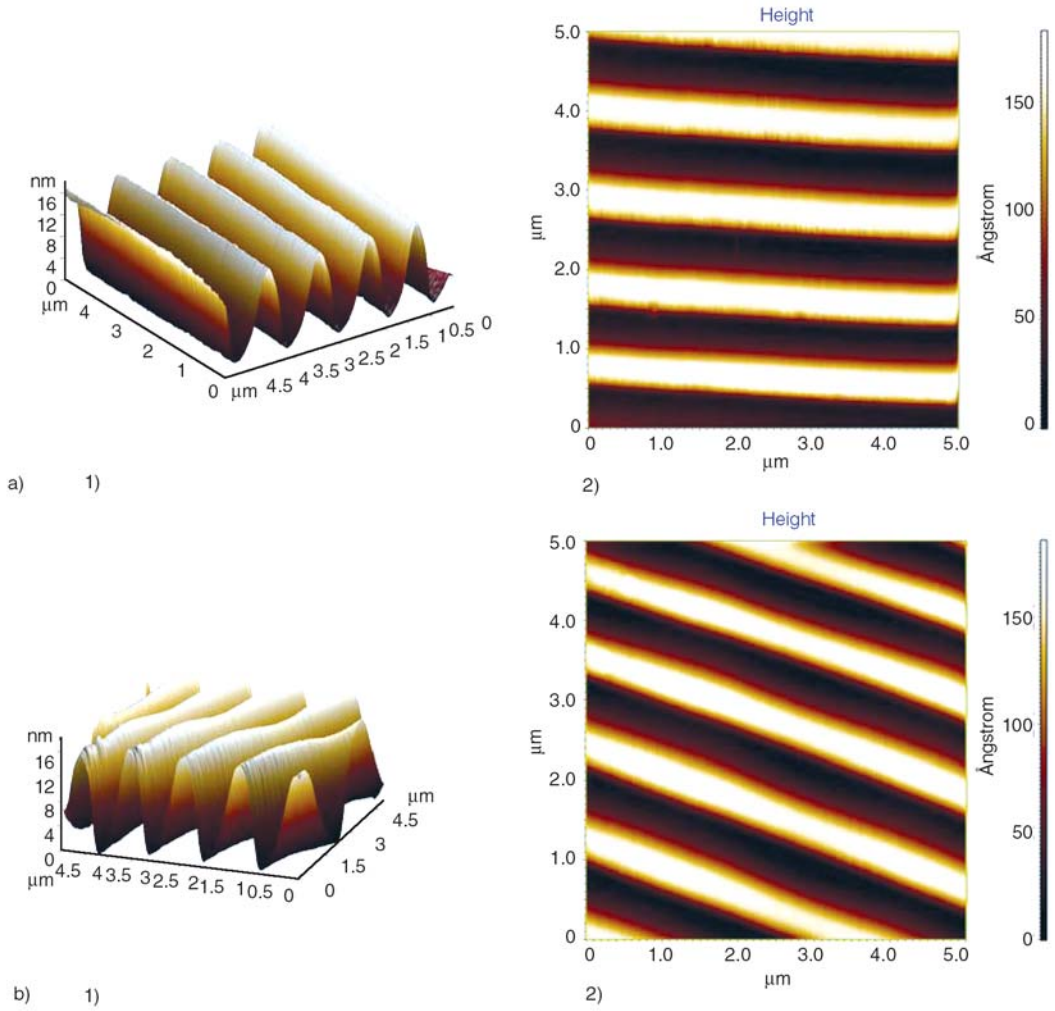

Figure 15. a – AFM images of the SRG inscribed on the pMACP film, prepared from sample with $M_{n(GPC)}$ = 8810 g·mol^{-1}, PDI = 1.28. b – AFM images of the SRG inscribed on the pMAMP film, prepared from sample with $M_{n(GPC)}$ = 8820 g·mol^{-1}, PDI = 1.27.

on the pMACP and pMAMP films. The grating depths, obtained through the AFM, were 15 and 18 nm for the samples (a) pMACP ($M_{n(GPC)}$ = 8810 g·mol^{-1}, PDI = 1.28) and (b) pMAMP ($M_{n(GPC)}$ = 8820 g·mol^{-1}, PDI = 1.27), respectively. Figure 15. (a 2) and 15. (b 2) show the AFM images of the SRG. The typical AFM images of the SRG with a grating periodicity around 1.0 µm were observed in these two polymer films.

4. Conclusions

Two azo polymers, pMACP and pMAMP with electronical push and pull substituents were synthesized through RAFT polymerizations. The polymerization showed the characteristics of 'living'/ controlled free radical polymerization. The isomerization rate of pMAMP was much slower than that of pMACP due to the donor-acceptor effect of the substituted azobenzene. The solution color of the polymers could be changed under irradiation of 365 nm of UV light because of the π-π* transition in *trans* isomer to *n*-π* transition in *cis* isomer. The light induced *tran-cis* isomerizations were confirmed to be thermally reversible. For the pMACP and pMAMP films, the diffraction efficiency of the SRGs increased with irradiation time and regular SRG images were obtained.

Acknowledgements

The financial supports of this work by the National Nature Science Foundation of China (No. 20574050), the Science and Technology Development Planning of Jiangsu Province (No. BK2007702 and BK2007048), the International Cooperation Foundation of Jiangsu Province (No. BZ2007037) and the Nature Science Key Basic Research of Jiangsu Province for Higher Education (No. 05KJA15008) are gratefully acknowledged.

References

[1] Gibbons W. M., Shannon P. J., Sun S-T., Swetlin B. J.: Surface-mediated alignment of nematic liquid crystals with polarized laser light. Nature, **351**, 49–50 (1991).

[2] Holme N. C. R., Ramanujam P. S., Hvilsted S.: 10 000 Optical write, read, and erase cycles in an azobenzene side-chain liquid-crystalline polyester. Optical Letters, **21**, 902–904 (1996).

[3] Katz H., Singer K., Sohn J., Dirk C., King L. A., Gordon H. M.: Greatly enhanced second-order nonlinear optical susceptibilities in donor-acceptor organic molecules. Journal of American Chemical Society, **109**, 6561–6563 (1987).

[4] Delaire J. A., Nakatani K.: Linear and nonlinear optical properties of photochromic molecules and materials. Chemical Reviews, **100**, 1817–1846 (2000).

[5] Todorov T., Nikolova L., Tomova N.: Polarization holography. 2: Polarization holographic gratings in photoanisotropic materials with and without intrinsic birefringence. Applied Optics, **23**, 4588–4591 (1984).

[6] Andruzzi L., Altomare A., Ciardelli F., Solaro R., Hvilsted S., Ramanujam P. S.: Holographic gratings in azobenzene side-chain polymethacrylates. Macromolecules, **32**, 448–454 (1999).

[7] Iftime G., Abarthet F. L., Natansohn A., Rochon P.: Control of chirality of an azobenzene liquid crystalline polymer with circularly polarized light. Journal of American Chemical Society, **122**, 12646–12650 (2000).

[8] Verbiest T., Kauranen M., Persoons A.: Second-order nonlinear optical properties of chiral thin films. Journal of Materials Chemistry, **9**, 2005–2012 (1999).

[9] Wu Y., Natasohn A., Rochon P.: Photoinduced birefringence and surface relief gratings in polyurethane elastomers with azobenzene chromophore in the hard segment. Macromolecules, **37**, 6090–6095 (2004).

[10] Natansohn A., Rochon P.: Photoinduced motions in azo-containing polymers. Chemical Reviews, **102**, 4139–4176 (2002).

[11] Mita I., Horie K., Hirao K.: Photochemistry in polymer solids. 9. Photoisomerization of azobenzene in a polycarbonate film. Macromolecules, **22**, 558–563 (1989).

[12] Naito T., Horie K., Mita I.: The effect of polymer rigidity on photoisomerization of 4-dimethylamino-4′-nitroazobenzene. Polymer Journal, **23**, 809–813 (1991).

[13] Ivanov S., Yakovlev I., Kostromin S., Shibaev V., Läsker L., Stumpe J., Kreysig D.: Laser-induced birefringence in homeotropic films of photochromic comb-shaped liquid-crystalline copolymers with azobenzene moieties at different temperatures. Die Makromolekulare Chemie, Rapid Communications, **12**, 709–715 (1991).

[14] Wiesner U., Reynolds N., Boeffel C., Spiess H. N.: Photoinduced reorientation in liquid-crystalline polymers below the glass transition temperature studied by time-dependent infrared spectroscopy. Die Makromolekulare Chemie, Rapid Communications, **12**, 457–464 (1991).

[15] Meerholz K., Volodin B. L., Sandalphon B., Kippelen B., Peyghambarian N.: A photorefractive polymer with high optical gain and diffraction efficiency near 100%. Nature, **371**, 497–500 (1994).

[16] Rochon P., Batalla E., Natansohn A.: Optically induced surface gratings on azoaromatic polymer films. Applied Physics Letters, **66**, 136–138 (1995).

[17] Sekkat Z., Wood J., Knoll W.: Reorientation mechanism of azobenzenes within the trans .fwdarw. cis photoisomerization. Journal of Physical Chemistry, **99**, 17226–17234 (1995).

[18] Ding L., Russell T. P.: A photoactive polymer with azobenzene chromophore in the side chains. Macromolecules, **40**, 2267–2270 (2007).

[19] Lissi E. A., Encinas M. V.: Photoinitiators for free radical polymerization. in 'Photochemistry and Photophysics' (ed.: Rabek J. F.) CRC Press, Boca Raton, vol 4, 221–294 (1990).

[20] Ho M. S., Barrett C., Natansohn A., Rochon P.: Azo polymers for reversible optical storage. 8. The effect of polarity of the azobenzene groups. Canadian Journal of Chemistry, **73**, 1773–1778 (1995).

[21] Cui L., Tong X., Yan X., Liu G., Zhao Y.: Photoactive thermoplastic elastomers of azobenzene-containing triblock copolymers prepared through atom transfer radical polymerization photoactive thermoplastic elastomers of azobenzene-containing triblock copolymers prepared through atom transfer radical polymerization. Macromolecules, **37**, 7097–7104 (2004).

[22] Mandal B. K., Jeng R. J., Kumar J., Tripathy S. K.: New photocrosslinkable polymers for second-order nonlinear optical processes. Die Makromolekulare Chemie, Rapid Communications, **12**, 607–612 (1991).

[23] Lambeth R. H., Moore J. S.: Light-induced shape changes in azobenzene functionalized polymers prepared by ring-opening metathesis polymerization. Macromolecules, **40**, 1838–1842 (2007).

[24] Wang X., Chen J-I., Marturunkakul S., Li L., Kumar J., Tripathy S. K.: Epoxy-based nonlinear optical polymers functionalized with tricyanovinyl chromophores. Chemistry of Materials, **9**, 45–50 (1997).

[25] Wang X., Kumar J., Tripathy S. K., Li L., Chen J-I., Marturunkakul S.: Epoxy-based nonlinear optical polymers from post azo coupling reaction. Macromolecules, **30**, 219–225 (1997).

[26] He Y., Yin J., Che P., Wang X.: Epoxy-based polymers containing methyl-substituted azobenzene chromophores and photoinduced surface relief gratings. European Polymer Journal, **42**, 292–301 (2006).

[27] Li Y., Deng Y., He Y., Tong X., Wang X.: Amphiphilic azo polymer spheres, colloidal monolayers, and photoinduced chromophore orientation. Langmuir, **21**, 6567–6571 (2005).

[28] Kato M., Kamigaito M., Sawamoto M., Higashimura T.: Polymerization of methyl methacrylate with the carbon tetrachloride/dichlorotris- (triphenylphosphine)ruthenium(II)/methylaluminum bis(2,6-di-tert-butylphenoxide) initiating system: Possibility of living radical polymerization. Macromolecules, **28**, 1721–1723 (1995).

[29] Wang J-S., Matyjaszewski K.: Controlled/'living' radical polymerization. Halogen atom transfer radical polymerization promoted by a Cu(I)/Cu(II) redox process. Macromolecules, **28**, 7901–7910 (1995).

[30] Matyjaszewski K., Xia J. H.: Atom transfer radical polymerization. Chemical Reviews, **101**, 2921–2990 (2001).

[31] Chiefari J., Chong Y. K., Ercole F., Kristina J., Jeffery J., Le T. P. T., Mayadunne R. T. A., Meijs G. F., Moad C. L., Moad G., Rizzardo E., Thang S. H.: Living free-radical polymerization by reversible addition-fragmentation chain transfer: The RAFT process. Macromolecules, **31**, 5559–5562 (1998).

[32] Moad G., Rizzardo E., Thang S. H.: Living radical polymerisation by the RAFT process. Australian Journal of Chemistry, **58**, 379–410 (2005).

[33] Moad G., Rizzardo E., Thang S. H.: Living radical polymerization by the RAFT process: A first update. Australian Journal of Chemistry, **59**, 669–692 (2006).

[34] Moad G., Rizzardo E., Thang S. H.: Radical addition-fragmentation chemistry in polymer synthesis. Polymer, **49**, 1079–1131 (2008).

[35] Barner-Kowollik C.: Handbook of RAFT polymerization. Wiley-VCH, Weinheim (2008).

[36] Favier A., Charreyre M-T.: Experimental requirements for an efficient control of free-radical polymerizations via the reversible addition-fragmentation chain transfer (RAFT) process. Macromolecular Rapid Communications, **27**, 653–692 (2006).

[37] Zhang Y., Cheng Z., Chen X., Zhang W., Wu J., Zhu J., Zhu X. L.: Synthesis and photoresponsive behaviors of well-defined azobenzene-containing polymers via RAFT polymerization. Macromolecules, **40**, 4809–4817 (2007).

[38] Sun B., Zhu X., Zhu J., Cheng Z., Zhang Z.: A novel synthetic method for well-defined polymer containing benzotriazole and bisazobenzene chromophore. Macromolecular Chemistry and Physics, **208**, 1101–1109 (2007).

[39] Hawker C. J., Bosman A. W., Harth E.: New polymer synthesis by nitroxide mediated living radical polymerizations. Chemical Reviews, **101**, 3661–3688 (2001).

[40] Chong Y. K., Krstina J., Le T. P. T., Moad G., Postma A., Rizzardo E., Thang S. H.: Thiocarbonylthio compounds [S=C(Ph)S-R] in free radical polymerization with reversible addition-fragmentation chain transfer (RAFT Polymerization). Role of the free-radical leaving group (R). Macromolecules, **36**, 2256–2272 (2003).

[41] Kim D. Y., Li L., Kumar J., Tripathy S. K.: Laser-induced holographic surface relief gratings on nonlinear optical polymer films. Applied Physics Letters, **66**, 1166–1168 (1995).

[42] Barner-Kowollik C., Buback M., Charleux B., Coote M. L., Darche M., Fukuda T., Goto A., Klumperman B., Klumperman B., Lowe A. B., Mcleary J. B., Moad G., Monteiro M. J., Sanderson R. D., Tonge M. P., Vana P.: Mechanism and kinetics of dithiobenzoate-mediated RAFT polymerization. I. The current situation. Journal of Polymer Science, Part A: Polymer Chemistry, **44**, 5809–5831 (2006).

[43] Zhang Q-Z., Sheng X., Li A-X., Yan W.: Study on photochemistry of photochromic liquid crystalline dendrimer of the first generation containing nitro groups (in Chinese). Acta Chimical Sinica, **14**, 1335–1342 (2005).

[44] Rau H.: Photoisomerization of azobenzenes. in 'Photoreactive Organic Thin Films'. (eds.: Sekkat Z., Knoll W.) Elsevier Science, San Diego, 3–49 (2002).

[45] Sin S. L., Gan L. H., Hu X., Tam K. C., Gan Y. Y.: Photochemical and thermal isomerizations of azobenzene-containing amphiphilic diblock copolymers in aqueous micellar aggregates and in film. Macromolecules, **38**, 3943–3948 (2005).

[46] Sasaki T., Ikeda T., Ichimura K.: Photoisomerization and thermal isomerization behavior of azobenzene derivatives in liquid-crystalline polymer matrixes. Macromolecules, **26**, 151–154 (1993).

[47] Rau H.: Photoisomerization of azobenzenes. in 'Photochemistry and Photophysics' (ed.: Rabek J. F.) CRC Press, Boca Raton, vol 2, 119–141 (1990).

[48] Natansohn A., Rochon P., Ho M-S., Barrett C.: Azo polymers for reversible optical storage. VI. poly[4-[2-(methacryloyloxy)ethyl]azobenzene. Macromolecules, **28**, 4179–4183 (1995).

[49] Barrett C., Natansohn A. L., Rochon P. L.: Mechanism of optically inscribed high-efficiency diffraction gratings in azo polymer films. Journal of Physical Chemistry, **100**, 8836–8842 (1996).

[50] Ho M. S., Barrett C., Paterson J., Esteghamatian M., Natansohn A., Rochon P.: Synthesis and optical properties of poly{(4-nitrophenyl)-[3-[N-[2-(methacryloyloxy)ethyl]-carbazolyl]]diazene}. Macromolecules, **29**, 4613–4618 (1996).

[51] Jiang X. L., Li L., Kumar J., Kim D. Y., Tripathy S. K.: Unusual polarization dependent optical erasure of surface relief gratings an azobenzene polymer film. Applied Physics Letters, **72**, 2502–2504 (1998).

[52] Tripathy S., Kim D. Y., Li L., Kumar J.: Photofabrication of surfaces for holograms. Chemtech, **28**, 34–40 (1998).

eXPRESS Polymer Letters Vol.2, No.8 (2008) 602–613
Available online at www.expresspolymlett.com
DOI: 10.3144/expresspolymlett.2008.72

A novel thermoplastic elastomer based on dynamically vulcanized polypropylene/acrylic rubber blends

B. G. Soares[1*], *D. M. Santos*[1], *A. S. Sirqueira*[2]

[1]Instituto de Macromoléculas, Universidade Federal do Rio de Janeiro, Centro de Tecnologia, Bloco J, Ilha do Fundão, 21945-970, Rio de Janeiro, RJ, P.O.Box 68525, Brazil
[2]Universidade Estadual da Zona Oeste, Rio de Janeiro, RJ, Brazil

Received 30 April 2008; accepted in revised form 10 July 2008

Abstract. Thermoplastic elastomer based on polypropylene (PP) and acrylic rubber (ACM) was investigated, with special attention on the compatibilization and dynamic vulcanization. ACM component contains chlorine and carboxyl groups along the backbone, which act as center for the curing and reactive compatibilization. The last event was carried out by adding a combination of maleic anhydride-modified PP (PP-g-MA) and triethylene tetramine (TETA), which act as interfacial agents between PP and ACM phases. The effectiveness of the compatibilization was suggested from mixing torque and viscosity, determined from rheological measurements. Outstanding mechanical performance, especially elongation at break, and better tensile set (lower values) were obtained with the compatibilization. The dynamic vulcanization also resulted in good mechanical properties for compatibilized blends, but the performance was inferior to that observed for non vulcanized blends. The effect of the compatibilization and/or dynamic vulcanization on the dynamic mechanical, thermal, morphological and stress relaxation properties was investigated.

Keywords: *polymer blends and alloys, acrylic rubber, TPV, reactive compatibilization, dynamic vulcanization*

1. Introduction

Polyacrylates (ACM) are oil resistant and high temperature resistant rubbers, which find important applications as oil seals and gaskets used in high performance auto engines [1]. Blending this rubber with a thermoplastic is a good approach for the development of oil resistant and processable materials. ACM is a saturated rubber and it is commercialized with different types of cure-site monomers [2, 3]. These sites can react with functional groups present in other polymers during the melt processing, producing graft copolymers or networks at the interface, which act as bridges between the phases. This process, known as reactive compatibilization, decreases the interfacial tension and increases the interfacial adhesion. Consequently a fine morphology is usually achieved for these blends, which contributes to an improvement of the overall properties. Some few examples of ACM – based elastomer thermoplastics are reported in the literature and include blends with nylon [4–7], poly(vinyl chloride) (PVC) [8, 9], poly(vinylidene fluoride) (PVDF) [10], poly (ethylene terephthalate) [11] and chlorinated polypropylene [12]. In all these blends, the thermoplastic component is polar, and presents some affinity with the ACM rubber. In the case of nylon or PET/ACM blends, the presence of the epoxide as the cure site monomer in the ACM backbone also provides an effective anchorage between the phases through the reaction between the epoxide groups of ACM and amino or carboxyl groups of nylon and PET, respectively [4, 11].

*Corresponding author, e-mail: bluma@ima.ufrj.br

Another important method to improve the elastomeric properties and processability of the thermoplastics is the dynamic vulcanization of the rubber phase in the presence of a suitable crosslinking agent, during the melt mixing with the thermoplastics, giving rise to a thermoplastic vulcanizate (TPV) [13]. This technique has been employed in the development of several TPVs. Most of them are constituted by polypropylene as the thermoplastic component and different vulcanized rubbers dispersed in the polypropylene matrix, such as ethylene-propylene-diene rubber (EPDM) [14–16], nitrile rubber [17–21] and natural rubber [22, 23], among others. However, to the best of our knowledge, there is no report in the accessible literature dealing with blends constituted by polypropylene and acrylic rubber.

Therefore, the aim of the present work is to investigate the performance of ACM as the rubber component in polypropylene- based thermoplastic elastomer blends. Because of the high incompatibility between the components, a technological compatibilization is necessary in order to improve the mechanical performance for commercial uses. The ACM grade used in this work was produced by Petroflex Ind. Com S.A. in Brazil, and contains double active cure-sites based on chlorine and carboxyl groups. Such functional groups can react with an appropriate functionalized polypropylene to promote a reactive compatibilization. This work evaluates the efficiency of maleic anhydride-grafted polypropylene (PP-g-MA) in combination with triethylenetetramine (TETA) as the reactive compatibilizer system for the PP/ACM blends. Figure 1 illustrates the possible reactions that should take place at the interface of these blends, during the melt processing. The effect of the reactive compatibilization and dynamic vulcanization on the mechanical, dynamic mechanical, rheological and morphological properties as well as stress relaxation behavior of PP/ACM blends was discussed in detail.

2. Experimental

2.1. Materials

Acrylic rubber, Hicryl 1540, (ACM), [derived from the polymerization of ethyl acrylate and containing carboxyl and chlorine as the double cure site groups; Mooney viscosity (ML 1+4 at 100°C) = 40] were kindly supplied by Petroflex Ind. Com. S.A. Rio de Janeiro, Brazil. Polypropylene (melt flow index = 3.5 g/10 min at 230°C/2.16 kg) was supplied by Braskem S.A., Rio Grande do Sul, Brazil. Maleic anhydride-modified polypropylene (PP-g-MA) (Polybond 3200) (melt flow index = 115 g/10 min at 190°C/2.16 kg; 1 wt% of maleic anhydride) was purchased by Crompton, Middlebury, CT, USA. Triethylene-tetramine (TETA), stearic acid and sodium stearate was purchased by Vetec Ind Quimicas, Rio de Janeiro, Brazil. WB-222, a processing agent based on aliphatic fatty acid esters, used for the ACM, was supplied by Struktol (Stow, Ohio, USA). Naphtenic oil is a mineral insulating oil produced by Petrobrás, Rio de Janeiro, Brazil. Chemac Park 50, a hexamethylenediamine carbamate, was supplied by Chemicon Ind. Quim. S.A., (São Paulo, Brazil).

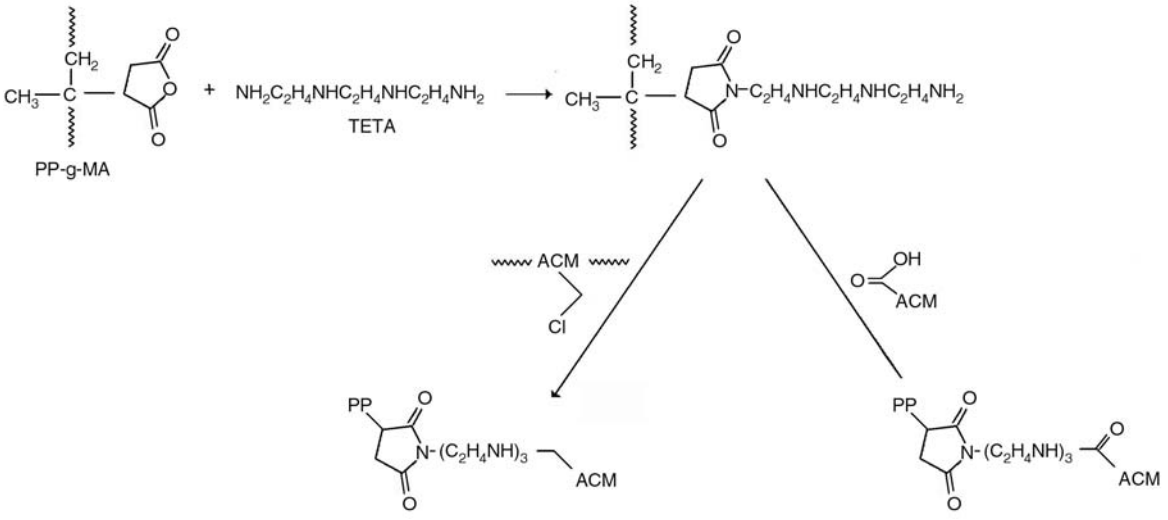

Figure 1. Possible reactions that occur at the interface of the compatibilized PP/ACM blends

2.2. Blend preparation

The blends were prepared in an internal Brabender plasticorder mixer (supplier), with banbury type rotors at 80 rpm at a mixer set point temperature of 185°C. PP was first charged and melted for 2 min in the chamber. Then, ACM was added and processed for 3 min, followed by the addition of naphtenic oil as the plasticizer. The mixing was continued for 7 min. In the case of compatibilized blends, PP-g-MA was added together with PP and TETA was added after the ACM addition and processed for 2 min. Then, the naphtenic oil was added and mixing was continued for 7 min.

For dynamically vulcanized blends, WB-222 and stearic acid were used as the processing aids. After the introduction of PP/PP-g-MA/ACM/TETA in this order, the processing aids (WB-222/stearic acid) were added. Two min later, sodium stearate was added and the mixture continued for 2 min, followed by the addition of Chemac Park 50, which was processed for an additional 3 min. The resultant blends were then discharged from the internal mixer in the form of lumps. The cooled lumps were milled and injection molded at 240°C with a pressure of 300 bar, in a Haake miniJet.

2.3. Physical testing

Tensile testing was done following the ASTM D638-5 method using dumb bell shaped samples at a cross-head speed of 100 mm/min with an Instron 5569 universal testing machine (Boston, MA, USA). Five specimens were used and the average was calculated in each case.

For the compression set test, cylindrical test specimens (12.5 mm diameter and 6.0 mm thickness) were injected at 240°C. The tests were done by pressing the specimens to 25% of their original thickness, according to ASTM D395-85 and aged in an air oven of controlled ventilation at 100°C for 22 h before determining their thickness recovery upon release of the compressive force.

Tension set and stress relaxation experiments were also performed in a Universal testing machine (Instron 5569). For tensile set experiments, the specimens were elongated until 50 or 100% of deformation at the rate of 100 mm/min and 25°C and kept at that position for 10 min. It was relaxed back to unstressed condition and equilibrated for 24 h. The percentage of change in the length of the sample before and after extension was taken as tension set. For the blends that did not exceed 50 or 100% elongation, tension set at break was reported. Stress relaxation experiments were carried out in a Universal testing machine (Instron 5569). The dumb bell shaped specimens were pulled to the 100% elongation at a strain rate of 100 mm/min and the decay in stress as a function of time was recorded.

2.4. Oil resistance

The oil resistance of the samples was determined by immersing the specimens in ASTM #3 oil at 100°C for 22 h, as per ASTM D471-98.

2.5. Dynamic mechanical analysis

The dynamic mechanical analyses of the blends were obtained by using the DMA analyzer (Q800; TA Scientific, New Castle, DE). The sample specimens were analyzed in single cantilever mode at a constant frequency of 1 Hz, strain amplitude of 30 μm and temperature ranging from –50 to +40°C, with a heating rate of 2°C/min. The temperature corresponding to the peak in tanδ versus temperature plot was taken as the glass-to-rubber transition temperature (T_g).

2.6. DSC analysis

The melting and crystallization behaviors of PP/ACM blends were determined using a Perkin-Elmer DSC-7 apparatus. The samples were heated at a rate of 10°C/min from 40 to 200°C and annealed at 200°C for 5 min, in order to remove any crystalline nuclei. The samples were then cooled to 40°C at a rate of 10°C/min and heated again to 200°C at a rate of 10°C/min.

2.7. Scanning electron microscopy

Scanning electron microscopy (SEM) was performed on a JEOL 5610 LV equipment (Tokyo, Japan) using backscattered electron detector and a voltage of 15 kV. The samples were cryo-fractured and the surface was treated with ruthenium tetroxide (RuO_4) for 5 min in order to selectively stain the acrylic rubber phase. The samples were then coated with a thin layer of carbon and observed by SEM.

2.8. Rheological properties

Rheological characterization of the systems was carried out using an Anton Paar Physica MCR301 rheometer (Graz, Austria) disposed with parallel-plates with a diameter of 25 mm. The measurements were done at 220°C. For strain sweep measurements, it was used a strain range of 10^{-2} to 300% and an angle frequency of 7.5 rad/s. The measurements with frequency sweep were done at a constant strain of 2.5% and a frequency range of 0.1 to 100 rad/s.

3. Results and discussion

3.1. The Effect of the Compatibilization

3.1.1. Brabender data

The effect of PP-g-MA/TETA compatibilizing system was first investigated in non vulcanized PP/ACM (50:50 parts) blends. Figure 2 shows the actual temperature versus time plots for the blends as a function of the compatibilization. The amount of PP-g-MA was fixed as 5% and the TETA, used as the coupling agent, was varied. All blends exhibited an increase of the internal temperature in the mixer, which were higher than the setting temperature. This is due to the viscous heating of the polymers during the processing. For compatibilized blends (curves B and C), the actual temperature in the mixer reached 200°C, due to both viscous heating of the highly viscous network formed by the reaction between the functional groups and also due to the exothermic heat of the chemical reactions.

The variation of the torque during time blending also gives information regarding the extent of the reaction which occurs during the reactive compatibilization of a blend in the melt. Figure 3 shows the torque versus time plots for these blends as a function of the compatibilization. The first increase in torque was related to the PP feed torque. At this stage, the torque level was lower for compatibilized blends because of the presence of the PP-g-MA (which has a lower viscosity compared to pure PP). After the ACM addition, the torque level increased and this effect was more pronounced in compatibilized blends because of the interactions between the ACM and PP-g-MA. The torque decreased with the addition of TETA (point a) because of the introduction of the low molecular weight component, but immediately increased and reached a plateau higher than that of non compatibilized blend as a consequence of the chemical reactions between the functional groups of ACM and PP-g-MA with TETA, as illustrated in Figure 1. The addition of higher amount of TETA (curve C) contributed to an additional increase of torque probably because of the higher amount of crosslinked material formed at the interface, giving rise to a more viscous system. After the addition of the plasticizer (point b) the torque leveled off and stabilized in a higher level than that of non compatibilized blend. These results confirm the reactive compatibilization of these blends during melting.

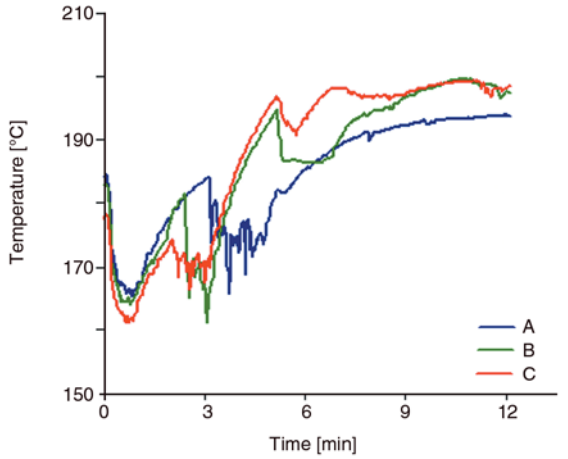

Figure 2. Dependence of the actual temperature with the time for non vulcanized PP/ACM (50:50 parts) blends, as a function of the compatibilization. (A) non compatibilized blend; and compatibilized blend with 5% of PP-g-MA and (B) 0.2% of TETA or (C) 0.5% TETA.

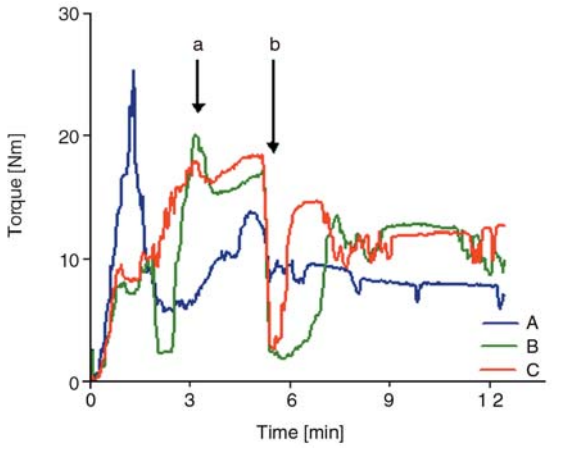

Figure 3. Dependence of the torque with time for non vulcanized PP/ACM (50:50 parts) blends, as a function of the compatibilization. (A) non compatibilized blend; and compatibilized blend with 5% of PP-g-MA and (B) 0.2% of TETA or (C) 0.5% TETA.

3.1.2. Rheological studies

The reactive compatibilization was also evidenced from rheological experiments. Figure 4 illustrates the dependence of the storage modulus (G') with the frequency for non compatibilized and compatibilized PP/ACM blends. The compatibilizing blends displayed higher storage modulus, confirming the presence of entanglements at the interface as a consequence of the reactive compatibilization. Blend containing 0.5% of TETA (curve C) presented lower values of G', probably because of the lubricating effect of this coupling agent, TETA, which competes with the network formation at the interface. The compatibilization also resulted in a substantial increase of the viscosity, as illustrated in Figure 5. At low deformation, the viscosity of the blend containing 0.5% of TETA was lower than that one containing 0.2% TETA, because of the lubricating effect of the TETA. However, at higher deformation, the viscosity of the blend containing higher amount of TETA was higher because of the formation of junction points at the interface in a higher extent.

The possible reactions which occur during processing of the compatibilized blends are illustrated in Figure 1. The use of PP-g-MA needs the presence of TETA to promote the coupling reaction. The amino groups of TETA react with the anhydride groups of the PP-g-MA forming the imide group. The other amino groups in this new functionalized PP may react with both carboxyl groups and chlorine groups located on the ACM backbone. These reactions give rise to a network at the interface, which is responsible for the increase of torque and viscosity of the blend.

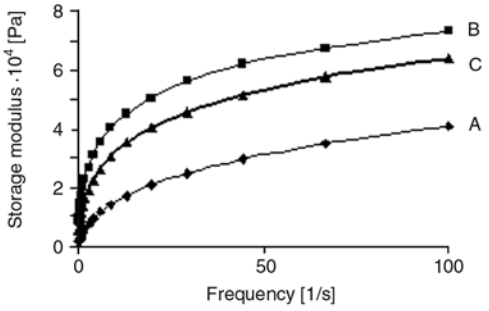

Figure 4. Dependence of storage modulus (G') with frequency for non vulcanized PP/ACM (50:50 parts) blends, as a function of the compatibilization. (A) non compatibilized blend; compatibilized blend with 5% of PP-g-MA and (B) 0.2% of TETA or (C) 0.5% TETA.

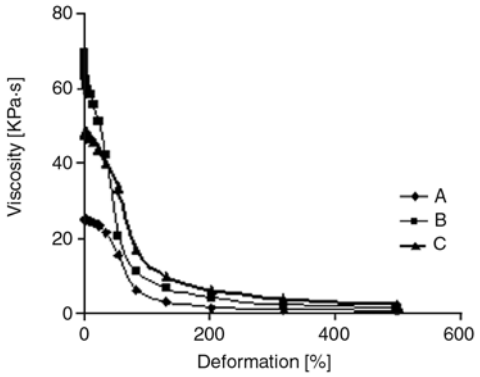

Figure 5. Dependence of viscosity with deformation for non vulcanized PP/ACM (50:50 parts) blends, as a function of the compatibilization. (A) non compatibilized blend; and compatibilized blend with 5% of PP-g-MA and (B) 0.2% of TETA or (C) 0.5% TETA.

3.1.3. Physical and mechanical properties

Table 1 summarizes the physical and tensile properties of non vulcanized PP/ACM (50:50 parts) blends. The compatibilization resulted in a significant improvement of tensile properties, especially the elongation at break. The oil resistance was also improved with the compatibilization. Compatibilized blends also exhibited superior tension set at 50 and 100% elongation, that is, lower tension set value. The tension set of non compatibilized blend could not be determined at 100% elongation because failures of specimen occurred at elongation

Table 1. Physical and mechanical properties of non vulcanized PP/ACM blends

Ingredients (by weight)	NV1	NV2	NV3
PP	50	45	45
ACM	50	50	50
PP9g-MA	0	5	5
TETA	0	0.2	0.5
Naphtenic oil	10	10	10
Physical properties			
Ultimate tensile strength [MPa]	11.2 ± 0.6	15.3 ± 0.4	15.9 ± 0.3
Elongation at break [%]	73 ± 20	280 ± 30	340 ± 15
Compression set [%]	89 ± 1	91 ± 1	83 ± 3
Tension set (at 50% deformation) [%]	5.9± 0.5	3.2± 0.5	2.1± 0.5
Tension set (at 100% deformation) [%]	28.2± 0.5[a]	14.8± 0.5	19.6± 0.5
Swelling in ASTM #3 oil [%]	8.1 ± 0.5	6.5 ± 0.2	5.8 ± 0.4

NV = non vulcanized blends
[a]tension set at break

at break lower than 100%. These results indicate good elastomeric properties, promoted by a reduced interfacial tension between the phases and by a stable dispersion of the rubber particles.

3.2. The effect of dynamic vulcanization

As extensively reviewed in the literature, the best way to produce thermoplastic elastomer blends containing finely dispersed rubber phase is through the dynamic vulcanization. Table 2 presents the main physical and tensile properties of the dynamically vulcanized PP/ACM blends. The reactive compatibilization was also effective in dynamically vulcanized blends, when it was observed a significant increase of tensile properties. This behavior may be attributed to a decrease of the interfacial tension promoted by the compatibilization, resulting in rubber domains with smaller particle size, which can be completely encapsulated by the less viscous PP component.

The compatibilization also improved the tensile set of vulcanized blends. As observed in Table 2, the compatibilized blends presented good tension set behavior (lower values) for experiments performed at 50 or 100% of deformation. The non compatibilized blends presented higher values or, in the case of 100% of elongation, the specimens broke during the experiment and could not be tested.

Table 2. Physical and mechanical properties of vulcanized PP/ACM blends

Ingredients (by weight)	V1	V2
PP	50	50
ACM	50	50
PPg-MA	0	5
TETA	0	0.2
Stearic acid	1	1
WB-222	1.5	1.5
Sodium stearate	1.0	1.0
Chemac Park 50	1.5	1.5
Physical properties		
Ultimate tensile strength [MPa]	11.0 ± 0.6	16.5 ± 0.2
Elongation at break [%]	50 ± 5	190 ± 4
Compression set [%]	89 ± 1	82 ± 2
Tension set (at 50% elongation) [%]	9.3 ± 0.5	6.3± 0.5
Tension set (at 100% elongation) [%]	–	24.6± 0.5
Swelling in ASTM #3 oil [%]	4.6 ± 0.5	4.2 ± 0.2

3.3. Morphology

The mechanical properties, especially elongation at break and tension set, were superior in non vulcanized blends, and can be explained by the morphology of the rubber dispersed phase. Figure 6 compares the SEM micrographs of PP/ACM (50:50 parts) blends as a function of the compatibilization and vulcanization. The white region corresponds to the rubber phase, which was selectively stained by RuO_4. Non vulcanized and non compatibilized blend presented a co-continuous structure, with large rubber phase because of the incompatibility between the phases. The compatibilization promoted a phase inversion with the rubber particle uniformly distributed inside the PP matrix (Figure 6b). This morphology is in agreement with the outstanding mechanical performance observed for this blend. Contrarily to the usual behavior of dynamic vulcanized blends, the vulcanization of PP/ACM blends resulted in a gross phase separated morphology. The non compatibilized blend presented very large rubber particle domains, as observed in Figure 6c. The reactive compatibilization improved the morphology, resulting in smaller crosslinked rubber particles, well dispersed inside the PP matrix (Figure 6d). However, this compatibilized blend still presents gross phase separated morphology, as compared to the non vulcanized blend (Figure 6b).

The curing process of the ACM rubber phase performed by Chemac Park 50 (a hexamethylene diamine carbamate) is believed to involve the reaction between hexamethylene diamine (generated from the decomposition of Chemac Park 50 at high processing temperature) and chloride and/or carboxylic groups of ACM, according to the scheme proposed in Figure 7. The curing system was added 3 min after the addition of the processing aid systems. Therefore, it is believed that the curing process started to occur before the rubber domains have enough time to deform and break up into smaller particles. Consequently, larger vulcanized domains of rubber were obtained. The compatibilization decreases the interfacial tension and avoids coalescence until the addition of the curing agent, contributing for the formation of smaller rubber particle size, and consequently an improvement of the mechanical performance.

Regarding the compatibilized, but non vulcanized blends, after the introduction of TETA and the pro-

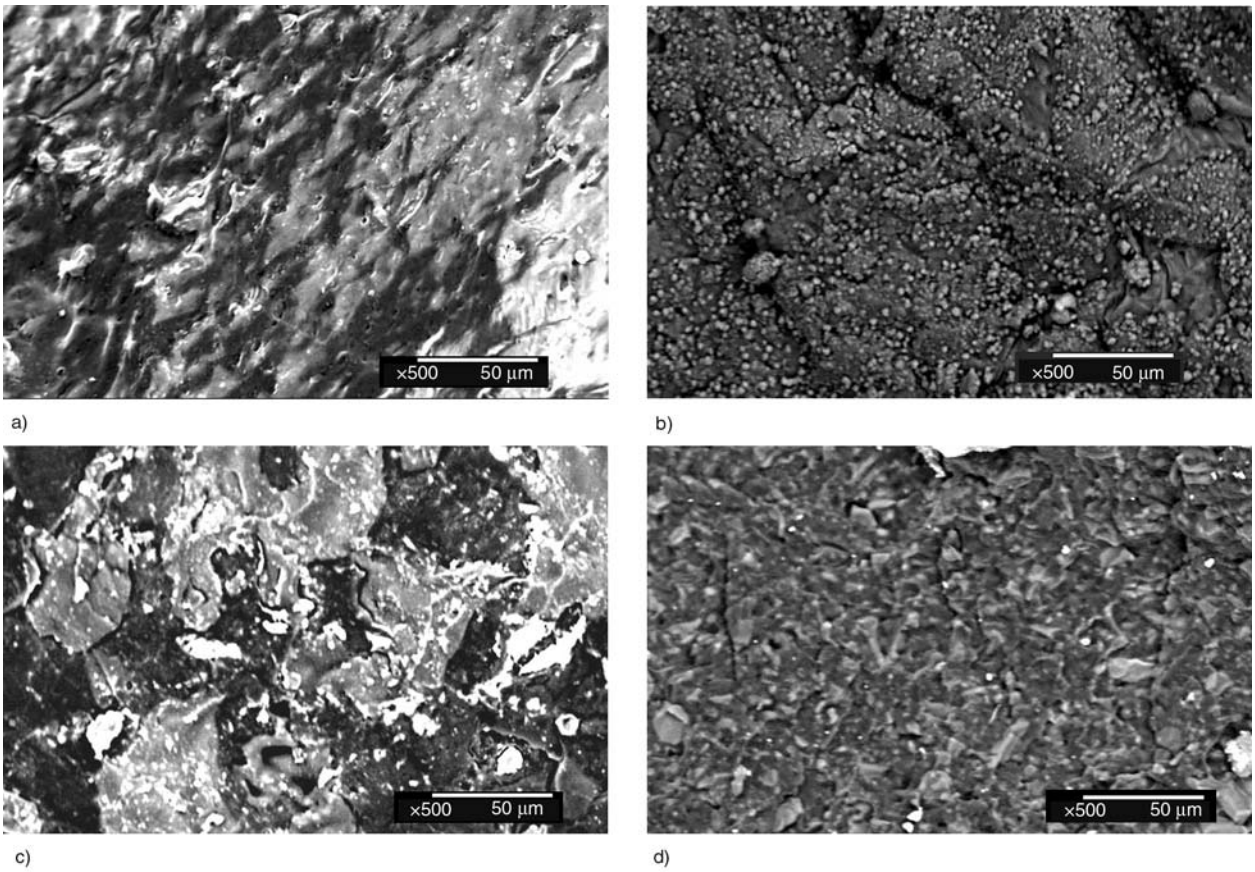

Figure 6. SEM micrographs of PP/ACM (50:50 parts) blends: (a) non vulcanized/non compatibilized; (b) non vulcanized/compatibilized with PP-g-MA/TETA (5:0.5); (c) vulcanized/non compatibilized; (d) vulcanized/compatibilized with PP-g-MA/TETA (5:0.5)

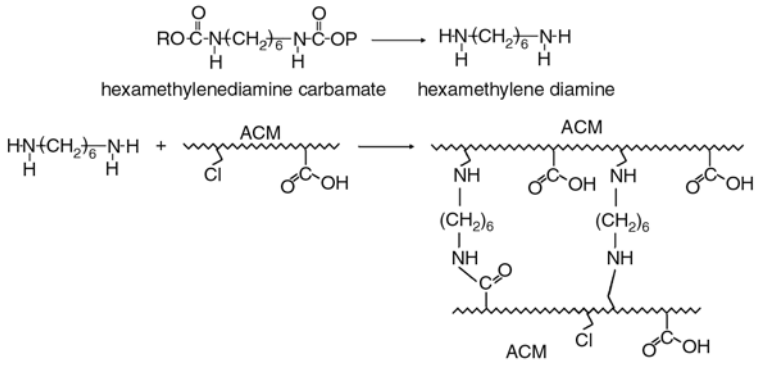

Figure 7. Proposal of the curing mechanism of ACM phase by hexamethylene diamine carbamate

cessing aid, this blend was processed for additional 7 min, which imparts the break up of the droplets in higher extent and a more effective dispersion of the rubber particle inside the PP matrix. In addition, TETA is a diamine compound (similarly to the decomposed form of Chemac Park 50) and may also react with the functional groups of the ACM phase, introducing some crosslinking into this phase. Therefore, the presence of TETA promoted a decrease of the interfacial tension, an improvement of the interfacial adhesion and the crosslinking of the rubber particles. All these features contribute for an improved morphology and the outstanding elastomeric properties of this blend.

3.4. Stress relaxation experiments

The improvement of the elastomeric characteristics of PP/ACM blends with the compatibilization was also observed from stress relaxation experiments

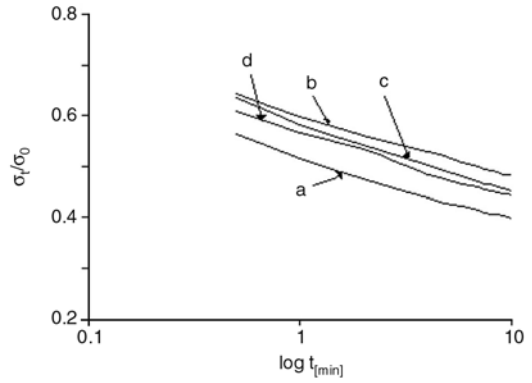

Figure 8. (σ_t/σ_0) versus log*t* plots of non vulcanized and vulcanized PP/ACM (50:50 parts) blends at a strain level of 100% (a) non vulcanized/non compatibilized blend; non vulcanized/compatibilized blend with (b) PP-g-MA/TETA (5:02); (c) PP-g-MA/TETA (5:0.5); (d) vulcanized and compatibilized with PP-g-MA/TETA (5:0.5)

carried out at 25°C. Figure 8 illustrates the (σ_t/σ_0) versus time plots for non vulcanized and vulcanized ACM/PP blends at 100% strain, where σ_t is the stress at time t and σ_0 is the stress at $t = 0$. In all blends, the experimental points fell on a single straight line, indicating that the relaxation process involves a single mechanism [24]. For non vulcanized blends the compatibilization resulted in slightly lower stress relaxation (lower stress decay). In addition the value of (σ_t/σ_0) for the same time is higher for compatibilized and non vulcanized blends, indicating an increasing of the elastic property of these blends because of the effective entanglement of the chains at the interface. The dynamic vulcanization resulted in a little higher stress relaxation (curve d). The best elastic response was observed for compatibilized/non vulcanized PP/ACM blends. This behavior confirms the good interfacial adhesion between the ACM and PP phases promoted by the PP-g-MA in combination with TETA as the coupling agent, and the crosslinking of the rubber particles.

3.5. Dynamic mechanical analysis

The dynamic mechanical properties such as storage modulus (E') and damping (tanδ) of the PP/ACM blends were evaluated from –60 to +60°C. Figure 9 illustrates the variation of the storage modulus (E') with the temperature for non vulcanized and dynamically vulcanized PP/ACM (50:50 parts) blends, as a function of the compatibilization. In both vulcanized and non vulcanized blends, those containing the compatibilizing system displayed the highest storage modulus over the entire temperature range. In non vulcanized blends, the increase in TETA content resulted in a substantial increase of modulus (curve c). These results are in agree-

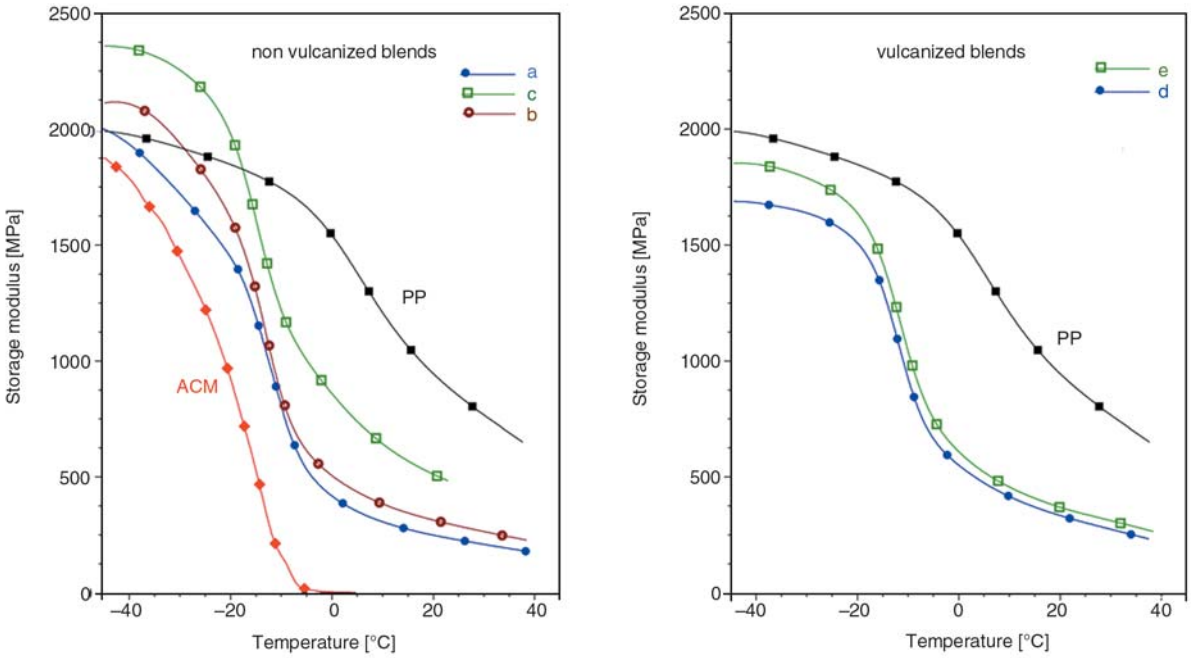

Figure 9. Dependence of storage modulus (E') with the temperature for PP/ACM (50:50 parts) blends: (a) non vulcanized/non compatibilized blend; non vulcanized/compatibilized blend with PP-g-MA/TETA (b) (5:0.2 parts) and (c) (5:0.5 parts); (d) vulcanized/non compatibilized blend; (e) vulcanized/compatibilized blend with PP-g-MA/TETA (5:0.5).

Table 3. DMA and DSC results of PP/ACM (50:50 parts) blends as a function of the compatibilization

Compatibilizing system [wt%]		DMA results				DSC results		
PP-g-MA	TETA	tanδ	T_g [°C]	E′ (–40°C) [MPa]	E′ (20°C) [MPa]	T_m [°C]	ΔH [J/g]	T_c [°C]
Non vulcanized blends								
0	0	0.31	–8.4	1930	230	159.8	36.0	113
5	0.2	0.26	–10.3	2100	290	161.1	37.5	120
5	0.5	0.16	–12.7	2350	490	161.3	38.6	120
Vulcanized blends								
0	0	0.27	–9.3	1680	300	161.0	37.8	114
5	0.5	0.21	–10	1850	380	165.0	40.6	120

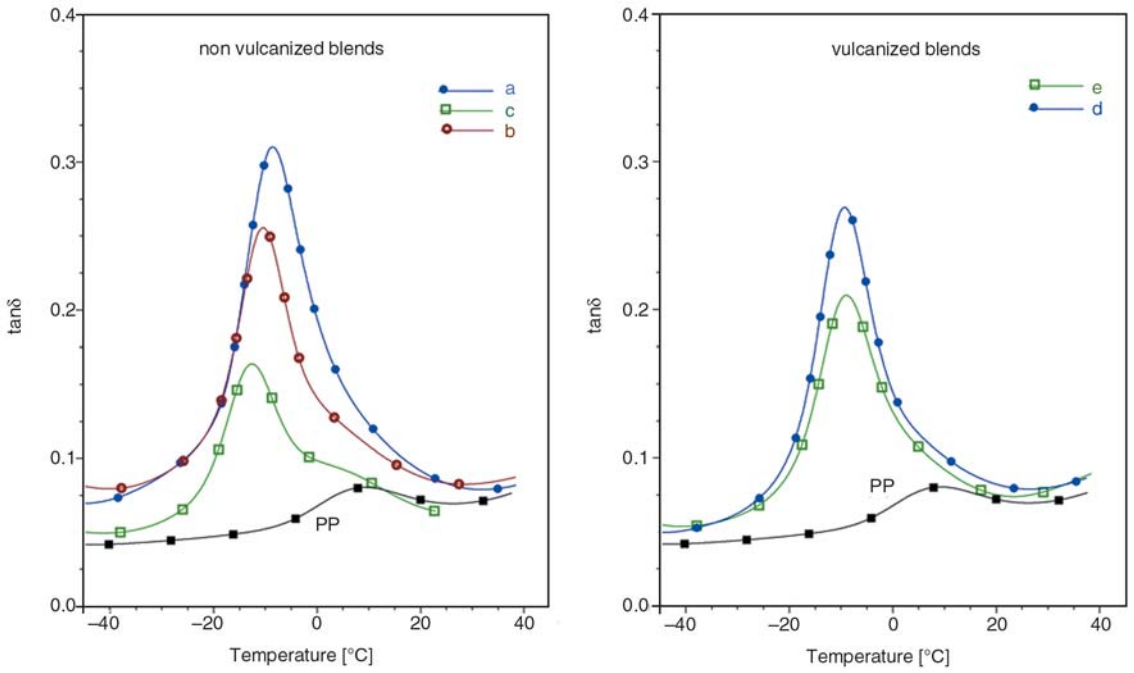

Figure 10. Dependence of tanδ with the temperature for PP/ACM (50:50 parts) blends: (a) non vulcanized/non compatibilized blend; non vulcanized/compatibilized blend with PP-g-MA/TETA (b) (5:0.2parts) and (c) (5:0.5parts); (d) vulcanized/non compatibilized blend; (e) vulcanized/compatibilized blend with PP-g-MA/TETA (5:0.5)

ment with the mechanical performance and confirm the interfacial adhesion caused by the emulsifying effect of the network formed at the interface, as a consequence of the reactive compatibilization. These interactions increase the stiffness of the material and reflect on the increase of modulus of the blends at room temperature. The values of modulus and other dynamic mechanical parameters are also summarized in Table 3.

The dependence of tanδ with the temperature for PP/ACM blends is illustrated in Figure 10. The main relaxation at around –10°C is related to the glass-rubber transition of the ACM phase. The relaxation due to the PP phase appears at around 10–15°C, but it is only detected as a small shoulder at this temperature region because of its very low damping when compared to the ACM. The compatibilized blends presented a decrease of damping (tanδ) due to the decrease of the chain mobility as a result of the interfacial adhesion. Comparing the vulcanized and non vulcanized blends with the same composition, the vulcanized but non compatibilized blend displayed lower tanδ, due to the mobilization restriction imparted by the crosslinks. However, for compatibilized blends lower tanδ and higher E' values were observed in non vulcanized blend. This behavior suggests that the compatibilizing system imparts some crosslinking to the rubber phase, and the posterior vulcanization may result an overcuring process and degradation of the blend, which decreases the crosslinking density of this blend. This behavior explains the inferior mechanical properties of the vulcanized blends when compared to the non vulcanized ones.

The glass transition temperature (established as the temperature corresponding to the maximum of the

tanδ peak) presented a slight decrease with the compatibilization, for non vulcanized blends. However, for vulcanized blends, the compatibilization did not exert influence on the transition temperature.

3.6. DSC analysis

The effect of the compatibilization and the dynamic vulcanization on the thermal behavior of PP/ACM (50:50 parts) blends was studied by differential scanning calorimetry, whose main results are summarized in Table 3. The addition of the compatibilizing agent increased both T_m and T_c of the PP phase, but the effect was more pronounced in the T_c values. Also the melt enthalpy presented a little increasing with the compatibilization. These results suggest that the compatibilization restricts the movement of the macromolecular chain because of the enhanced interaction between the phases, resulting in higher T_m values. In addition, the compatibilizing agent acts as a nucleating agent increasing the melt enthalpy.

3.7. Effect or reprocessing

An important advantage of TPVs over conventional thermosetting rubbers is that they can be reprocessed by all common equipment for plastic processing, without significant changes in physical properties. The reprocessability was tested in compatibilized blends (non vulcanized and vulcanized blends). The blends were studied after three cycles of injection molding, with the product being reground after each molding cycle. The tensile properties were measured after each cycle, and the results are summarized in Table 4. Both non vulcanized and vulcanized blends presented an increase of ultimate tensile strength after the first cycle, indicating additional interactions and/or crosslinking taking place at this stage. After the second and third cycles, the tensile strength decreased, but the values still remained higher than the original values. The elongation at break decreased after the first cycle for non vulcanized blend. However, for vulcanized blend, it was observed an increase of this value with reprocessing. These results indicate that these blends can be considered a reprocessable thermoplastic elastomer.

4. Conclusions

Thermoplastic elastomers based on polypropylene and acrylic rubber were studied for the first time, with special emphasis on the effect of the reactive compatibilization and dynamic vulcanization. The compatibilization with maleic anhydride-functionalized PP/TETA system resulted in a significant improvement of mechanical properties and oil resistance. In addition it was observed a significant improvement on the elasticity of the material as indicated by the lower tension set values and a lower stress relaxation. The reactive compatibilization was also suggested by the increase of the torque during mixing and by the increase of the viscosity and storage modulus of the blends.

The dynamic vulcanization process was only effective for compatibilized blends. For this blend, the vulcanized rubber particles presented lower particle size, which was effectively surrounded by the PP matrix, characterizing an actual thermoplastic vulcanizate. However, superior mechanical performance and finer morphology with smaller rubber particle size were achieved for non vulcanized/compatibilized blends. Probably due to the decrease of the interfacial tension, the improvement of the interfacial adhesion and the crosslinking of the rubber particles, imparted by TETA in combination with PP-g-MA.

The reactive compatibilization also resulted in a decrease of damping and an increase of storage modulus obtained from dynamic mechanical analysis and an increase of melting and crystallization

Table 4. Tensile properties of compatibilized PP/ACM blends as a function of the reprocessing

Cycles	Non vulcanized blend (NV2)		Vulcanized blend (V2)	
	Ultimate tensile strength [MPa]	Elongation at break [%]	Ultimate tensile strength [MPa]	Elongation at break [%]
1	15.3 ± 0.4	280 ± 30	16.5 ± 0.2	190 ± 4
2	17.7 ± 0.3	230 ± 20	17.7 ± 0.3	200 ± 10
3	16.4 ± 0.1	235 ± 35	17.1 ± 0.2	190 ± 8
4	16.3 ± 0.2	310 ± 25	16.6 ± 0.4	220 ± 15

temperature as a result of the mobilization restriction imparted by the chemical bonds at the interface. The PP/ACM thermoplastic elastomers presented good reprocessing ability.

Acknowledgements

We would like to acknowledge the Conselho Nacional de Desenvolvimento Científico e Tecnológico (CNPq), Coordenação de Aperfeiçoamento de Pessoal de Nivel Superior (CAPES), Financiadora de Estudos e Projetos (FINEP), Fundação de Amparo à Pesquisa do Estado do Rio de Janeiro (FAPERJ) and Petroflex Ind. Com. S.A. (now Lanxess) for the financial support for this project.

References

[1] Nakajima N., DeMarco R. D.: Application of polyacrylate rubber for high performance automotive gaskets and seals. Journal of Elastomers and Plastics, **33**, 114–120 (2001).

[2] Vial T. M.: Recent developments in acrylic elastomers. Rubber Chemistry and Technology, **44**, 344–362 (1971).

[3] Giannetti E., Mazzocchi R., Fiore L., Crespi E.: Ammonium salt catalyzed crosslinking mechanism of acrylic rubbers. Rubber Chemistry and Technology, **56**, 21–30 (1983).

[4] Jha A., Dutta B., Bhowmick A. K.: Effect of fillers and plasticizers on the performance of novel heat and oil-resistant thermoplastic elastomers from nylon-6 and acrylate rubber blends. Journal of Applied Polymer Science, **74**, 1490–1501 (1999).

[5] Jha A., Bhowmick A. K.: Thermal degradation and ageing behavior of novel thermoplastic elastomeric nylon-6/acrylate rubber reactive blends. Polymer Degradation and Stability, **62**, 575–586 (1998).

[6] Ding X., Xu R., Yu D., Chen H., Fan R.: Effect of ultrafine, fully vulcanized acrylate powdered rubber on the mechanical properties and crystallization behavior of nylon 6. Journal of Applied Polymer Science, **90**, 3503–3511 (2003).

[7] Jha A., Bhowmick A. K.: Influence of dynamic vulcanization and phase interaction on the swelling behavior of the thermoplastic elastomeric blends of nylon-6 and acrylate rubber in various solvents and oil. Journal of Applied Polymer Science, **69**, 2331–2340 (1998).

[8] Wong-On J., Wootthikanokkhan J.: Dynamic vulcanization of acrylic rubber-blended PVC. Journal of Applied Polymer Science, **88**, 2657–2663 (2003).

[9] Wimolmala E., Wootthikanokkhan J., Sombatsompop N.: Effects of composition and temperature on extrudate characteristics, morphology, and tensile properties of acrylic rubber-blended PVC. Journal of Applied Polymer Science, **80**, 2523–2534 (2001).

[10] Li Y., Yuko O., Kadowaki Y., Inoue T., Nakayama K., Shimizu H.: A novel thermoplastic elastomer by reaction-induced phase decomposition from a miscible polymer blend. Macromolecules, **39**, 4195–4201 (2006).

[11] Shivakumar E., Srivastava R. B., Pandey K. N., Das C. K.: Compatibility study of blends of acrylic rubber (ACM), poly(ethyleneterephtalate) (PET), and liquid crystalline polymer (LCP). Journal of Macromolecular Science, Part A: Pure and Applied Chemistry, **42**, 1181–1195 (2005).

[12] Wu C., Otani Y., Namiki N., Emi H., Nitta K-H.: Phase modification of acrylate rubber/chlorinated polypropylene blends by a hindered phenol compound. Polymer Journal, **33**, 322–329 (2001).

[13] Margolis J. M.: Elastomeric materials and processes. in 'Handbook of Plastics, Elastomers and Composites' (ed.: Harper C. A.) McGraw-Hill, New York, 189–228 (2004).

[14] Gupta N. K., Jain A. K., Singhal R., Nagpal A. K.: Effect of dynamic crosslinking on tensile yield behavior of polypropylene/ethylene-propylene-diene rubber blends. Journal of Applied Polymer Science, **78**, 2104–2121 (2000).

[15] Chatterjee K., Naskar K.: Development of thermoplastic elastomers based on maleated ethylene propylene rubber (m-EPM) and polypropylene (PP) by dynamic vulcanization. Express Polymer Letters, **1**, 527–534 (2007).

[16] Manchado M. A. L., Arroyo M., Kenny J. M: New developments in dynamically cured PP-EPDM blends. Rubber Chemistry and Technology, **74**, 211–220 (2002).

[17] Zhang X., Huang H., Zhang Y.: Dynamically vulcanized nitrile rubber/polypropylene thermoplastic elastomers. Journal of Applied Polymer Science, **85**, 2862–2866 (2002).

[18] Naderi G., Nouri M. R., Mehrabzadeh M., Bakhshandeh G. R.: Studies on dynamic vulcanization of PP/NBR thermoplastic elastomer blends. Iranian Polymer Journal, **8**, 37–42 (1999).

[19] George S., Varughese K. T., Thomas S.: Dielectric properties of isotactic polypropylene/nitrile rubber blends: Effects of blend ratio, filler addition, and dynamic vulcanization. Journal of Applied Polymer Science, **73**, 255–270 (1999).

[20] Coran A. Y., Patel R.: Rubber-thermoplastic compositions. VIII. Nitrile rubber-polyolefin blends with technological compatibilization. Rubber Chemistry and Technology, **56**, 1045–1060 (1983).

[21] Soares B. G., Almeida M. S. M., Deepa Urs M. V., Kumaraswamy G. N., Ranganathaiah C., Siddaramaiah, Mauler R.: Influence of curing agent and compatibilizer on the physicomechanical properties of polypropylene/nitrile butadiene rubber blends investigated by positron annihilation lifetime technique. Journal of Applied Polymer Science, **102**, 4672–4681 (2006).

[22] Nakason C., Wannavilai P., Kaesaman A.: Thermoplastic vulcanizates based on epoxidized natural rubber/polypropylene blends: Effect of epoxide levels in ENR molecules. Journal of Applied Polymer Science, **101**, 3046–3052 (2006).

[23] Thitihammawong A., Nakason C., Sahakaro K., Noordermeer J.: Effect of different types of peroxides on rheological, mechanical and morphological properties of thermoplastic vulcanizates based on natural rubber/polypropylene blends. Polymer Testing, **26**, 537–546 (2007).

[24] Asaletha R., Bindu P., Aravind I., Meera A. P., Valsaraj S. V., Yang W., Thomas S.: Stress-relaxation behavior of natural rubber/polystyrene and natural rubber/polystyrene/natural rubber-graft-polystyrene blends. Journal of Applied Polymer Science, **108**, 904–913 (2008).